

X-Ray and Neutron Diffraction Studies of Strongly Correlated Electron Systems

X-RAY AND NEUTRON DIFFRACTION STUDIES OF STRONGLY
CORRELATED ELECTRON SYSTEMS

By

JOHN-PAUL ADRIAN CASTELLAN, M.Sc.

A Thesis

Submitted to the School of Graduate Studies

in Partial Fulfillment of the Requirements

for the Degree

Phd.

McMaster University

© Copyright John-Paul A. Castellan, 2007

Doctor of Philosophy (2007)
(Physics)

McMaster University
Hamilton, Ontario

TITLE: X-Ray and Neutron Diffraction Studies of Strongly Correlated Electron
Systems

AUTHOR: John-Paul A. Castellan, M.Sc. (McMaster University)

SUPERVISOR: Dr. B.D. Gaulin

NUMBER OF PAGES: xvi, 106

Acknowledgements

I would like to thank my supervisor, Dr. Bruce D. Gaulin for his guidance during the course of this work. As well I would like to thank the members of my supervisory committee, Dr. G. Luke and Dr. J.E. Greedan.

I would like to take the opportunity to thank Marek Kiela for his technical mastery, without his help none of this would have been possible. Marek was exceptional at ensuring the lab equipment was in working order. I would like to thank our crystal grower, without Hanna Dabkowska there would have been nothing to study. She was responsible for making the wonderful Bi-2212 samples that were used in this study.

I would like to thank my family and friends for there support and encouragement. Finally, I would like to thank Allison Hanak for her patience and support.

Preface

This thesis is comprised of three original works presented in Chapters 4,5, and 6. The three projects are comprised of three different problems in condensed matter physics, the commonality between the topics is the technique used to study the materials, diffraction. Two of which are in the form of journal articles that have been peer-reviewed and published in Physical Review B, while the third is that of an unpublished work. The unpublished work is presented first and uses neutron scattering techniques, while two published papers were performed using x-ray diffraction.

The neutron scattering experiments were performed by myself with the assistance of William J.L. Buyers and B.D. Gaulin. These experiments were performed at Chalk River Laboratories in northern Ontario. The x-ray scattering experiments were carried out on the rotating anode x-ray laboratory at McMaster University and the Advanced Photon Source in Argonne Il. All data analysis was performed by myself under the guidance of B.D. Gaulin.

Contents

1	Scattering	1
1.1	Introduction	1
1.2	Diffraction	1
1.3	Neutron Scattering	2
1.3.1	Cross Section	3
1.3.2	Nuclear Scattering	4
1.3.3	Magnetic Scattering	5
1.3.4	Triple-Axis Spectrometer	5
1.4	X-Ray Scattering	7
2	Critical Phenomena	11
2.1	General Introduction	11
2.1.1	Critical Phase Transitions	12
2.2	Ginzberg-Landau Theory	14
2.2.1	Critical Exponents	16
2.2.2	Universality and Scaling	17
2.3	Magnetic Critical Scattering	21
3	Magnetic Systems	23
3.1	Dilute Magnetic Systems	23

3.1.1	Percolation	24
3.1.2	Random Fields	25
3.2	Frustrated Magnetic Systems	30
4	Random Field Domains and the Partially-paramagnetic State of	
	CsCo_{0.83}Mg_{0.17}Br₃	33
4.1	Introduction	35
4.2	Experimental Details	38
4.3	Experimental Results	39
4.4	Discussion	52
4.4.1	CASE 1: Partially Paramagnetic Phase	54
4.4.2	CASE 2: Low Temperature Ordered Phase	56
4.5	Conclusion	57
	Bibliography	58
5	Two and Three Dimensional Incommensurate Modulation in Optimally-	
	Doped Bi₂Sr₂CaCu₂O_{8+δ}	61
5.1	Introduction	64
5.2	Materials and Experimental Methods	66
5.3	Experimental Results	67
5.3.1	Three Dimensional Modulated Structure	67
5.3.2	Two Dimensional Modulated Structure	72
5.4	Discussion and Relation to STM Imaging	77
5.5	Conclusions	83
5.6	Acknowledgements	84
	Bibliography	84

6	Structural Ordering and Symmetry Breaking in $\text{Cd}_2\text{Re}_2\text{O}_7$	88
6.1	Introduction	91
6.2	Experimental Details	93
6.3	Order Parameter	93
6.4	Lattice Parameters	97
6.5	Discussion	101
6.6	Summary	104
	Bibliography	104

List of Figures

1.1	Diffraction from layers of periodic atoms	2
1.2	Schematic diagram of a triple-axis spectrometer.	6
1.3	Spectrum from an x-ray generator	8
2.1	Illustration of a simple gas-liquid-solid phase diagram.	12
2.2	Illustration of a simple magnetic phase transition of a ferromagnetic. T_c denotes the critical point in the phase diagram, below which the system enters the ferromagnetic phase	13
2.3	Free energy plotted as a function of the order parameter, M	16
3.1	Illustration of the phase diagram for a dilute magnetic system plotted against the magnetic ion concentration.	24
3.2	Illustration of the random field domain state of the classic Random Field Ising Model.	27
3.3	The effect of an impurity on an antiferromagnet in an applied field. The red arrows depict spin-up(+z direction), while the blue depicts spin-down moments. The applied field is aligned in the +z direction. The state (a) is lower in energy than state (b) by $2B$	27

3.4	Quasielastic scattering observed along the longitudinal direction $\vec{Q} = (1 + \xi, 0, 0)$ at 5.3K with H=60kG. The best fits to the Lorentzian (a long-dashed line), to the Lorentzian-squared (a short-dashed line), to Eq. 3.5 (a solid line) are shown. R indicates the instrumental resolution. Taken from Birgeneau [1].	29
3.5	Resolution-corrected inverse correlation length κ in $Rb_2Co_{0.7}Mg_{0.3}F_4$ at various fields as a function of temperature. The solid lines are guides to the eye. The units are $\frac{2\pi}{a_m} = 1.083\text{\AA}^{-1}$. Taken from Birgeneau [1]. .	29
3.6	Magnetic structure for nearest neighbour interactions for a square lattice A, and a triangular lattice B.	31
4.1	The unit cell of CsCoBr ₃ . It is a simple hexagonal structure, with space group $P6_3/mmc$ and lattice constants $a=7.47\text{\AA}$ and $c=6.27\text{\AA}$.	35
4.2	(a) An Illustration of the three sublattice ordered state of CsCoBr ₃ ($\sim 20K < T < 28K$). (b) An Illustration of the low temperature ($< 13K$) ordered state of CsCoBr ₃ . + depicts up spins, - down spins, and P paramagnetic sites.	36
4.3	Peak magnetic Bragg intensity at the magnetic zone centers $(\frac{2}{3}, \frac{2}{3}, 1)$ in CsCoBr ₃ and $(\frac{4}{3}, \frac{4}{3}, 1)$ in CsCo _{0.83} Mg _{0.17} Br ₃ . [2]	37
4.4	Peak neutron intensity plotted on a logarithmic scale at the magnetic zone center, $(\frac{2}{3}, \frac{2}{3}, 1)$ in CsCo _{0.83} Mg _{0.17} Br ₃ as a function of temperature in both zero applied magnetic field (blue) and a magnetic field of B=2.6 T applied along the c -axis. The red curve shows the field cooled measurements, while the black curve shows the zero field cooled measurements.	40

4.5	Critical neutron scattering scans along the (H,H,1) direction in reciprocal space. The scattering from the magnetic zone center, $(\frac{2}{3}, \frac{2}{3}, 1)$ is shown in a colour contour map for $\text{CsCo}_{0.83}\text{Mg}_{0.17}\text{Br}_3$ as a function of temperature for zero applied field (top) and for B=2.6T field (bottom). The magnetic field is applied along the c -axis for the data shown in the lower part of the plot.	41
4.6	Representative scan in the (H,H,1) direction at T=20K in zero applied field. Fits to the two components (Lorentzian squared and Lorentzian) of the scattering. Peaking at each of the two magnetic zone centers $(\frac{1}{3}, \frac{1}{3}, 1)$ and $(\frac{2}{3}, \frac{2}{3}, 1)$ are displayed clearly.	43
4.7	Representative critical neutron scattering scans along (H,H,1) from which the colour contour map of Fig. 4.5 was constructed. These are shown for both zero applied magnetic field (left hand panels) and for B=2.6T (right hand panels). Also, shown as the solid blue lines are fits to the critical scattering as described in the text.	45
4.8	Fit parameters κ_{ab} (top panel) and κ_c (bottom panel) as a function of temperature extracted from fits to the data using Eq. 4.2. Black circles are appropriate to zero applied magnetic field, while red boxes are appropriate to B=2.6T applied along the c -axis.	46
4.9	Inverse correlation lengths extracted from the fit parameters for the Lorentzian term in Eq. 4.2. Black circles are appropriate to zero applied magnetic field, while red boxes are appropriate to B=2.6T applied along the c -axis.	48

4.10	Amplitudes of the two components of the scattering observed in $\text{CsCo}_{0.83}\text{Mg}_{0.17}\text{Br}_3$ extracted from fits of the data to Eq. 4.2. Top panel (log scale) is the amplitude from the Lorentzian-squared term, A_2 . Bottom panel (linear scale) is the amplitude of the Lorentzian term A_1 . Zero field is represented by the black circles and in field data with $B=2.6\text{T}$ applied along the c -axis is represented by red boxes.	49
4.11	The temperature dependence of the a -lattice parameter as measured from the $(\frac{2}{3}, \frac{2}{3}, 1)$ magnetic Bragg peak position.	51
4.12	Amplitude of the Lorentzian-squared term, A_2 from fits of the data to Eq. 4.2 are plotted on a linear scale. (a) shows the full temperature range demonstrating the upturn near T_{n3} in pure CsCoBr_3 . (b) shows an expanded scale near the phase transition, T_{n1}	52
4.13	A comparison of two $[H,H,1]$ critical scattering scans near $[\frac{2}{3}, \frac{2}{3}, 1]$, both well below T_{n1} . Each has been normalized such that the peak intensity is 1.	53
4.14	Role of nonmagnetic atoms in generating a random field domain state in the Partially Paramagnetic state of CsCoBr_3 . a) Zero magnetic field, the nonmagnetic Mg ion couples to the paramagnetic site. b) Applied magnetic field along the c -axis, the nonmagnetic Mg ion couples to the lattice sites which would have aligned opposite to the applied magnetic field in the absence of the vacancy.	55

4.15	Role of nonmagnetic atoms in generating a random field domain state in the low temperature ordered phase of CsCoBr ₃ . a) Zero magnetic field, the system will not be in the RF state and the system should fully order. b) Applied Magnetic Field along the c -axis, the nonmagnetic Mg ion couples to the lattice sites which would have aligned opposite to the applied magnetic field in the absence of the vacancy.	57
5.1	A schematic diagram depicting one unit cell of Bi ₂ Sr ₂ CaCu ₂ O _{8+δ} is shown. The light (orange) pyramids represent CuO ₂ plus apical oxygen complexes, while the dark (blue) octahedra represent BiO ₂ plus apical oxygen atom complexes. The Cu ions reside at the center of the base of the light pyramids, while the Bi ions reside at the center of the octahedra. The CuO ₂ and BiO ₂ bilayer thicknesses are 3.3 Å and 3.2 Å, respectively, while the bilayer-bilayer separation, <i>c</i> /2, is ~ 15.4 Å.	65
5.2	Synchrotron X-ray scattering scans on a logarithmic intensity scale along [0,K,0] (top panel) and [0,K,1] (lower panel) in Bi ₂ Sr ₂ CaCu ₂ O _{8+δ} . A total of four harmonics of the modulated structure with the form (0, 4-n×τ, L) are observed at both L=0 and L=1, and they clearly alternate between resolution-limited and broad along both K and L (see Fig. 5.3). The broad component to the scattering is well described by a Lorentzian-squared lineshape (see Fig. 5.4).	68

5.3	Rotating anode x-ray scattering measurements on a logarithmic intensity scale show the L-dependence of the principal Bragg peaks, such as [0,4,L] (top panel); the first order harmonic of the modulated structure [0, 3.79, L] (middle panel); and the second order harmonic of the primary modulated structure [0, 3.58, L] (bottom panel). The harmonics alternate with L between resolution-limited Bragg scattering and broad scattering which is well described by a Lorentzian-squared lineshape (see Fig. 5.4).	70
5.4	X-ray scattering scans along K (top) and L (bottom) taken from Figs. 5.2 and 5.3 and plotted on a linear intensity scale. Both plots show the second order harmonics of the primary modulation [0, 3.58, 1] and [0, 3.58, 5]. These positions correspond to wavevectors with broad (as opposed to resolution-limited) lineshapes. Also shown is the fit to each lineshape using a Lorentzian-squared form, Eq. 5.1, which is clearly excellent. As described in the text, this lineshape is typically used to describe the three dimensional random field domain state in disordered magnets.	71
5.5	X-ray scattering scans of the form [H, 3.58, 5] which show the new modulated structure corresponding to a doubling of the unit cell along a is shown. The dashed line in the upper panel shows where the scans reside in reciprocal space, passing through the second order harmonic of the primary modulation. The middle and lower panels show these scans on logarithmic (middle) and linear (bottom) intensity scales, with Lorentzian lineshapes (Eq. 5.2) fit to the data. The bottom panel also demonstrates the lack of temperature dependence to this scattering below room temperature.	73

- 5.6 X-ray scattering scans of the form $[1/2, K, 5]$ which display the new modulated structure corresponding to a doubling of the unit cell along \mathbf{a} is shown. The upper panel shows where the scans reside in reciprocal space, passing through the first four harmonics of this new modulated structure. The data in the bottom panel is fit to Lorentzian lineshapes (Eq. 5.2) centered at each of the four harmonic positions along \mathbf{K} . Also shown for comparison in the same panel are \mathbf{K} scans of the first and second harmonics of the primary modulated structure, whose linewidth defines the instrumental resolution. 75
- 5.7 X-ray scattering scans of the form $[1/2, K, L]$ which observe the new modulated structure corresponding to a doubling of the unit cell along \mathbf{a} are shown. The top panel shows L-scans of the second order ($K=3.58$) harmonic of this scattering, at different temperatures below 250 K, as well as a background scan of the form $[\cdot 3, 3.45, L]$. The lower panel shows the L dependence of each of the first four harmonics of this structure at 10 K. Remarkably over the 10 Brillouin zones from $L=10$ to $L=-10$, a near complete rod of scattering is observed for the first order harmonic ($K=3.79$), while higher order harmonics peak up weakly at $L=\pm 5$ 76

5.8	The correlation areas of the new modulated structure corresponding to a doubling of the unit cell along \mathbf{a} extracted from our x-ray scattering analysis are superposed on STM topographs[9] of the surface of $\text{Bi}_2\text{Sr}_2\text{CaCu}_2\text{O}_{8+\delta}$. Our measurements indicate isotropic short range correlations with a correlation length of $\sim 27 \text{ \AA}$, and these correspond very well to the extent of the “S” microstructure which appears to be imprinted on the primary modulated structure of $\text{Bi}_2\text{Sr}_2\text{CaCu}_2\text{O}_{8+\delta}$, as observed in real space with the STM measurements.	81
6.1	The top panel shows the integrated intensity of the (0,0,10) superlattice Bragg peak as a function of temperature, compared with the square of the order parameter expected from mean field theory, and that expected from the 3 dimensional Ising model. The lower shows the same data in the immediate vicinity of $T_{C'} \sim 194 \text{ K}$, along with a fit to critical behavior modeled as a power law in reduced temperature (left-hand y-axis), and the broad critical scattering as measured at (0.04,0.064,10) (right-hand y-axis).	95
6.2	High resolution scans of the scattering at and near the (0,0,10) superlattice Bragg peak positions are shown for the temperatures marked by arrows in the inset to Fig. 6.1. Data is shown in maps as a function of sample rotation angle Ω and scattering angle 2θ . The two diffraction features at 2θ values of $\sim 97.7^\circ$ and 98.07° are from $\text{Cu K}_{\alpha 1}$ and $\text{Cu K}_{\alpha 2}$ radiation, respectively. The top of the linear color scale is different for each data set.	96

6.3	The right hand panels shows longitudinal cuts taken through the (0,0,12) principal Bragg peak position well above $T_{C'}$ (bottom) and well below (top). This data, on a linear scale, shows a clear shoulder on the high 2θ side of both the Cu $K_{\alpha 1}$ and $K_{\alpha 2}$ peaks. The left hand panels show the superlattice (0,0,10) (top) and principal (0,0,12) (bottom) Bragg peaks on a semi-log scale, at temperatures just below and well below $T_{C'}$. Clearly, while the principal Bragg peaks split on lowering the temperature, the superlattice peaks do not.	98
6.4	The temperature dependence of the lattice parameters extracted from fits to the (0,0,12) principal Bragg peaks are shown, along the temperature dependence of the superlattice (0,0,10) Bragg peak periodicity below $T_{C'}$. The error bars indicate uncertainties associated with the absolute values of the lattice parameters.	100
6.5	The temperature dependence of the lattice parameters extracted from fits to the (0,0,12) principal Bragg peaks are shown, along the temperature dependence of the superlattice (0,0,10) Bragg peak periodicity below $T_{C'}$	102

Chapter 1

Scattering

1.1 Introduction

Neutron and X-ray scattering are some of the principle techniques for studying the microscopic characteristics of materials. The wavelengths of both probes are comparable to the inter-atomic distance between atoms in a solid. In the case of neutron scattering the energy scale is appropriate to measure excitations within the materials.

1.2 Diffraction

Diffraction by crystals was first discovered by van Laue in 1912 and further developed by Bragg in 1913. The diffraction process can be illustrated by imagining several planes of atoms separated by an inter-atomic spacing, d , as seen in figure 1.1. If the beam of particles incident on the planes has a de Broglie wavelength on the order of d , these waves can be reflected from the planes in the solid.

The path difference of the two waves shown in figure 1.1 will be $2d \sin \theta$. For constructive interference to occur, the path difference must be equal to the wavelength of the incident particles, or an integer number of wavelengths. These spots of intensity

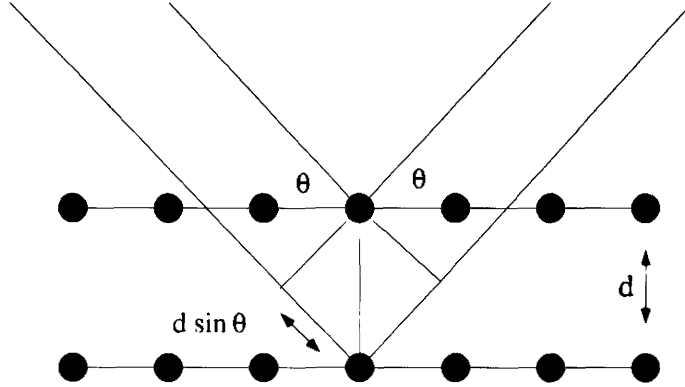


Figure 1.1: Diffraction from layers of periodic atoms

are seen experimentally and are referred to as Bragg peaks. This diffraction condition is known as Bragg's law and is written as,

$$n\lambda = 2d \sin \theta \quad (1.1)$$

1.3 Neutron Scattering

Neutrons can be produced by nuclear fission and by spallation. Neutrons produced from fission are moderated within the reactor to form a Maxwellian distribution of speeds which correspond to the temperature of the moderating material. Moderating materials are typically light or heavy water at temperatures near room temperature (300K). By heating or cooling the moderators the peak of the flux distribution of neutrons can be shifted to higher and lower energies. Thermal neutrons have energies on the order of $k_B T$ where the T is the temperature of the moderator. Room temperature moderators, $T=300\text{K}$, typically have wavelengths on the order of $1 - 2\text{\AA}$ and energies in the 10-25meV range.

Thermal neutrons interact with matter in two ways. The first of these is with the nucleus of an atom via the strong force. This interaction only extends over a very

short length scale on the order a few femtometers. This interaction will either cause the neutron to be scattered by the nucleus or absorbed by the nucleus. The neutron also has a magnetic dipole moment and thus can interact with matter via magnetic forces. The dipole moment of a neutron is $\mu_n = -\gamma\mu_N\sigma$, where $\gamma = 1.913$, μ_N is the nuclear magneton and σ is the Pauli spin operator for a particle with spin $\frac{1}{2}$ [3]. In condensed matter systems there are many magnetic solids with unpaired electrons associated with the magnetic ion. These unpaired electrons and associated magnetic moments will also scatter neutrons. This interaction is on a much longer length scale than that of the nuclear interactions.

The neutron scattering formalism is covered in many text books devoted to the topic most notably, Squires [4] and Lovesey[5]. The discussion to follow is a summary that is pertinent to the present work.

1.3.1 Cross Section

The only events that can occur to a neutron are that the neutron is scattered or it is absorbed. We can write the total cross section as:

$$\sigma_t = \sigma_a + \sigma_s \tag{1.2}$$

where σ_s is the scattering cross section, the total number of neutrons scattered by the target per second, and σ_a is the number of neutrons absorbed by the target per second. The cross section has dimensions of area and is usually quoted in barns, where 1 barn= $10^{-28}m^2$. In our case the scattering probability is small and we can thus use the first Born approximation.

Neutron scattering experiments measure a quantity known as the partial differential cross section. This is the probability of a neutron scattering into a solid angle $d\Omega$ in an energy range of dE' . The initial state for the neutron is $|\mathbf{k}\sigma\rangle$ and the final state is $|\mathbf{k}'\sigma'\rangle$, where the \mathbf{k} 's are the initial and final neutron wavevector and the

σ 's are the initial and final spin states for the neutron. The target is initially in state $|\lambda\rangle$ and then found in a final state $|\lambda'\rangle$. Then the partial differential cross section is given by [6]:

$$\frac{d^2\sigma_s}{d\Omega dE'} = \frac{k'}{k} \left(\frac{m}{2\pi\hbar^2} \right)^2 |\langle \mathbf{k}'\sigma'\lambda' | V | \mathbf{k}\sigma\lambda \rangle|^2 \delta(E_\lambda - E_{\lambda'} + E - E') \quad (1.3)$$

where E_λ is the energy of the target in state $|\lambda\rangle$, m is the mass of the neutron, and V is the interaction potential between the neutron and the target. This interaction potential V can come about from the interaction with the nucleus or by the dipole interaction of the neutron with magnetism in the target.

1.3.2 Nuclear Scattering

For a system of N identical nuclei with a scattering length b , the partial differential cross section for coherent scattering is:

$$\frac{d^2\sigma_s}{d\Omega dE'} = \frac{k'}{k} N b^2 S(\mathbf{Q}, \omega) \quad (1.4)$$

where $\hbar k$ and $\hbar k'$ are the initial and final neutron momenta, \mathbf{Q} is the scattering wavevector ($\vec{Q} = \vec{k} - \vec{k}'$), and ω is the energy transfer ($\hbar\omega = E - E'$). The scattering function, $S(\mathbf{Q}, \omega)$ is the space and time Fourier transform of the nuclear correlation function.

$$S(\mathbf{Q}, \omega) = \frac{1}{\hbar N} \sum_{j1} \int_{-\infty}^{\infty} e^{i\omega\tau} d\tau \langle e^{-i\mathbf{Q}\cdot R_{j1}(0)} e^{i\mathbf{Q}\cdot R_j(\tau)} \rangle \quad (1.5)$$

where $R_j(\tau)$ is the position of the j^{th} atom at time τ .

The scattering length, b , of an atom depends on the nature of the nucleus. Different isotopes of the same chemical species will have different scattering lengths. As well as the isotope effect there will be a dependence on the particular spin orientation of the neutron and the spin of the nucleus. The end result of this is that the

scattering cross section will be broken up into two terms; a coherent term, σ_c and an incoherent term, σ_i . Where:

$$\sigma_s = \sigma_c + \sigma_i \quad (1.6)$$

$$\sigma_c = 4\pi(\bar{b})^2 \quad (1.7)$$

$$\sigma_i = 4\pi(\bar{b}^2 - (\bar{b})^2) \quad (1.8)$$

1.3.3 Magnetic Scattering

The magnetic partial differential cross section for N identical magnetic atoms on a lattice has a similar form to Eq. 1.4[4][5]:

$$\frac{d^2\sigma_s}{d\Omega dE'} = (\gamma r_o)^2 \frac{k'}{k} \frac{N}{h} |F(\mathbf{Q})|^2 \sum_{\alpha\beta} (\delta_{\alpha\beta} - \hat{\mathbf{Q}}_\alpha \hat{\mathbf{Q}}_\beta) \mathbf{S}^{\alpha\beta}(\mathbf{Q}, \omega) \quad (1.9)$$

The magnetic form factor is labeled as $F(\mathbf{Q})$ and arises from the fact that the magnetic moment has a finite spatial extent. The form of this function is dependent upon which magnetic atom is scattering the neutron because of the spatial distribution of the unpaired electron. There is also a polarization factor, $(\delta_{\alpha\beta} - \hat{\mathbf{Q}}_\alpha \hat{\mathbf{Q}}_\beta)$. This term has the effect that only components of the moment perpendicular to the scattering wavevector contribution to the scattering. Again $\mathbf{S}(\mathbf{Q}, \omega)$ is a space and time correlation function; this time it is the spin-spin correlation function. The scattering length here is γr_o and is a magnetic analog to the nuclear scattering length, b .

$$S^{\alpha,\beta}(\mathbf{Q}, \omega) = \frac{1}{2\pi} \sum_r e^{i\mathbf{Q}\cdot\mathbf{R}} \int_{-\infty}^{\infty} e^{i\omega\tau} \langle S_{0\alpha}(0) S_{R\beta}(\tau) \rangle d\tau \quad (1.10)$$

1.3.4 Triple-Axis Spectrometer

All of the relevant information we would like to obtain in a neutron scattering experiment is contained in the scattering function, $\mathbf{S}(\mathbf{Q}, \omega)$. The triple axis spectrometer

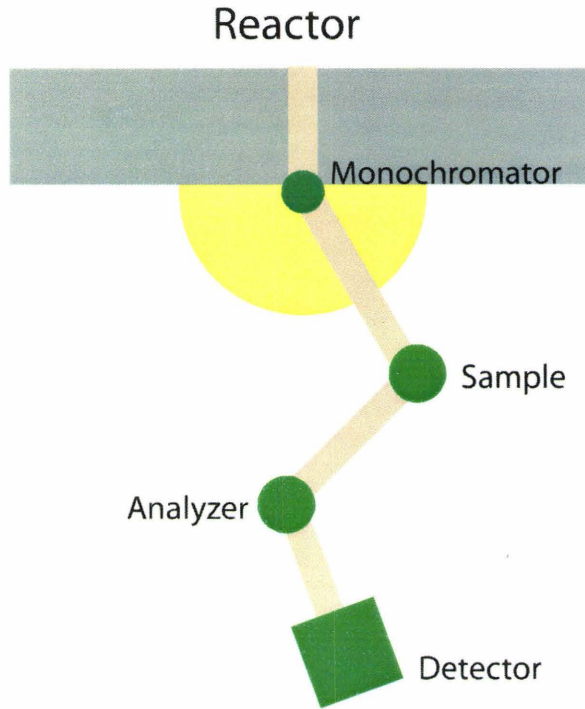


Figure 1.2: Schematic diagram of a triple-axis spectrometer.

developed by Brockhouse, was designed to measure $S(\mathbf{Q}, \omega)$ on a grid in \vec{Q}, ω space. The components of a triple-axis spectrometer are depicted in Figure 1.2. With the triple-axis spectrometer there are three scattering events; one to produce a monochromatic beam from the “white” beam of neutrons coming from the reactor core, the second at the sample, and the third to analyze the energy distribution of the scattered neutrons from the sample.

Using Bragg’s law, we can determine the scattering angle needed to select a beam of neutrons with a single wavelength, thus producing a monochromatic beam. At the sample position there are several rotational stages. The purpose of these rotation stages is to align the sample such that it is in the correct orientation to scatter neutrons off of planes in the crystal (or equally to orient the sample in reciprocal space). This same process is used to analyze the final energy of the scattered neutrons.

Using this technique, the incident wavevector, \vec{k} ; final wavevector, \vec{k}' ; and the energy transfer, $\hbar\omega$ can be selected. This gives us the unique ability to measure systematically $S(\mathbf{Q}, \omega)$ over large regions of \vec{Q} and ω space.

The beam collimation has a small angular divergence. The mosaic spread of the monochromator and analyzer crystals also introduce a spread in the incident and final wavevectors. Therefore the resolution of the instrument is not perfect. This is often good as finite resolution will be required in order to have measurable count rates. Because of this, the measurement is actually a convolution of the scattering function with the instrument's resolution function.

$$I(\mathbf{Q}, \omega) \sim \int (S(\mathbf{Q} - \mathbf{Q}', \omega - \omega') R(\mathbf{Q}', \omega') d\omega' d^3\mathbf{Q}') \quad (1.11)$$

where $R(\mathbf{Q}, \omega)$ is the resolution function for the instrument.

1.4 X-Ray Scattering

The way in which x-rays have been produced in small laboratories has changed relatively little since Roentgen's discovery of x-rays in 1895. The basic components of an x-ray generator are a source of high energy electrons from a tungsten filament and a large potential difference with which to accelerate the electrons and a target; typically copper or molybdenum.

Electromagnetic theory tells us that an accelerated charged particle will emit radiation [7]. Electrons incident on a metal will undergo a rapid deceleration and thus will produce radiation. Furthermore, each electron will be decelerated in a different manner some losing all their energy at once and others after many collisions with the atoms in the metal. The result of this process produces a continuous spectrum of radiation with an upper cutoff corresponding to the full energy of the incident

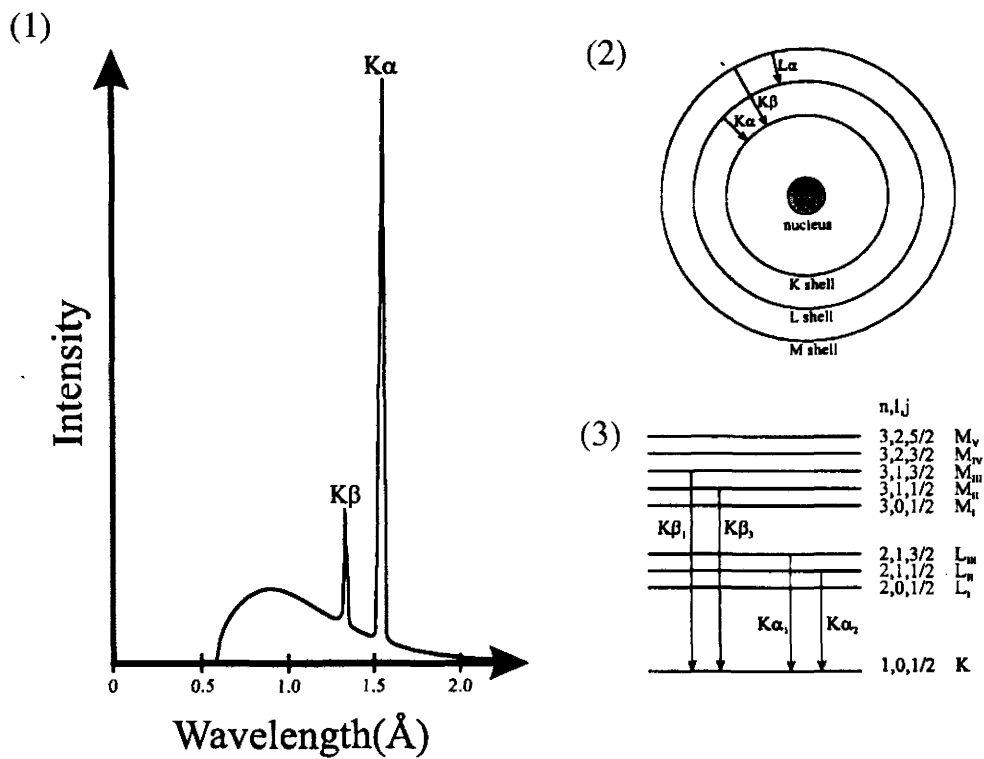


Figure 1.3: (1) Spectrum of radiation from an x-ray generator with a copper target. (2) Atomic shell model describing $K\beta$ and $K\alpha$ lines. (3) Diagram showing the quantum numbers and $K\beta$ and $K\alpha$ sub lines.

electron as seen in Figure 1.3. This continuum of radiation is known as Bremsstrahlung or braking radiation.

In addition to this Bremsstrahlung radiation, some electrons may cause one of the inner shell electrons to be ejected. When one of the higher energy electrons falls into this vacant state, left by the ejected electron in the shell, a photon is emitted. The energy of the photons produced from this secondary effect will be discrete in nature and the wavelength of the radiation will be dependent upon which shell the electron decays from and the characteristic atoms in the metal target. The two sharp features in figure 1.3 are due to transitions from the L shell to the K shell and the M shell to the K shell respectively. These peaks can be further split into a doublet commonly denoted as $K_{\alpha 1}$ and $K_{\alpha 2}$. This differentiates between the two electrons that share the K shell with opposite spin thus giving an energy difference between the two. The spectra shown in Figure 1.3 are for a copper target and the wavelengths for the peaks are as follows:

$$K_{\alpha 1} : 1.54051 \text{ \AA}$$

$$K_{\alpha 2} : 1.54433 \text{ \AA}$$

$$K_{\beta 1} : 1.39217 \text{ \AA}$$

Since X-rays scatter from the electron cloud, the scattering power of an atom will scale with Z , the atomic number. As a result light atoms such as Hydrogen are weak scatterers and heavy atoms such as Lead are strong scatterers. Another difference between neutron and x-ray scattering is the size of the scattering centers; for neutrons they are point scatterers, while x-rays the scattering dimensions are of the size of the atom. The x-ray atomic form factor is of the following form [8]:

$$f = \frac{4\pi}{e} \int_0^{\infty} r^2 \rho(r) \frac{\sin(kr)}{kr} dr \quad (1.12)$$

where in this case $k = (4\pi \sin(\theta))/\lambda$.

One of the most important things that one can measure with x-ray scattering is the positions of all the atoms in the unit cell of a material. This information is contained within the X-ray scattering structure factor, $F(\vec{Q})$;

$$F(\vec{Q}) = \sum_n f_n e^{2\pi i \vec{Q} \cdot \vec{r}_n} \quad (1.13)$$

where \vec{Q} is a reciprocal lattice vector and r_n is the position of the n^{th} atom in the unit cell.

Chapter 2

Critical Phenomena

2.1 General Introduction

Critical phenomena occur in the region of a phase diagram near the boundary where a system changes from one state to another. A typical example of a phase diagram is that of simple gas-liquid-solid system shown in Figure 2.1. Figure 2.1 shows a plot of pressure as a function of temperature. The three phases, gas, liquid, and solid are separated by lines called phase boundaries. The point where all the phase boundaries intersect is known as the triple point. At this point in the phase diagram all three phases can coexist.

When crossing a phase boundary if we observe a discontinuous change in properties accompanied with latent heat, then the transition is called a first order phase transition. However, if there is a continuous change in state across the boundary this type of transition is known as a second order or continuous phase transition. These two types of phase transitions can also be described by the Gibbs free energy, $G(P,T)$. If the first derivative of G , dG/dp or dG/dT is discontinuous this indicates a first order phase transition. Likewise if the first derivative is continuous then we refer to this type of transition as second order. For the subject of this thesis we will

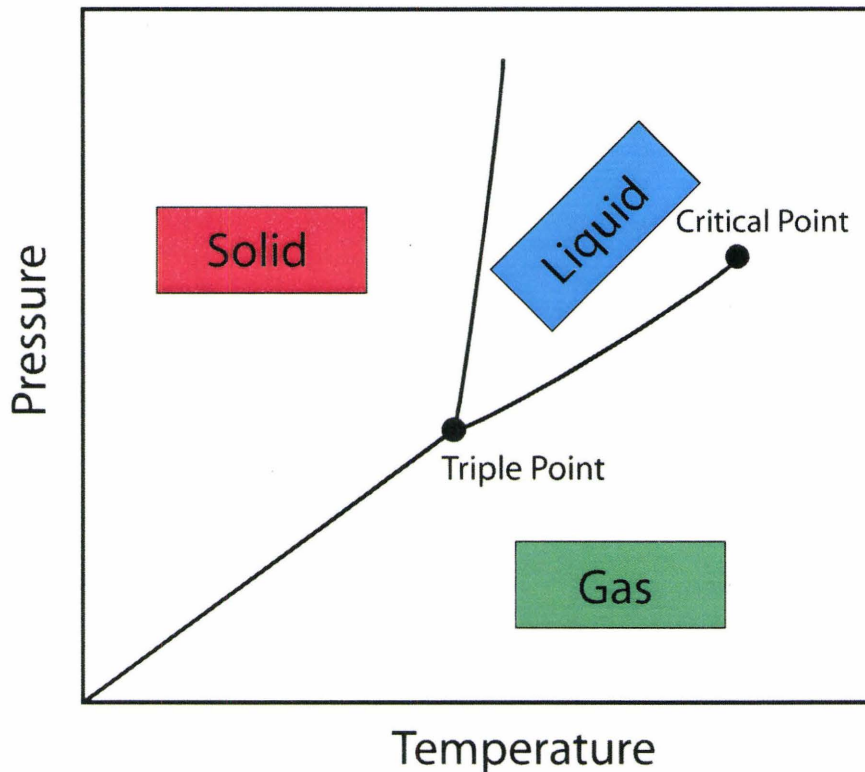


Figure 2.1: Illustration of a simple gas-liquid-solid phase diagram.

focus on second order phase transitions.

2.1.1 Critical Phase Transitions

Phase transitions near a critical point in the phase diagram have short lived fluctuating micro regions of one phase in the other. These fluctuations give rise to scattering known as critical scattering. As we approach the critical region in the phase diagram these fluctuations grow in size and become infinite at the critical point[9].

For the rest of the discussion we will switch from the gas-liquid-solid example to that of a simple magnetic phase transition. The magnetic example is that of a simple continuous phase transition from a paramagnetic structure to that of an ordered ferromagnet. We will need to define a variable to describe the ordered fer-

romagnetic state. In the paramagnetic state the magnetization, \mathbf{M} , is zero in zero applied magnetic field, whereas at low temperature, below the ferromagnetic ordering temperature, the magnetization, \mathbf{M} is finite. Therefore, a measure of \mathbf{M} is a measure of the magnetic order of the system. Such quantities as \mathbf{M} are known as order parameters.

Figure 2.2 is an diagram depicting a typical measurement of the magnetization as a function of temperature for ferromagnetic systems. We see that \mathbf{M} is a continuous function but the derivatives of \mathbf{M} diverge at T_c . The transition here in zero field has no latent heat and is described as a critical phase transition. If we look at the applied

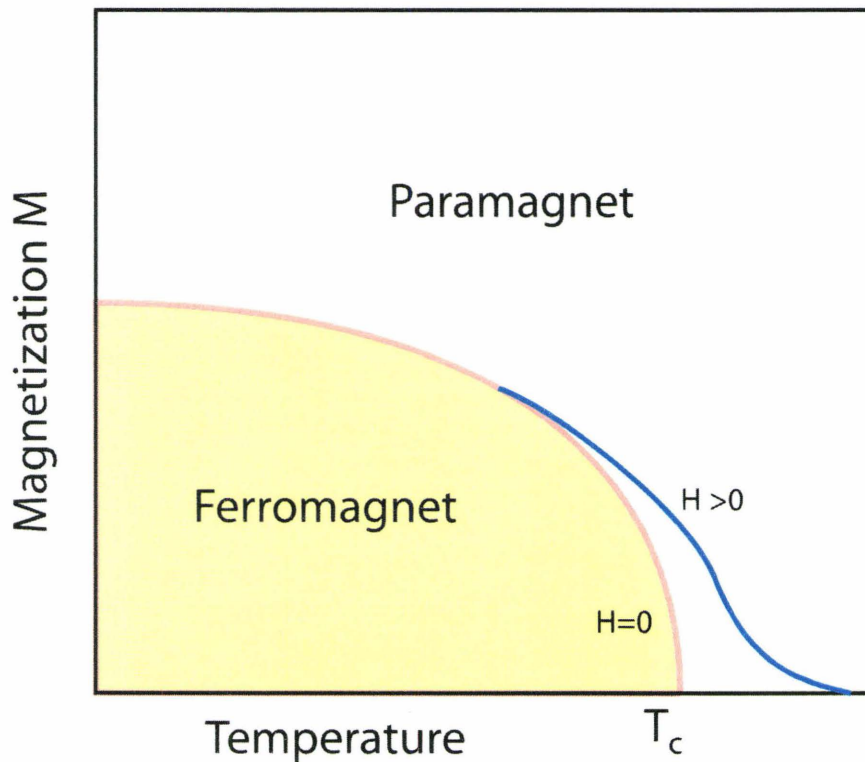


Figure 2.2: Illustration of a simple magnetic phase transition of a ferromagnetic. T_c denotes the critical point in the phase diagram, below which the system enters the ferromagnetic phase

magnetic field case (blue curve) we can pass from the paramagnetic phase to the ferromagnetic phase without passing through the critical point.

There are several properties that are common amongst all critical phase transitions [6]. There is a broken symmetry at the phase transition. The order parameter is a continuous function of temperature; \mathbf{M} is zero above T_c and nonzero below T_c . \mathbf{M} may be a scalar or a vector with some dimensionality, D . The dimensionality describes the number of degrees of freedom the order parameter displays. Near the critical point there are fluctuations of both phases present. The extent of these fluctuating regions is described by the correlation length, ξ . ξ will tend to infinity as we approach the critical point from any direction. The response time, critical slowing down for the system, will tend to infinity as we approach the critical point.

2.2 Ginzberg-Landau Theory

Mean field or Landau theory is one of the simplest treatments of phase transitions. First we must identify the order parameter for the system in question; for magnetism this is usually the magnetization or a sublattice magnetization for an antiferromagnet. Then using this order parameter we write a Taylor series expansion of the free energy in powers of M . This theory is only valid for regions in the phase diagram near the critical point.

The free energy function is a function of T and M and near the critical point the Free energy would behave as[6]:

$$F(T, M) = A(T) + B(T)M^2 + C(T)M^4 + \dots \quad (2.1)$$

In this example the odd terms are missing and the value of the free energy is the same for M as $-M$; thus odd terms do not appear. Also, M^2 is really $M^2 = M \cdot M$. At any given temperature the system is in equilibrium, as characterized by a minimum

in $F(T,M)$. We have to satisfy the following relations:

$$\left. \frac{dF}{dM} \right|_T = 0$$

and

$$\left. \frac{d^2F}{dM^2} \right|_T > 0$$

Then

$$M \cdot B(T) + 2M^3 \cdot C(T) = 0$$

and

$$B(T) + 6M^2 \cdot C(T) > 0$$

If we are above the critical temperature then $M=0$, then we know that $B(T) > 0$ for $T > T_c$. Below T_c M is nonzero then we get:

$$B(T) = -2M^2 \cdot C(T) \quad \text{for } (T < T_c)$$

$$M^2 \cdot C(T) > 0 \quad \text{for } (T < T_c)$$

Then $C(T) > 0$ and $B(T) < 0$ for $T < T_c$. We can see that there is a change in sign of $B(T)$ at the critical temperature. If we now expand $B(T)$ about $T = T_c$ and only look at the lowest order nonzero terms we end up with:

$$B(T) = (T - T_c)A(T) \tag{2.2}$$

With $A(T)$ positive we find that M^2 is:

$$M^2 = \frac{A(T)}{2C(T)}(T_c - T) \tag{2.3}$$

for $T < T_c$. Now we can solve for the Free energy for the two cases of $T > T_c$ and $T < T_c$.

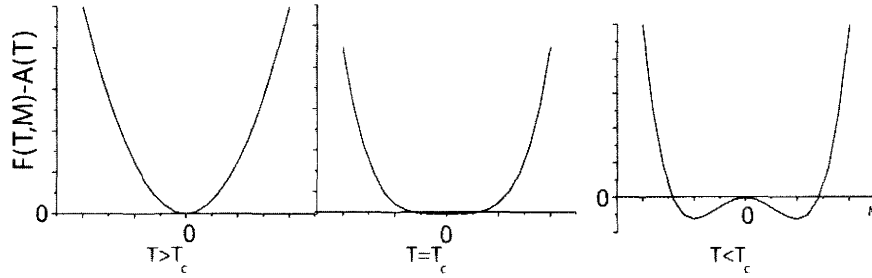


Figure 2.3: Free energy plotted as a function of the order parameter, M

$$F(T, M) = A(T) \quad \text{for} \quad (T > T_c)$$

$$F(T, M) = A(T) - \frac{B(T)^2}{4C(T)}(T - T_c)^2 \quad \text{for} \quad (T < T_c)$$

We can illustrate these results graphically, Figure 2.3. When we are above the critical temperature the free energy has a minimum at $M=0$. Then as we cool below the critical temperature we find that the minimum has moved out to the values of $M = \pm[A(T)(T - T_c)/2C(T)]^{1/2}$. Here we see that the order parameter is proportional to $\sim (T - T_c)^{1/2}$. Several physical quantities near a phase transition follow related power law relations. These exponents are known as critical exponents and vary as $[(T - T_c)/T_c]^x$ near phase transitions.[9].

2.2.1 Critical Exponents

In magnetic systems there are many physical quantities that can be measured near the phase transition, such as the susceptibility, specific heat, correlation length, and magnetization. The first three diverge at the critical point, while the fourth tends to zero. Experimentally we cannot measure right at the divergence. Many experiments have been performed and show how the properties diverge near the critical point, and

Property	Critical Exponent	Power Law	Conditions	Theoretical Predictions	Experiment
Susceptibility, χ_T	γ	$t^{-\gamma}$	$T > T_c, H=0$	1	1.3-1.4
Susceptibility, χ_T	γ'	$(-t)^{-\gamma'}$	$T < T_c, H=0$	1	-
Magnetization, M	β	$(-t)^\beta$	$T > T_c, H=0$	0.5	0.2-0.4
Magnetization, M	δ	$H^{\frac{1}{\delta}}$	$T = T_c$	3	3-6
Specific Heat, C_H	α	$t^{-\alpha}$	$T > T_c, H=0$	Discontinuous	-0.3-0.3
Specific Heat, C_H	α'	$(-t)^{-\alpha'}$	$T < T_c, H=0$	Discontinuous	-0.3-0.3
Correlation Length, ζ	ν	$t^{-\nu}$	$T > T_c, H=0$	0.5	0.6-0.7
Correlation Length, ζ	ν'	$(-t)^{-\nu'}$	$T < T_c, H=0$	0.5	0.6-0.7

Table 2.1: Some Magnetic Critical Exponents, with a comparison between predictions from Mean Field Theory and values found experimentally. Taken from Collins [6].

that many physical properties seem to obey some form of power law. For example the susceptibility near the critical temperature was found to follow the following power law:

$$\chi_T = at^{-\gamma} \quad T > T_c \quad (2.4)$$

where $t = (T - T_c)/T_c$ and a and γ are constants. The power law holds from system to system but γ can itself vary depending the characteristics of the system. Table 2.1 is taken from Collins [6] and lists some of the critical exponents with a comparison of theory to experiments performed.

2.2.2 Universality and Scaling

For a continuous phase transition the critical exponents depend on the dimensionality of the system, d , the dimensionality of the order parameter D , and the range of the interactions involved. This generalizes things greatly as it does not matter what the microscopic details of the system are, as long as the range of the interactions is small.

As well, the critical exponents will not depend on the what the specific crystal lattice is for the material being studied. This is the general idea behind universality.

This concept allows us to simplify the theory by choosing the simplest theoretical model for a particular universality class (particular choice of d and D). If the solution for the critical exponents for the simplest model with a class can be found then all other systems within the same class will have the same critical exponents.

The different values for the dimensionality of the order parameter, or the symmetry of the order parameter, D are:

1. $D=1$, The Ising Model: In the magnetic case the spin would be restricted in one-dimension, say the \mathbf{z} -direction. Hamiltonians for Ising systems resemble the following[6]:

$$H = - \sum_n \sum_i' J_i S_n^z S_{n+i}^z \quad (2.5)$$

The exchange constant J couples the spins, on sight n with site $n+1$. The sum over i adds this interaction up over the nearest-neighbour sites.

2. $D=2$, The X-Y model: Again in the magnetic case the spins here have 2 degrees of freedom, now within the \mathbf{xy} -plane and an example Hamiltonian for this system would be[6]:

$$H = - \sum_n \sum_i' J_i (S_n^x S_{n+i}^x + S_n^y S_{n+i}^y) \quad (2.6)$$

3. $D=3$: The Heisenberg model: Now the spin is a full three-dimensional vector and we need all three components of the spin in the Hamiltonian[6]:

$$H = - \sum_n \sum_i' J_i (S_n^x S_{n+i}^x + S_n^y S_{n+i}^y + S_n^z S_{n+i}^z) \quad (2.7)$$

4. $D=\infty$, The spherical model: In this model the spin would have an infinite number of dimensions. There are no experimental realizations of this model but this model has the attraction that it can be exactly solved.

Model	Mean Field	Ising	Ising	X-Y	X-Y	Heisenberg	Spherical
D	any	1	1	2	2	3	∞
d	any	2	3	2	3	3	3
γ	1.0	1.75	1.2378(6)	–	1.316(9)	1.388(3)	1
ν	0.5	1	0.6312(3)	–	0.669(7)	0.707	1
x	–	1.875	2.481(1)	–	2.484(9)	2.482(5)	2.5
α	–	0	0.106	–	-0.01	-0.121	-1
β	0.5	0.125	0.326	–	0.345	0.367	0.5
δ	3	15	4.78	15	4.81	4.78	5
η	0	0.25	0.039	0.25	0.03	0.37	0

Table 2.2: Values of the Critical Exponents for the different universality classes. Taken from Collins [6].

Even though we have simplified the problem by introducing universality there remain systems which are too difficult to be solved. To tackle these more difficult problems the idea of scaling is introduced. In the region near the critical point in the phase diagram there will be large volumes that are on the size of that of the correlation length, ξ . In these regions the magnetization will be fairly constant. There will be many of these regions in the sample with approximately the same magnetization but with perhaps a different direction. These large regions will fluctuate fairly slowly with time and since the correlation length diverges as we approach the critical point these volumes will be very large[6][9].

Scaling theory is derived with the assumptions that the Gibbs free energy and correlation length do not depend on the length scale, L . This is true provided that L is less than the correlation length, ξ . Then the Gibbs free energy and correlation

length can be written in terms of the reduced temperature, t , and the reduced effective magnetic field, h .

$$h = \frac{g\mu_B H_e}{k_B T} \quad , \quad t = \frac{T - T_c}{T_c} \quad (2.8)$$

If we change our cell size from L to lL we obtain the following relations for the Gibbs free energy and correlation length[6]:

$$l^{-1}\xi(t, h) = \xi(l^y t, l^x h) \quad (2.9)$$

$$l^d G(t, h) = G(l^y t, l^x h) \quad (2.10)$$

again d is the dimensionality of the system and x and y are indices related to the critical exponents. These equations will be valid for any arbitrarily large value of l . This will include the case where $l^y t = 1$. Near the critical temperature the reduced temperature, t , is very small and just above T_c will be positive. Using these two conditions and having zero field, $h=0$, the equations above become:

$$\xi(t) = t^{-1/y}\xi(1) \quad (2.11)$$

$$G(t) = t^{d/y}G(1) \quad (2.12)$$

From Table 2.1 we saw that $\xi(t) \sim t^{-\nu}$, we find that $y = \nu^{-1}$. Using the Gibbs free energy we can calculate the specific heat, c_H .

$$c_H = -T \left. \frac{\partial^2 G}{\partial T^2} \right|_H \quad (2.13)$$

$$c_H = -T \frac{d}{y} \left(\frac{d}{y} - 1 \right) t^{d/y-2} G(1) T_c^{-2} \quad (2.14)$$

before we saw that $c_H \sim t^{-\alpha}$ and near T_c , T can be treated as a constant. We then obtain [6]:

$$\frac{d}{y} - 2 = -\alpha, \quad 2 - \alpha = \frac{d}{y} = d\nu \quad (2.15)$$

Equations like the one above that relate one critical exponent to another are known as scaling laws. Another key scaling law is:

$$\gamma + \alpha + 2\beta = 2 \quad (2.16)$$

2.3 Magnetic Critical Scattering

Neutron scattering has proven to be very useful in studying magnetic phase transitions. One can measure many of the important quantities such as the order parameter and fluctuations in the order parameter, or correlation length using this technique. Going back to the magnetic cross section determined earlier in Eq. 1.9 we can use this to get an idea of what the neutrons can measure[6].

The first case we consider is where we integrate over all energies to obtain the static correlation function, $C(Q)$. If we integrate Eq. 1.9 over energy we get[6].

$$\frac{d\sigma}{d\Omega} = \frac{N}{h} (\gamma r_o)^2 |F(Q)|^2 \sum_{\alpha\beta} (\delta_{\alpha\beta} - \hat{k}_\alpha \hat{k}_\beta) C^{\alpha\beta}(Q, t) \quad (2.17)$$

where t is the reduced temperature ($t = (T - T_c)/T_c$), and $C(Q)$ is[6]:

$$C^{\alpha\beta}(Q) = \sum_R e^{iQ \cdot R} \langle S_{0\alpha} S_{R\beta} \rangle \quad (2.18)$$

This is the real space static correlation function, which for $T > T_c$ can be approximated as[10][11]:

$$C(R, t) \sim |R^{(1-d)/2}| \xi^{(3-d)/2 - \eta} e^{-(|R|/\xi)} \quad (2.19)$$

In three dimensions η is very small ~ 0.03 . Taking $\eta = 0$ then the Fourier transform of Eq. 2.19 has the following Lorentzian form[11]:

$$C(Q, t) \sim \frac{1}{q^2 + \kappa^2} \quad (2.20)$$

where κ is the inverse correlation length, ξ^{-1} , and \vec{q} is the displacement from the ordering wavevector ($\vec{q} = \vec{Q} - \vec{Q}_o$). By determining the temperature dependence of the width of a magnetic scattering at the Bragg position one can measure the inverse correlation length and obtain the critical exponent ν . Likewise, the amplitude of $C(Q)$ can be extracted obtain the critical exponent γ . $C(Q) \sim \chi(Q) \sim [(T - T_c)/T_c]^{-\gamma}$.

The second case of interest is $T < T_c$ we can look at the spin correlation function for infinite time. This will pick out features in $S(\vec{Q}, \omega)$ that are static, $\omega=0$.

The elastic part of the cross section is:

$$S_{elastic}^{\alpha\beta}(\vec{Q}, \omega) = \delta\omega \sum_R e^{i\vec{Q}\cdot\vec{R}} \langle S_{0\alpha}(0)S_{R\beta}(\infty) \rangle \quad (2.21)$$

This is proportional to the square of the order parameter. A measure of the elastic scattering as a function of temperature will give us 2β .

$$I \sim (\text{orderparameter})^2 \sim \left[\frac{T_c - T}{T_c} \right]^{2\beta} \sim t^{2\beta} \quad (2.22)$$

Chapter 3

Magnetic Systems

3.1 Dilute Magnetic Systems

So far we have been only considering systems that are homogeneous. The topic discussed in Chapter 4 is that of a dilute antiferromagnet, therefore at this time we will present a short discussion of the effects of dilution on magnetic systems. In any real material there is almost always impurities that lead to disorder. The effect of disorder on phase transitions is an intriguing and pervasive problem. Disorder can be generally classified into two groups; annealed disorder and quenched disorder.

Annealed disorder is one in which the disorder is in thermal equilibrium with the pure system and is free to move. Quenched disorder means that the impurities are frozen in place and unable to move, therefore the impurities are not in thermal equilibrium with the system. Examples of quenched disorder would include atoms adsorbed on the surface of the material and lattice defects within the sample.

To study the effect disorder has on phase transitions and magnetic properties of materials we are going to purposely add quenched disorder to a magnetic system. Transition metals like Mn, Co, Fe, and Mg are chemically very similar but magnetically very different, the quenched disorder is introduced by chemical substitution of

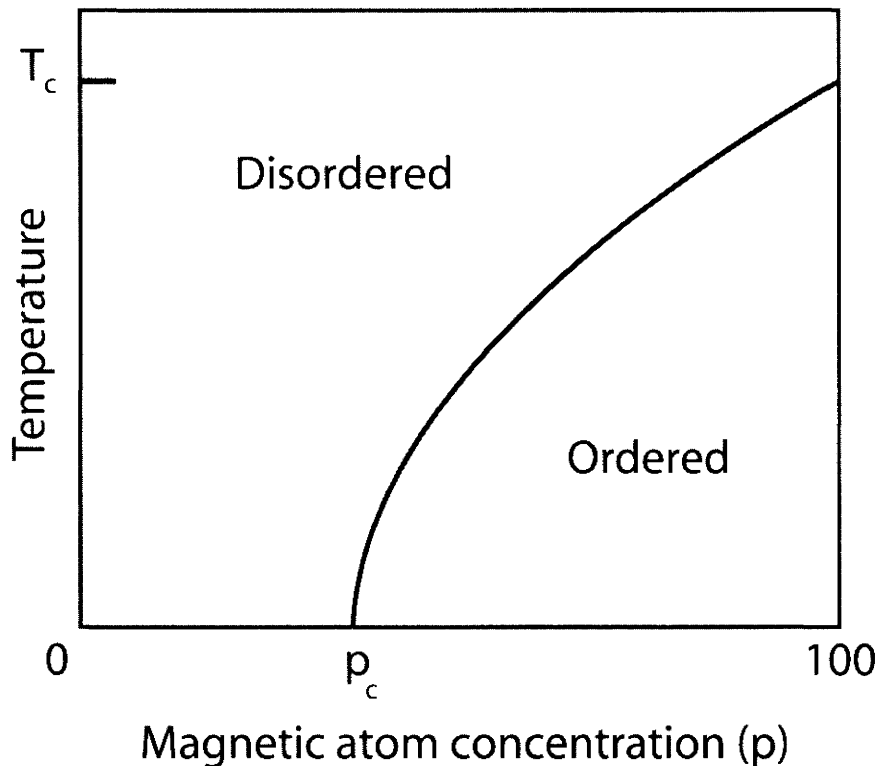


Figure 3.1: Illustration of the phase diagram for a dilute magnetic system plotted against the magnetic ion concentration.

a magnetic ion in the lattice for a non-magnetic one.

3.1.1 Percolation

If this dilution of the magnetism is sufficiently high one can eliminate the magnetic exchange path through the entire sample and destroy the long range ordered magnetic state. The dilution limit where long range order is destroyed is known as the percolation limit, p_c . Figure 3.1 shows a phase diagram for a simple diluted magnetic system. When the system is pure, 100%, we find that the critical temperature is T_c . As we remove magnetic ions we find that the phase transition temperature is reduced from T_c until we reach the critical concentration, p_c , where the system

never achieves long range order [6][12][9]. Typical values for the percolation limit for magnetic three-dimensional systems are as high as $\sim 70\%$ dilution.

In the region of the phase diagram shown in Fig. 3.1 far to the right of the percolation point, p_c there still remains a sharp critical phase transition. We can justify this by realizing that in regions close to the phase transition we will have large regions on the scale of ξ that will be ordered or disordered. If ξ is large enough it will average out the disorder present[9]. It is this region of the phase diagram that we are interested in.

3.1.2 Random Fields

One example system where quenched magnetic disorder in a material has a profound effect on the critical phase transition is that of the Random Field Ising Model (RFIM). This was first considered by Imry and Ma [13] and was argued that such random fields would destroy long range order in the system for dimensions less than 4 for continuous symmetry and destroy long range order in dimensions less than 2 for Ising like symmetry. If we consider an Ising ferromagnet and apply small random fields h_i along the z-axis at each site i with the condition that:

$$\langle h_i \rangle = 0, \quad \langle h_i^2 \rangle \neq 0 \quad (3.1)$$

The Hamiltonian for such a system is:

$$H = J \sum_{\langle ij \rangle} S_i S_j - \sum_i h_i S_i + B \sum_i S_i \quad (3.2)$$

where J is the nearest neighbor interaction and B is the applied external magnetic field.

With zero applied magnetic field ($B=0$) there is a symmetry breaking at critical temperature, T_n . One of two states must be chosen, with spins aligned along the $+z$ or $-z$ axis. The presence of these quenched random fields will affect how the

system chooses which of the two degenerate states locally. In some regions there will be an excess of fields, h_i along $+z$ and in other regions along $-z$. This is depicted in Fig. 3.2 which illustrates how the system will break up into domains of up and down domains.

In reality it is not possible to apply such random fields. Fishman and Aharony[14] showed that a dilute antiferromagnet with an applied magnetic field along the z -axis is a realization of the model presented in Eq. 3.2. With a dilute antiferromagnet some local regions on the lattice will have more spins on the spin-up sub-lattice than on spin-down sub-lattice. These local regions will form domains of one type while others will form the other way around. An illustration of the origin of these random fields is found in Figure 3.3. The sublattice of the antiferromagnet with the most spins aligned with the magnetic field is favored. This domain structure destroys long-ranged order in the system but there is still short-ranged order present within the domains. There is an overall energy gain from forming the random domains, however this is balanced by the fact that there is an energy cost at the domain wall. The domain wall will have broken bonds on surface, and an associated energy cost. This energy cost will be proportional to the surface area of the domain.

Studies of site-random Ising antiferromagnets have been carried out for both three-dimensional materials ($Co_xZn_{1-x}F_2$ [15], $Mn_xZn_{1-x}F_2$ [16], and $Mn_xZn_{1-x}F_2$ [17]) and for the quasi-two-dimensional systems ($Rb_2Co_{0.7}Mg_{0.3}F_4$ [1]). It is clear from these experiments that the field-cooled state at low temperatures is that of a system broken up into domains. We will briefly discuss general results from these experiments.

The example we will use to describe general features of a RFIM is that of the two-dimensional Ising Antiferromagnet $Rb_2Co_{0.7}Mg_{0.3}F_4$ in an applied magnetic field. $Rb_2Co_{0.7}Mg_{0.3}F_4$ is a 2D-square lattice nearest-neighbor Ising model with a

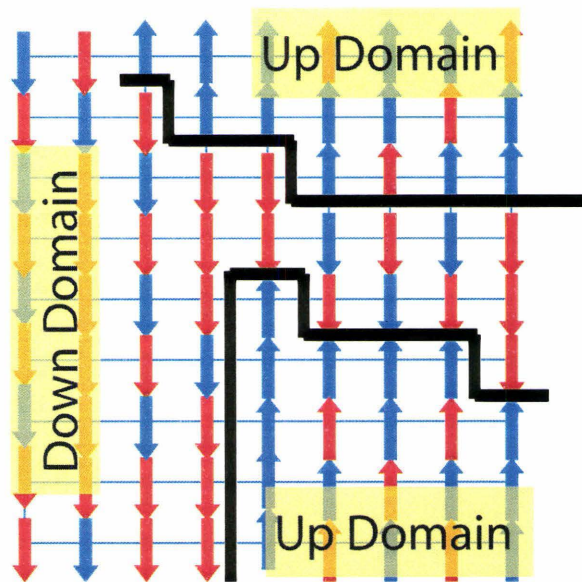


Figure 3.2: Illustration of the random field domain state of the classic Random Field Ising Model.

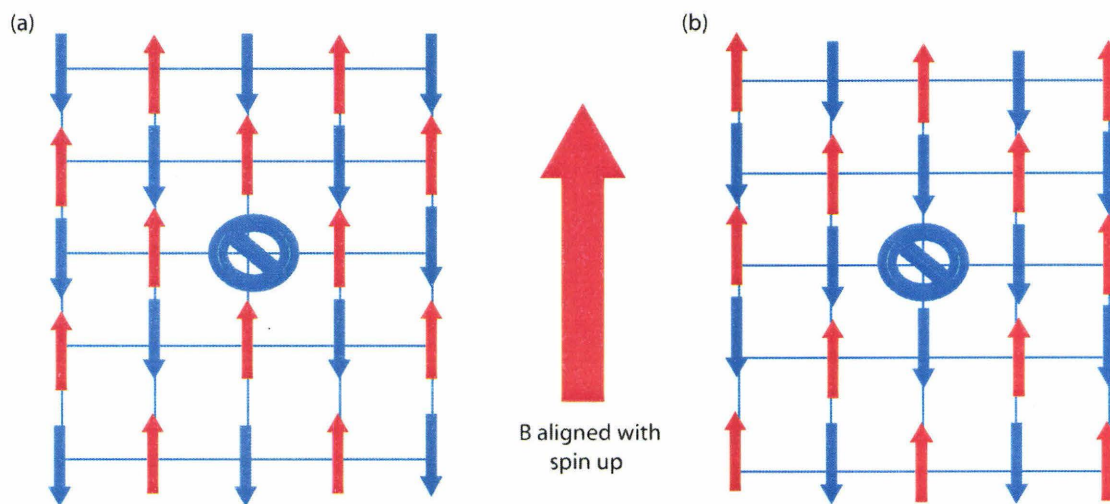


Figure 3.3: The effect of an impurity on an antiferromagnet in an applied field. The red arrows depict spin-up(+z direction), while the blue depicts spin-down moments. The applied field is aligned in the +z direction. The state (a) is lower in energy than state (b) by $2B$.

zero field Néel temperature, $T_n=42.5\text{K}$.

In an elastic neutron scattering experiment the scattering cross section will be proportional to the two spin correlation function. At high temperatures the system will exhibit Lorentzian fluctuations centered on the antiferromagnetic reciprocal lattice positions as discussed in Chapter 2 (see Eq. 2.20). Below T_n the cross section is the sum of the Lorentzian fluctuations along with the Bragg scattering and becomes:

$$S(\vec{Q}) = N \langle S^z \rangle^2 \delta(\vec{Q} - \vec{G}) + \frac{B'}{\kappa^2 + q^2}, T < T_n \quad (3.3)$$

The Bragg term (δ function term in Eq. 3.3) now will have to evolve into the domain structure of the random field state. For random-field effects the suggested spacial correlation function is[1]:

$$S(r) \sim \frac{e^{-\kappa r}}{r^{(d-3)/2}} \quad (3.4)$$

The Fourier transform of this is that of a Lorentzian-squared. Then $S(Q)$ from Eq. 3.3 becomes:

$$S(\vec{Q}) = \frac{A}{(\kappa^2 + q^2)^2} + \frac{B}{(\kappa^2 + q^2)} \quad (3.5)$$

This lineshape is indeed observed in Random Field Ising systems with typical data shown in Figure 3.4. Fig. 3.4 shows longitudinal scans along $\vec{Q} = [H, 0, 0]$ direction in reciprocal space centered at $H=1$. This two component line shape is a common feature in RFIM systems. From fitting a series of these transverse scans in reciprocal space as a function of temperature like that found in Fig. 3.4, we can extract the FWHM or inverse correlation length as a function of temperature.

Figure 3.5 displays the inverse correlation length extracted from fits to Eq. 3.5 from scans like that found in Fig. 3.4 for $Rb_2Co_{0.7}Mg_{0.3}F_4$. Fig. 3.5 shows that for low temperatures κ is independent of temperature for $T \leq 20\text{K}$ and is not resolution limited with the application of a magnetic field. This shows the destruction of long range order by the random field.

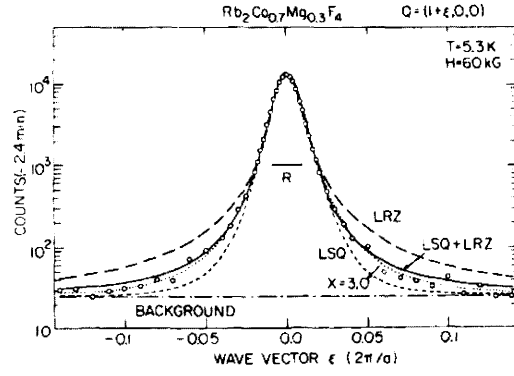


Figure 3.4: Quasielastic scattering observed along the longitudinal direction $\vec{Q} = (1 + \xi, 0, 0)$ at 5.3K with $H=60\text{kG}$. The best fits to the Lorentzian (a long-dashed line), to the Lorentzian-squared (a short-dashed line), to Eq. 3.5 (a solid line) are shown. R indicates the instrumental resolution. Taken from Birgeneau [1].

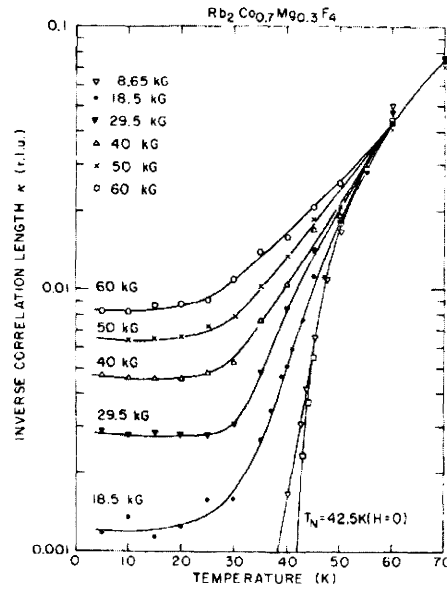


Figure 3.5: Resolution-corrected inverse correlation length κ in $Rb_2Co_{0.7}Mg_{0.3}F_4$ at various fields as a function of temperature. The solid lines are guides to the eye. The units are $\frac{2\pi}{a_m} = 1.083\text{\AA}^{-1}$. Taken from Birgeneau [1].

3.2 Frustrated Magnetic Systems

The topics discussed in Chapters 4 and 6 are related to systems that exhibit geometrically frustrated behaviour. In chapter 4 the magnetic system is in fact that of a frustrated magnetic system. While in chapter 6 the corner sharing tetrahedral structure of the pyrochlore is known to show frustration, however the material studied in Chapter 6 is not known to show exhibit magnetic properties. The following is a simple introduction to the idea of geometric frustration, for a complete review see Diep[18] and Greedan [19].

Geometrically frustrated magnetic materials have been of the subject of intense interest due to the rich diversity in exotic ground states that they display. Some of the exotic magnetic ground states known to exist are partially paramagnetic Néel states, complex noncollinear Néel states, disordered cooperative paramagnetic, spin liquids and spin glasses. To begin we will use a simple magnetic nearest neighbour model to illustrate the idea of frustration.

The interactions between spins, J , is responsible for the transition to long range magnetic order. If J is positive then ferromagnetic magnetism is favoured, conversely if J is negative antiferromagnetic order is favoured. If one looks at a two dimensional square lattice with nearest neighbour interactions then there are two types of ordered structures shown in Figure 3.6A. In structures like those in Fig 3.6A all the interactions between neighbouring spins can be satisfied. We can find many structures in which this is not always possible.

The simplest structure where not all the nearest neighbour interactions can be simultaneously satisfied is on a two-dimensional triangular lattice with antiferromagnetic interactions, as shown in Fig. 3.6B. Two of the three spins can be aligned antiparallel, but it is not possible to simultaneously align the third spin to the other two with an antiferromagnetic interaction. It is this effect that is known as lattice

frustration. There are bonds remaining for which the interaction energy is not minimized. This is not exclusive to two-dimensional triangular lattices, frustration can occur in many different lattice configurations. Frustration can also occur in systems where long range interactions are favoured instead of the nearest neighbour interactions or in systems with random interactions.

Many frustrated systems that do undergo phase transitions to a long range ordered state adopt a non-collinear spin configuration. An example of this is the two-dimensional triangular lattice with XY spins. The spins will adopt a 120° spin alignment which satisfies the antiferromagnetic interactions within a triangle. The vector sum of the spins on an individual triangle will be zero. This ground state is highly degenerate.

These non-collinear spin configurations do not work for Ising spins on a triangular lattice. Some Ising systems on a triangular lattice undergo phase transitions into what is known as a partially paramagnetic Néel state. These ground states are characterized as a multi-sub-lattice antiferromagnet. For the case of a triangular lattice two of the sites on a triangle would order, either up or down, while the third sublattice remains disordered.

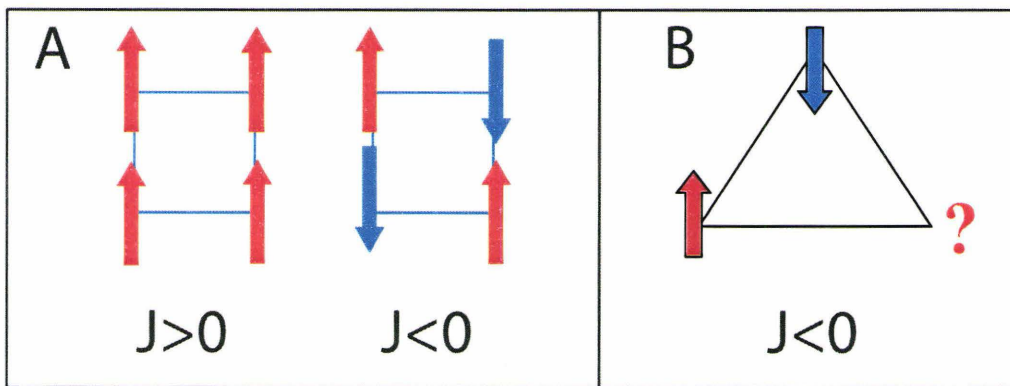


Figure 3.6: Magnetic structure for nearest neighbour interactions for a square lattice A, and a triangular lattice B.

There are also many frustrated systems where the ground states do not have any long range order. These include the cooperative paramagnets, spin glasses, spin liquids and spin ices. Many of the systems studied that exhibit this type of behaviour have a lattice structures made up of tetrahedra. The tetrahedra is to three dimensions what the triangle is to two dimensions and related degenerate ground states can occur.

Chapter 4

Random Field Domains and the Partially-paramagnetic State of $\text{CsCo}_{0.83}\text{Mg}_{0.17}\text{Br}_3$

Abstract

Critical neutron scattering measurements have been carried out on $\text{CsCo}_{0.83}\text{Mg}_{0.17}\text{Br}_3$, a dilute stacked triangular lattice (STL) Ising antiferromagnet. Measurements were carried out in both zero magnetic field and a magnetic field of 2.6 Tesla applied along the c -axis. Two components to the scattering, a Lorentzian-squared term and a Lorentzian term were found to be associated with the magnetic scattering. The Lorentzian-squared term appears at a temperature coinciding with T_{n1} of the pure material CsCoBr_3 . Such scattering is common in Random Field Ising Model systems. The random field domain state in this material is believed to arise as a consequence of the geometric frustration within the STL. The magnetic vacancies nucleate antiferromagnetic domains in which the vacancies reside on the disordered sub-lattice within the partially paramagnetic state of CsCoBr_3 . This creates a random field domain state without the application of a field. When a sufficiently strong magnetic field is applied, the random field will couple to the system in a different way. The magnetic field will minimize the number of sites on the down sublattice, those which oppose the magnetic field. With the application of a magnetic field, we see that it is the Lorentzian-squared term which is a signature of the random field domains, and not the broad Lorentzian component, as previously thought[2].

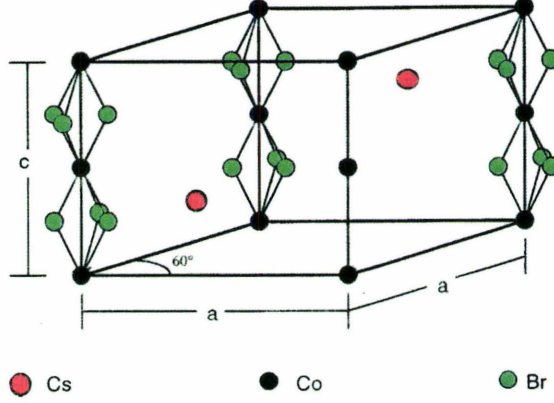


Figure 4.1: The unit cell of CsCoBr_3 . It is a simple hexagonal structure, with space group $P6_3/mmc$ and lattice constants $a=7.47\text{\AA}$ and $c=6.27\text{\AA}$

4.1 Introduction

CsCoBr_3 belongs to the ABX_3 family of stacked triangular lattice (STL) antiferromagnets. These materials make up an interesting group of magnetic systems in which quasi-one-dimensional exchange interactions along the \mathbf{c} -axis are very much stronger than those within the triangular \mathbf{ab} -plane. The interactions along \mathbf{c} are not frustrated, while the near neighbor antiferromagnetic interactions in the basal plane are frustrated. This geometrical frustration introduces novel ordering states of matter and novel critical phenomena at the relevant phase transitions. Inelastic neutron scattering studies [20] have determined the spin Hamiltonian for CsCoBr_3 to be:

$$H = \sum_{i(\vec{c})} \left(2J \left[S_i^z S_{i+1}^z + \epsilon (S_i^x S_{i+1}^x + S_i^y S_{i+1}^y) \right] + h_o S_i^z (-1)^i + 2J' \sum_{j(ab)}^6 S_i^z S_j^z \right) \quad (4.1)$$

where $J=1.62\text{Thz}$, $J'=0.0096\text{Thz}$ and $\epsilon=0.137$. For CsCoBr_3 the interactions along the \mathbf{c} -direction are ~ 170 times stronger than in the \mathbf{ab} plane. At temperatures $\sim 30\text{K}$ the weaker basal plane antiferromagnetic interactions become important. Two phase transitions are established with decreasing temperature, while a third has been suggested[21][22][23].

The highest temperature transition is that from a paramagnetic phase to a partially paramagnetic, three sublattice state. This unusual state is a consequence of frustration, and it is made up of triangular plaquettes where two of every three spins are ordered antiferromagnetically, with the third spin remaining paramagnetic. This sets in below an ordering temperature of $T_{n1}=28.3\text{K}$ and is characterized by magnetic ordering wavevectors of the form $(\frac{h}{3}, \frac{h}{3}, l)$ where l is odd. An intermediate transition at $T_{n2} \sim 16\text{K}$ is suggested to be where the remaining disordered site gradually orders. While the lowest temperature state sets in below $T_{n3}=13\text{K}$ [21] and this is where the paramagnetic site fully orders within the **ab**-plane, either up or down. This order creates ferrimagnetic sheets, which stack antiferromagnetically to create an antiferromagnetic structure with no net moment. The three-sublattice state and lowest temperature state are graphically illustrated in Fig. 4.2.

The Ising-like antiferromagnetic systems, CsCoBr_3 and CsCoCl_3 , have been

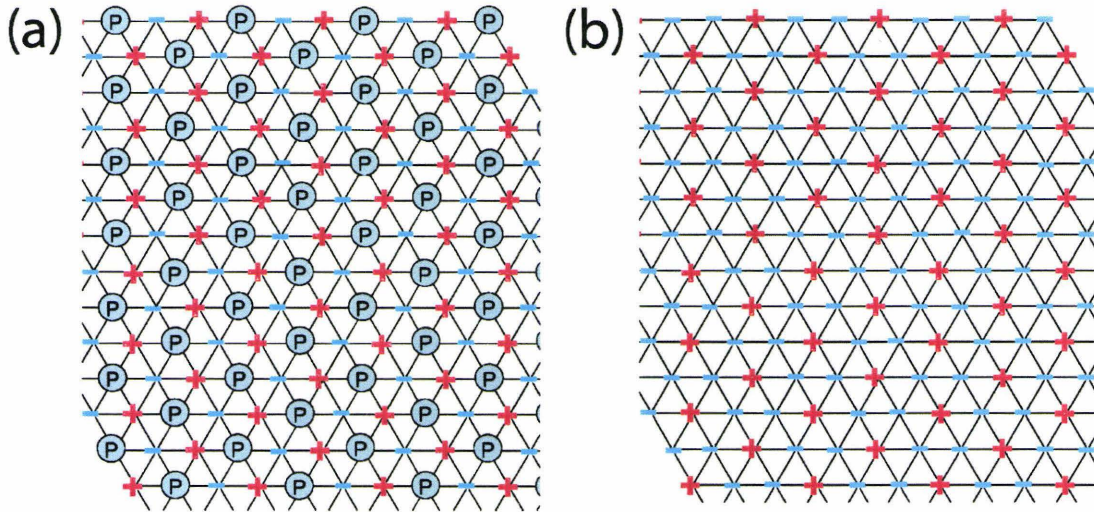


Figure 4.2: (a) An Illustration of the three sublattice ordered state of CsCoBr_3 ($\sim 20\text{K} < T < 28\text{K}$). (b) An Illustration of the low temperature ($< 13\text{K}$) ordered state of CsCoBr_3 . + depicts up spins, - down spins, and P paramagnetic sites.

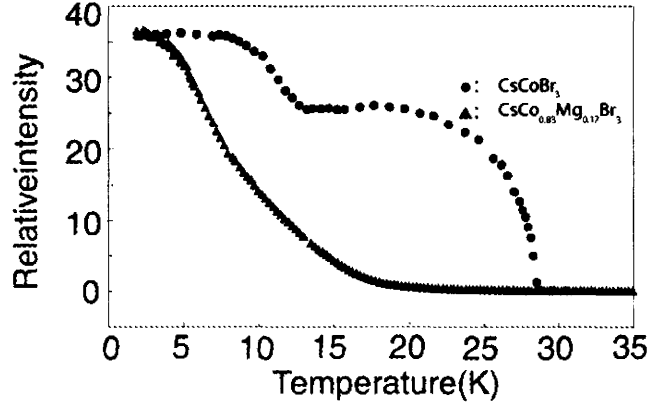


Figure 4.3: Peak magnetic Bragg intensity at the magnetic zone centers $(\frac{2}{3}, \frac{2}{3}, 1)$ in CsCoBr_3 and $(\frac{4}{3}, \frac{4}{3}, 1)$ in $\text{CsCo}_{0.83}\text{Mg}_{0.17}\text{Br}_3$. [2]

shown to be very sensitive to nonmagnetic impurities on the Co site. Several studies of doped $\text{CsCo}_{0.83}\text{Mg}_{0.17}\text{Br}_3$ [24] and $\text{CsCo}_{1-x}\text{Mg}_x\text{Cl}_3$ [25] where the Co is replaced with a nonmagnetic Mg show that 17% dilution of the cobalt site appears to completely disrupt the magnetic order in the materials. Figure 4.3 shows the temperature dependence of the elastic Bragg scattering at a magnetic ordering wavevector in both CsCoBr_3 and $\text{CsCo}_{0.83}\text{Mg}_{0.17}\text{Br}_3$. Here we see the magnetic neutron scattering peak intensity at $Q = (4/3, 4/3, 1)$ for $\text{CsCo}_{0.83}\text{Mg}_{0.17}\text{Br}_3$ shows only upward curvature down to $\sim 5\text{K}$. As well, the two clear transitions seen in CsCoBr_3 at $\sim 28\text{K}$ and $\sim 13\text{K}$ are not evident in $\text{CsCo}_{0.83}\text{Mg}_{0.17}\text{Br}_3$.

In the sister compound, $\text{CsCo}_{0.83}\text{Mg}_{0.17}\text{Cl}_3$ Nagler *et al.* [25] also observe upward curvature to the temperature dependence of the magnetic Bragg peak intensity at the magnetic zone center. No evidence of the transition at $T_n \sim 21\text{K}$ that is present in CsCoCl_3 is found either. Earlier low resolution critical neutron scattering studies performed by van Duijn *et al.* [2] on $\text{CsCo}_{0.83}\text{Mg}_{0.17}\text{Br}_3$ have shown that the critical scattering near the phase transitions in pure CsCoBr_3 are characterized by a two component line shape. The two components to the magnetic Bragg peak intensity

were analyzed as a sharp Lorentzian and broad Lorentzian. This two component lineshape has been interpreted in terms of a system entering a Random Field (RF) domain state below $T_{n1} \sim 28K$. Here the RF state is realized in the absence of an applied field as the non-magnetic vacancies (Mg ions) preferentially reside on the disordered sublattice. This earlier neutron scattering was taken with relatively low resolution and concentrated on the broad Lorentzian component of the scattering. The new neutron work reported here will concentrate on both components of the scattering and was enabled by significant improvements to the resolution of the measurements. This will provide information on both the broad and sharp components to the neutron scattering. The application of a 2.6 T magnetic field applied along the moment direction will be used to further study the RF state in the low temperature regime.

4.2 Experimental Details

Neutron scattering measurements were carried out on the C5 triple axis spectrometer, operated in a two axis mode, at the NRU reactor of Chalk River Laboratories. The sample was the same as the one studied previously by J. van Duijn *et al.*[2], Rogge *et al.* [24], and Yang *et al.* [26]. We employed 2.37\AA incident neutrons which were reflected off the (0,0,2) planes of a focusing pyrolytic graphite (PG) monochromator. Several PG filters were placed between the sample and the detector to remove higher order contamination from the diffracted beam. Measurements in zero applied magnetic field were carried out in a 4K. closed cycle refrigerator. Measurements in applied magnetic field were taken using the M2 horizontal magnet cryostat at Chalk River Laboratories. In both experiments the sample was aligned in the (h,h,l) reciprocal lattice plane. The 2.6 Tesla magnetic field was aligned along the \mathbf{c} -axis (the moment direction) of the sample. A relatively high degree of collimation was used for both

experiments to achieve the high resolution required for the measurements. The collimation was set to 0.273° for the incident neutron beam and 0.152° for the diffracted neutron beam. This setup allowed excellent Q resolution, such that we could measure both the broad and sharp components of the scattering simultaneously.

Order parameter measurements of $\text{CsCo}_{0.83}\text{Mg}_{0.17}\text{Br}_3$ were performed in zero magnetic field as well as in a magnetic field of 2.6 Tesla applied along the **c**-axis (the moment direction). They were performed at the magnetic zone center $(\frac{2}{3}, \frac{2}{3}, 1)$ as neutron scattering at this ordering wavevector possessed the greatest intensity at low temperatures. In addition, detailed \vec{Q} scans were performed along the $(h, h, 1)$ and $(\frac{2}{3}, \frac{2}{3}, l)$ direction to examine the broad and sharp components of the scattering as a function of temperature. These were performed both in zero applied magnetic field and with an applied magnetic field of 2.6 Tesla directed along the **c**-axis.

4.3 Experimental Results

Figure 4.3 shows the neutron scattering intensity of the $[\frac{4}{3}, \frac{4}{3}, 1]$ magnetic Bragg peak for CsCoBr_3 and $[\frac{2}{3}, \frac{2}{3}, 1]$ for $\text{CsCo}_{0.83}\text{Mg}_{0.17}\text{Br}_3$ on a linear scale as a function of temperature. When plotted on a linear scale, no phase transitions are observed in $\text{CsCo}_{0.83}\text{Mg}_{0.17}\text{Br}_3$, in contrast to what is observed in CsCoBr_3 . However, the same data plotted on a logarithmic scale, as shown as the blue data in Fig. 4.4, shows a clear indication of a phase transition at $\sim 28\text{K}$. In addition we observe that the neutron scattering Bragg peak intensity at the ordering wavevector, $[\frac{2}{3}, \frac{2}{3}, 1]$, is suppressed at low temperatures with the application of a magnetic field along the **c**-axis when compared to that of the zero applied magnetic field data. Further analysis of the the full critical scattering will show the nature of these lower transitions in $\text{CsCo}_{0.83}\text{Mg}_{0.17}\text{Br}_3$.

Critical scattering scans were carried out on $\text{CsCo}_{0.83}\text{Mg}_{0.17}\text{Br}_3$ through the

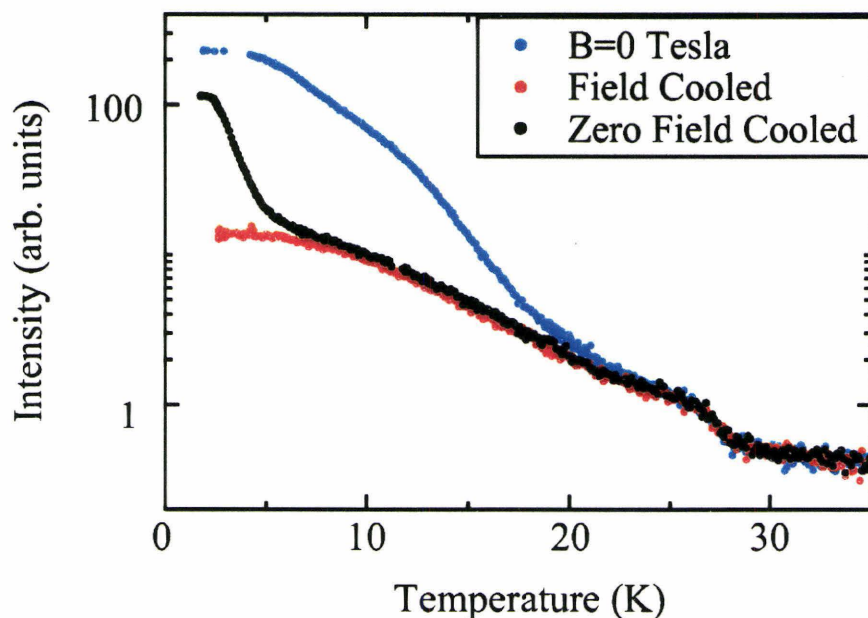


Figure 4.4: Peak neutron intensity plotted on a logarithmic scale at the magnetic zone center, $(\frac{2}{3}, \frac{2}{3}, 1)$ in $\text{CsCo}_{0.83}\text{Mg}_{0.17}\text{Br}_3$ as a function of temperature in both zero applied magnetic field (blue) and a magnetic field of $B=2.6$ T applied along the \mathbf{c} -axis. The red curve shows the field cooled measurements, while the black curve shows the zero field cooled measurements.

magnetic zone centers $(\frac{1}{3}, \frac{1}{3}, 1)$, $(\frac{2}{3}, \frac{2}{3}, 1)$ and along the $(\frac{2}{3}, \frac{2}{3}, L)$ direction. The full temperature dependence of the critical scattering at the $(\frac{2}{3}, \frac{2}{3}, 1)$ magnetic zone center for both zero applied field and for 2.6 Tesla applied along the \mathbf{c} -direction is shown in Fig. 4.5. For both $B=0$ T and $B=2.6$ T we see the onset of sharp magnetic Bragg peak at $\sim 28\text{K}$. We also see broad diffuse scattering appear near $\sim 28\text{K}$ that is also centered on magnetic zone center. Concentrating on the zero magnetic field data (top panel) we see that as the sample is cooled further the sharper feature at $(\frac{2}{3}, \frac{2}{3}, 1)$ builds up and begins to rapidly increase in intensity below $\sim 20\text{K}$. If we qualitatively look at the broad feature for the $B=0\text{T}$ case we see it build up gradually through the whole temperature range and slightly narrows below 15K . In contrast to the in-field

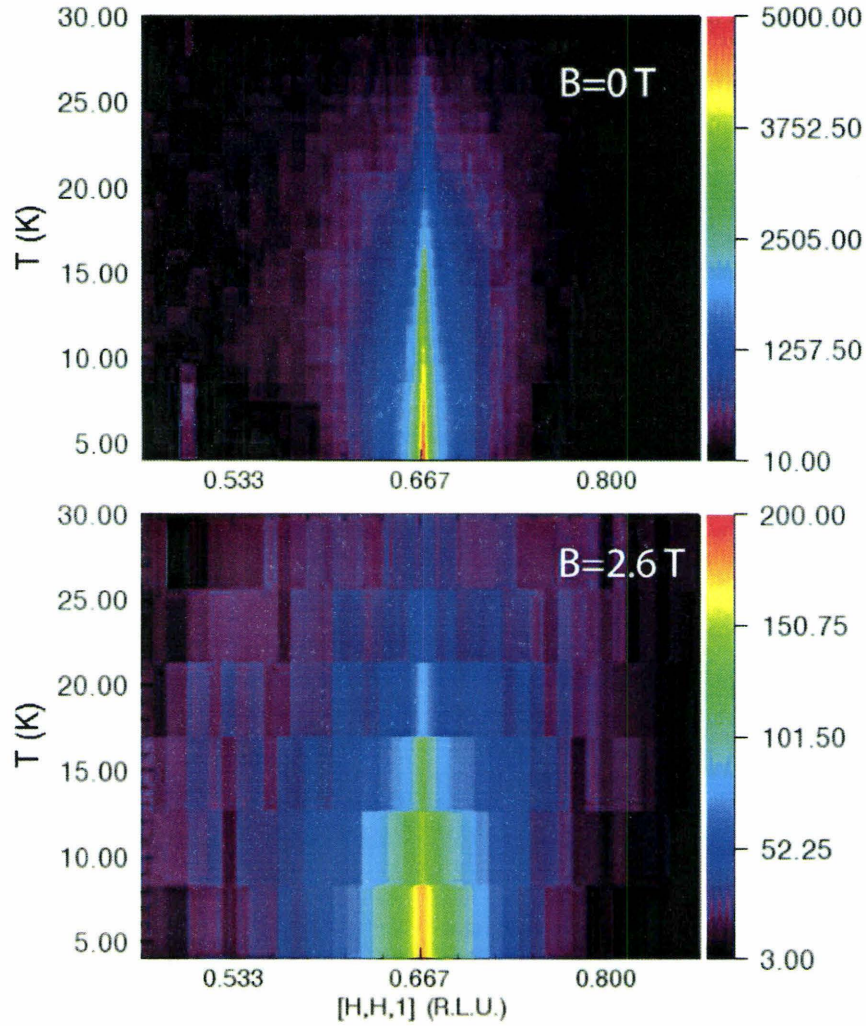


Figure 4.5: Critical neutron scattering scans along the $(H,H,1)$ direction in reciprocal space. The scattering from the magnetic zone center, $(\frac{2}{3}, \frac{2}{3}, 1)$ is shown in a colour contour map for $\text{CsCo}_{0.83}\text{Mg}_{0.17}\text{Br}_3$ as a function of temperature for zero applied field (top) and for $B=2.6\text{T}$ field (bottom). The magnetic field is applied along the c -axis for the data shown in the lower part of the plot.

data (B=2.6T) we observe the sharper feature to remain fairly weak through the entire temperature range, with no abrupt upturn at a function of temperature, as observed in the zero magnetic field case. The diffuse scattering qualitatively appears to be unaffected the application of a magnetic field. One difference we can note is the overall scale of the measured intensity, a maximum of ~ 5000 cts/mon for B=0T, and ~ 200 cts/mon for B=2.6T for base temperature. Finally we can note that the overall width of the sharp feature in the scattering at base temperature for B=2.6T is much broader than that corresponding to B=0T.

Let us take a closer look at a single representative scan along the (H,H,1) direction. Figure 4.6 shows such a scan along the [H,H,1] direction which passes through two magnetic zone centers, $(\frac{1}{3}, \frac{1}{3}, 1)$ and $(\frac{2}{3}, \frac{2}{3}, 1)$. From this we can see that there is no doubt that the scattering contains two components. These two components to the scattering imply both long and short range magnetic correlations are present. The data was analyzed by a convolution of the scattering cross section with the measured two-dimensional resolution function. The cross section, centered at each of the ordering wavevectors is described by the sum of an anisotropic Lorentzian and an anisotropic Lorentzian-squared component with a high temperature background subtraction. The calculated intensities included both the Co^{2+} magnetic form factor, and the neutron polarization factor. The inverse correlation lengths within the **ab**-plane and along the **c**-axis were allowed to differ, accounting for the strong anisotropic nature of the AF interactions within the material. The form of the scattering function fitted to the data was then:

$$S(\vec{Q}) = \frac{A_2}{\left[1 + \frac{q_a^2 + q_b^2}{\kappa_{ab}^2} + \frac{q_c^2}{\kappa_c^2}\right]^2} + \frac{A_1}{\left[1 + \frac{q_a^2 + q_b^2}{\kappa_{ab}^2} + \frac{q_c^2}{\kappa_c^2}\right]} \quad (4.2)$$

where $\vec{q} = \vec{Q} - \vec{Q}_{ord}$, and $\kappa = \xi^{-1}$. Where the κ 's are the half widths at half maximum and ξ is the correlation length.

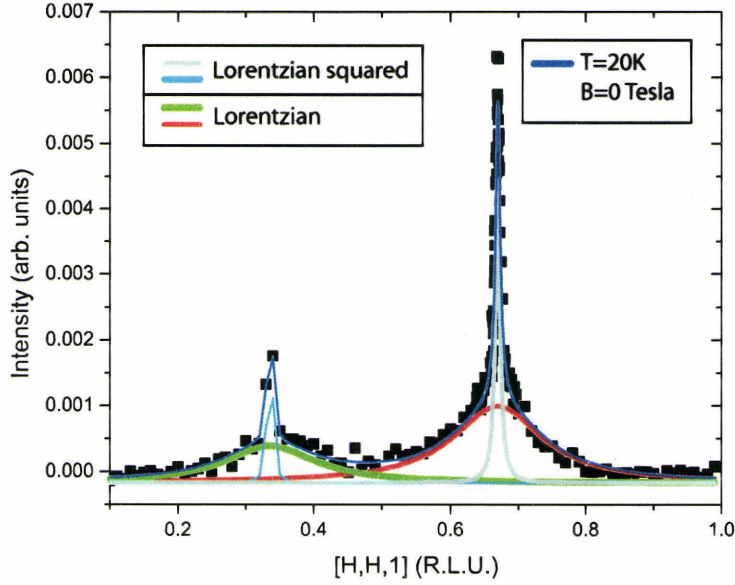


Figure 4.6: Representative scan in the $(H,H,1)$ direction at $T=20\text{K}$ in zero applied field. Fits to the two components (Lorentzian squared and Lorentzian) of the scattering. Peaking at each of the two magnetic zone centers $(\frac{1}{3}, \frac{1}{3}, 1)$ and $(\frac{2}{3}, \frac{2}{3}, 1)$ are displayed clearly.

The solid lines shown in Fig. 4.6 are fits to the data, a Lorentzian-squared term (first term in Eq.4.2) was used to describe the sharp feature and a Lorentzian term (second term in Eq. 4.2) to describe the broad feature. The Lorentzian-squared terms are shown in Fig 4.6 as the light blue and gray curves, while the Lorentzian terms are the green and red curves. The sum of all these terms describing the full scattering is the blue curve in Fig 4.6 and represents the data very well.

Typical fits of the data to Eq. 4.2 for several temperatures are shown in Figure 4.7. We present a side by side comparison of the zero field data with the $B=2.6\text{ T}$ applied field data for 3 temperatures. The fits of the data to Eq. 4.2 are shown as the solid blue lines and are of good quality. This functional form for the scattering (Eq.4.2) has been used experimentally before for other Random Field Ising

systems, such as $Co_xZn_{1-x}F_2$ [15] and $Fe_{0.6}Zn_{0.4}F_2$ [27].

If we examine the 25K data set in Figure 4.7 (top panel) we see that, for both zero and the applied magnetic field data, the overall amplitude of the scattering is about the same for the 2 components to the scattering. In addition the half width at half maximum (inverse correlation length) for both the zero and applied magnetic field data are approximately the same. Reducing the temperature slightly, ~ 5 K to 20K (middle panels in Fig. 4.7) already has a profound effect. At 20K we see that the overall amplitudes of the scattering are no longer the same, the zero magnetic field amplitude is ~ 2.5 times that of the applied magnetic field data. We can also observe that the ratio of the broad to sharp components is different in zero applied field compared with the applied magnetic field data. For $B=0$ T the amplitude of the sharp component is ~ 3 times that of the broad component, whereas for the $B=2.6$ T case the ratio of the amplitudes is about 1 to 1. Again if we compare the full width at half maximum of the two data sets, qualitatively we do not see much difference at 20K.

Reducing the temperature further to 12K (bottom panels in Fig. 4.7) we now see little resemblance between the two cases of $B=0$ T and $B=2.6$ T. The peak intensity of the scattering is vastly different now; the zero magnetic field data is ~ 15 times greater than that of the applied magnetic field data. The zero magnetic field data appears to be largely made up of a single sharp component, while the magnetic field data is composed primarily of the broad component. To examine this further and more quantitatively we will look at the parameters extracted from fitting the data to Eq. 4.2 for the broad and sharp components separately.

First we will investigate the temperature dependence of the sharp Lorentzian-squared term's width (κ_{ab} and κ_c) from Eq. 4.2. The top panel in Fig. 4.8 shows the fit parameter κ_{ab} [half width at half maximum (HWHM)] for the sharp, Lorentzian-

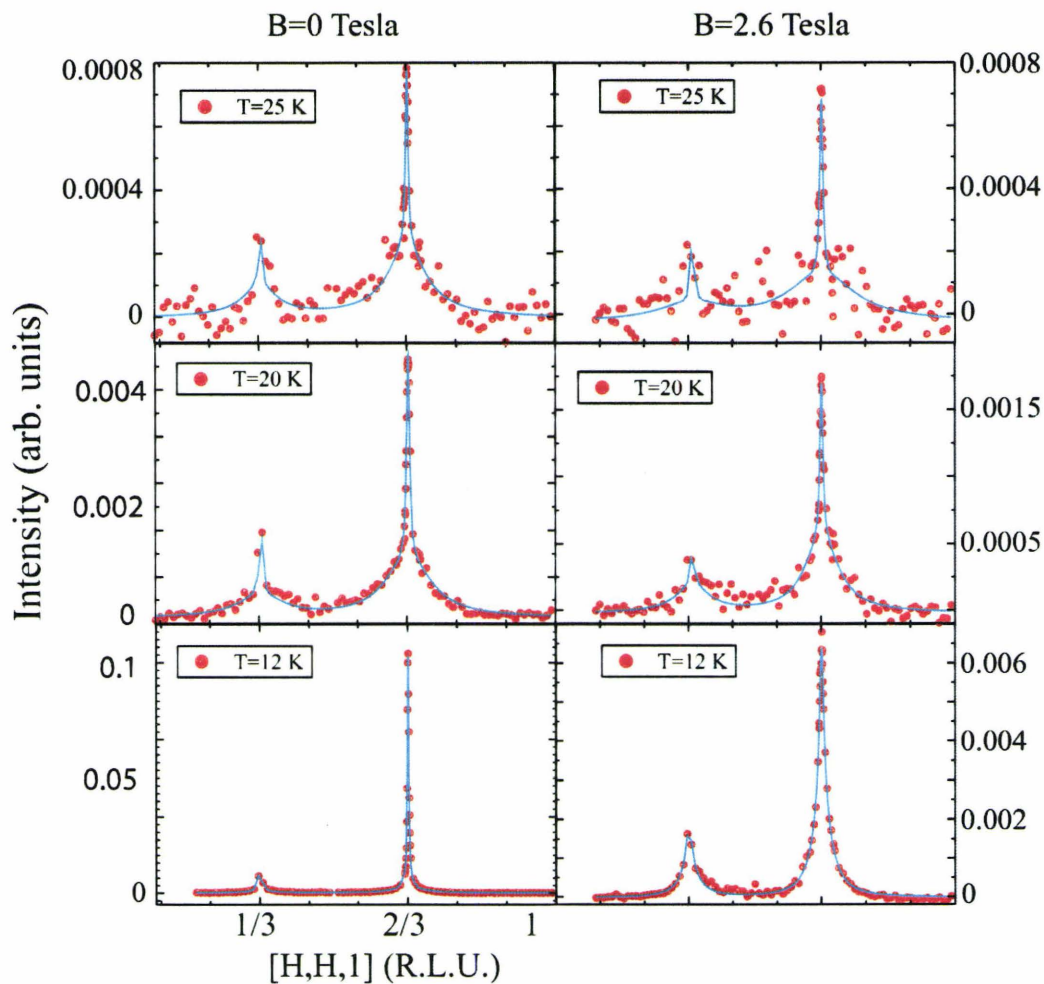


Figure 4.7: Representative critical neutron scattering scans along $(H,H,1)$ from which the colour contour map of Fig. 4.5 was constructed. These are shown for both zero applied magnetic field (left hand panels) and for $B=2.6\text{T}$ (right hand panels). Also, shown as the solid blue lines are fits to the critical scattering as described in the text.

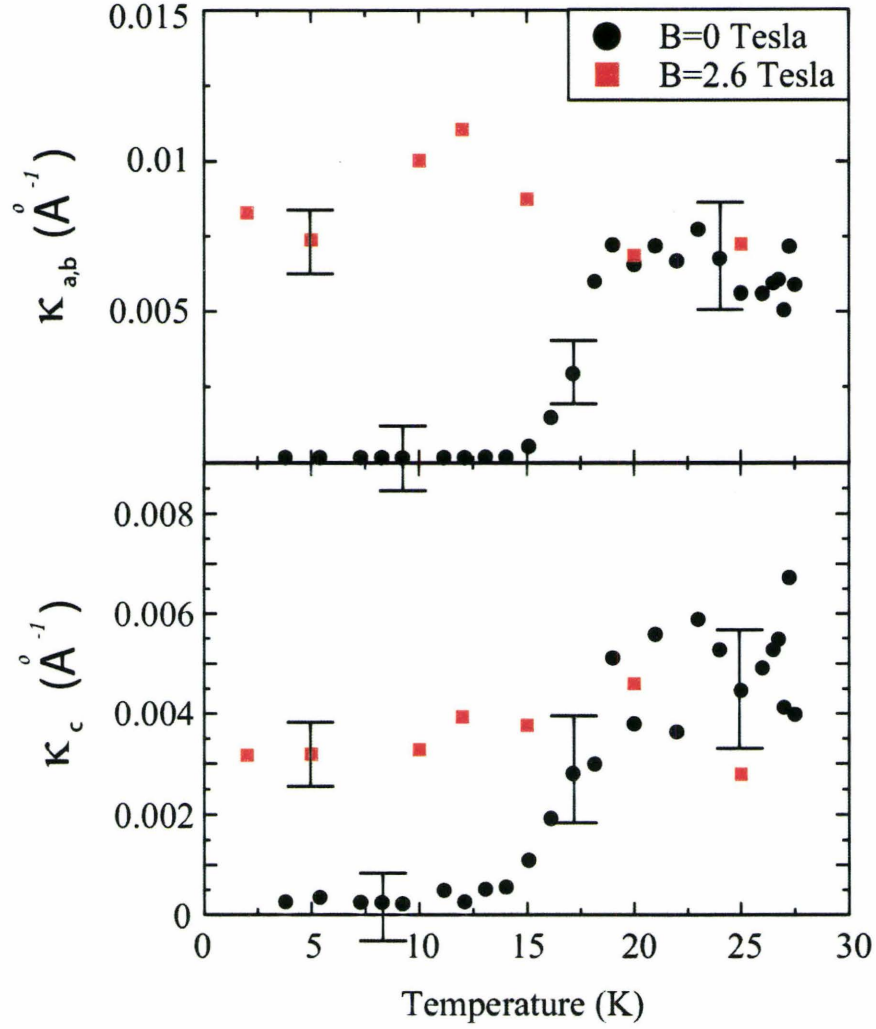


Figure 4.8: Fit parameters κ_{ab} (top panel) and κ_c (bottom panel) as a function of temperature extracted from fits to the data using Eq. 4.2. Black circles are appropriate to zero applied magnetic field, while red boxes are appropriate to $B=2.6$ T applied along the **c**-axis.

squared component from Eq. 4.2. κ_{ab} is related to the inverse correlation length in the **ab**-plane. Likewise the bottom panel of Fig. 4.8 shows the Lorentzian-squared component's κ_c , which is related to the inverse correlation length along the **c**-axis. The top panel in Fig. 4.8 shows the temperature dependence of κ_{ab} in zero applied magnetic field (black circles). Above $\sim 18\text{K}$, κ_{ab} is finite and constant with a value of $\sim 0.0075\text{\AA}^{-1}$. This corresponds to a correlation length of $\sim 130\text{\AA}$ in the **ab**-plane. As the temperature is reduced below 18K, the HWHM begins to decrease and approaches our resolution limit at $\sim 13\text{K}$. The same is also true for the parameter κ_c , where above a temperature of $\sim 18\text{K}$ the correlation length is $\sim 250\text{\AA}$ along the **c**-axis. When a magnetic field is applied along the **c**-axis as shown by the red boxes in Fig. 4.8, we see that across the whole temperature range the correlation length, κ_{ab} and κ_c , remain finite. The magnitude of the correlation length is similar to the $B=0\text{T}$ case above 18K.

The second term in Eq. 4.2 has been used to describe the broad scattering observed in the data. Figure 4.9 shows the temperature dependence of κ'_{ab} (top panel) and κ'_c (bottom panel) fit parameters of the Lorentzian term in Eq. 4.2 to the data. In Fig. 4.9 we see much broader correlation lengths when compared to the correlation lengths obtained for the Lorentzian-squared term from Eq. 4.2. These short ranged correlations, κ'_{ab} and κ'_c , do not show a qualitative difference between zero applied magnetic field and that of the applied magnetic field data. These correlations grow linearly below T_{n1} and reach their maximum below a temperature of $\sim 15\text{K}$.

In the **ab**-plane we see a correlation length (κ'^{-1}_{ab}) of $\sim 5\text{\AA}$ just below T_{n1} , which grows to a maximum of 10\AA below 15K for the Lorentzian term in equation 4.2. Below 15K these broad correlations remain constant with a value of $\sim 10\text{\AA}$ down to the lowest temperatures measured. The behaviour is similar along the **c**-axis. This short ranged correlation (κ'^{-1}_c) linearly increasing from $\sim 28\text{K}$ down to $\sim 15\text{K}$ then

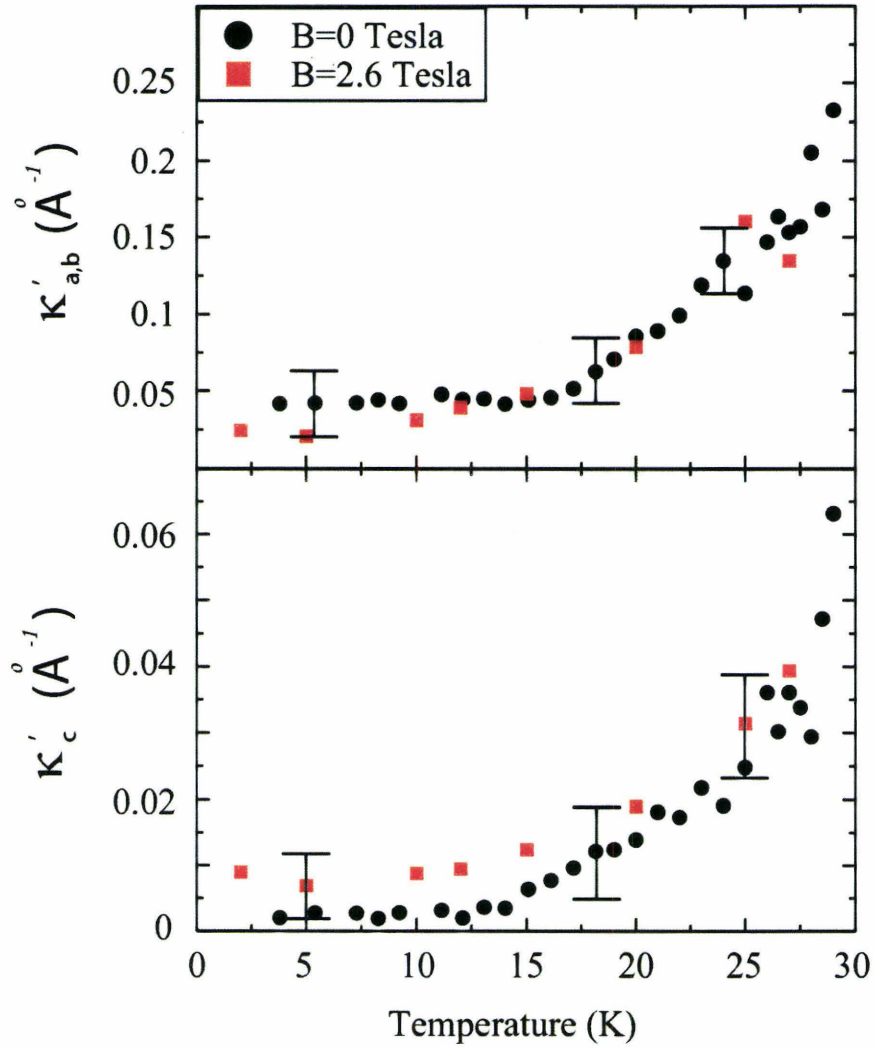


Figure 4.9: Inverse correlation lengths extracted from the fit parameters for the Lorentzian term in Eq. 4.2. Black circles are appropriate to zero applied magnetic field, while red boxes are appropriate to $B=2.6$ T applied along the c -axis.

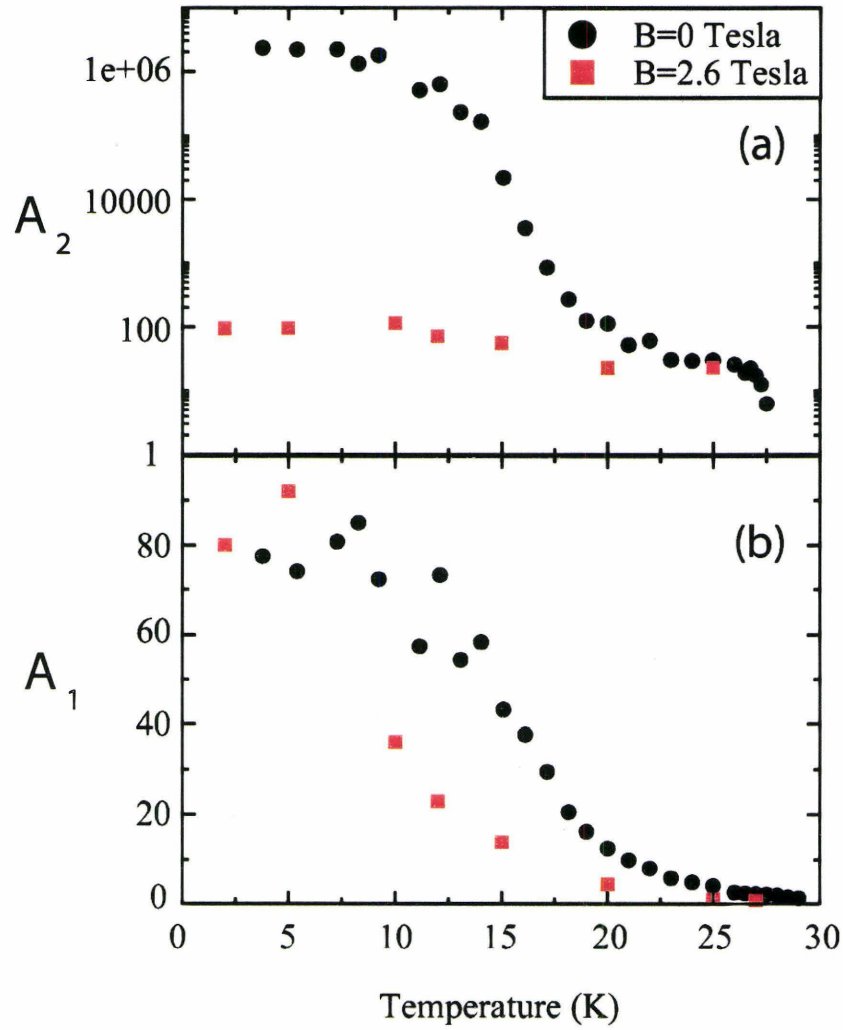


Figure 4.10: Amplitudes of the two components of the scattering observed in $\text{CsCo}_{0.83}\text{Mg}_{0.17}\text{Br}_3$ extracted from fits of the data to Eq. 4.2. Top panel (log scale) is the amplitude from the Lorentzian-squared term, A_2 . Bottom panel (linear scale) is the amplitude of the Lorentzian term A_1 . Zero field is represented by the black circles and in field data with $B=2.6\text{T}$ applied along the c -axis is represented by red boxes.

constant below 17K. With a maximum at low temperatures reaching $\sim 100\text{\AA}$.

Figure 4.10 shows the temperature dependence of the extracted parameters for the amplitudes A_2 and A_1 for the Lorentzian-squared and Lorentzian components in Eq. 4.2 respectively. The top panel of Fig. 4.10 shows the temperature dependence of A_2 on a log scale. The sharp Lorentzian-squared component, A_2 (top panel) shows downward curvature near 28K, indicating the onset of a phase transition. Below $\sim 18\text{K}$ A_2 displays an abrupt upturn in scattering amplitude as a function of temperature. This upturn of the scattering amplitude in zero field is not evident when a magnetic field is applied; in Fig. 4.10 the scattering amplitude, A_2 , is relatively flat as a function of temperature. The broad Lorentzian component, A_1 (bottom panel of Fig. 4.10) displays a gradual upturn for the whole temperature range for both the zero and $B=2.6\text{T}$ applied magnetic field. The strong magnetic field dependence is only observed in the long range correlations and not for the short ranged correlations.

We are consistently seeing an indication of a phase transition $\sim 18\text{K}$. In Fig. 4.8 we see that inverse correlation length from the Lorentzian-squared term, κ_{ab} and κ_c , both begin to approach our resolution limit below 18K and by 13K has reached our resolution limit in zero applied magnetic field. We were able to measure the in plane lattice constant, \mathbf{a} , as a function of temperature along the $[1,1,0]$ direction using the peak positions from the scans along the $[H,H,1]$ direction. At low temperatures it was noticed that the lattice distortions were only along the HH-direction, no appreciable distortion was seen along the L-direction. Thus the assumption was made that there is only an expansion of the lattice within the basal plane and not along the \mathbf{c} -axis. Figure 4.11, shows the temperature dependence of the \mathbf{a} -lattice constant. Above 20K the lattice parameter is constant within error. As we reduce the temperature below 20K the lattice starts to expand slightly in the basal plane. This expansion continues down to $\sim 13\text{K}$ then becomes constant again to the low temperature. This seems to

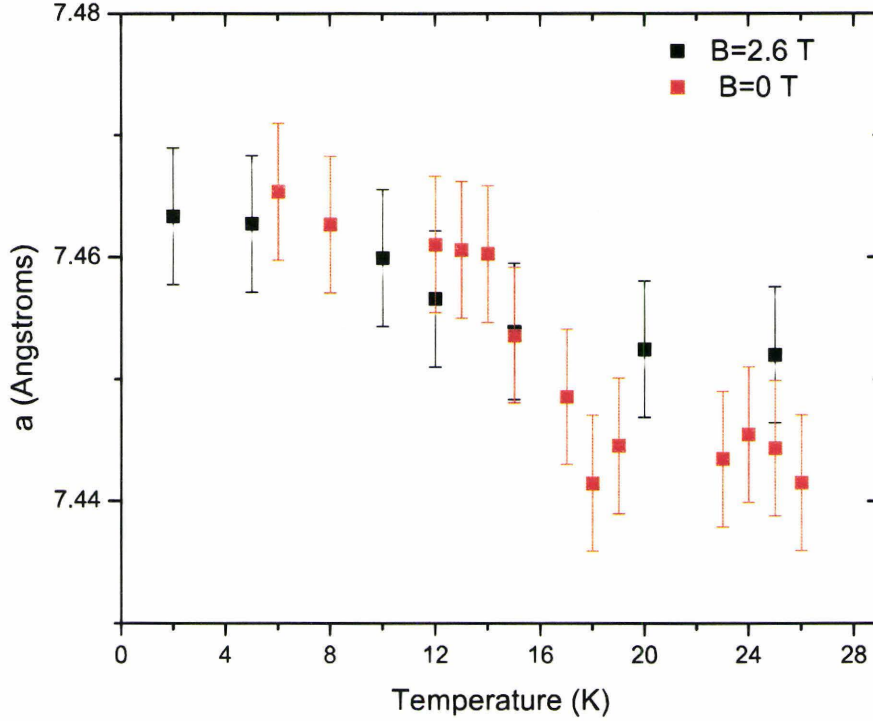


Figure 4.11: The temperature dependence of the \mathbf{a} -lattice parameter as measured from the $(\frac{2}{3}, \frac{2}{3}, 1)$ magnetic Bragg peak position.

coincide qualitatively with the low temperature phase transition into the fully ordered state at $T_{n3} 13K$. While the onset of the lattice distortion seems to coincide with the temperature that the Lorentzian-squared component inverse correlation length, κ_{ab} and κ_c , tends to zero. This expansion of the \mathbf{a} -lattice parameter is extremely small, $\sim 0.02\text{\AA}$ which explains why it was not observed before in work done by van Duijn [2]. When we apply a magnetic field of 2.6 Tesla along the c -direction (black boxes in Fig. 4.11) the lattice parameter is almost constant as a function of temperature, with a $\sim 0.01\text{\AA}$ expansion (\sim the error bars).

4.4 Discussion

At first glance the small amount of disorder seems to suppress the two known phase transitions in CsCoBr_3 , as seen in Fig. 4.3. If we examine the top panel of Fig. 4.10, the fit parameter A_2 in Eq. 4.2 on a linear scale we see that the two phase transitions in CsCoBr_3 are preserved in $\text{CsCo}_{0.83}\text{Mg}_{0.17}\text{Br}_3$. Panel (a) in Fig. 4.12 shows an abrupt increase in the magnetic Bragg peak intensity near T_{n3} . If we look on an expanded scale near 28K (panel (b) of Fig. 4.12) we see the indication of a phase transition near T_{n1} in $\text{CsCo}_{0.83}\text{Mg}_{0.17}\text{Br}_3$.

There is a possibility that the sample might be made up of a mixture of doped $\text{CsCo}_{0.83}\text{Mg}_{0.17}\text{Br}_3$ and pure CsCoBr_3 . This would mean that the sharp feature we see develop at T_{n1} originates from the part of the sample that is CsCoBr_3 and the diffuse magnetic scattering would originate from the $\text{CsCo}_{0.83}\text{Mg}_{0.17}\text{Br}_3$ part of the sample. We argue that this cannot be the case, as we see in Fig. 4.8 the fit parameters that

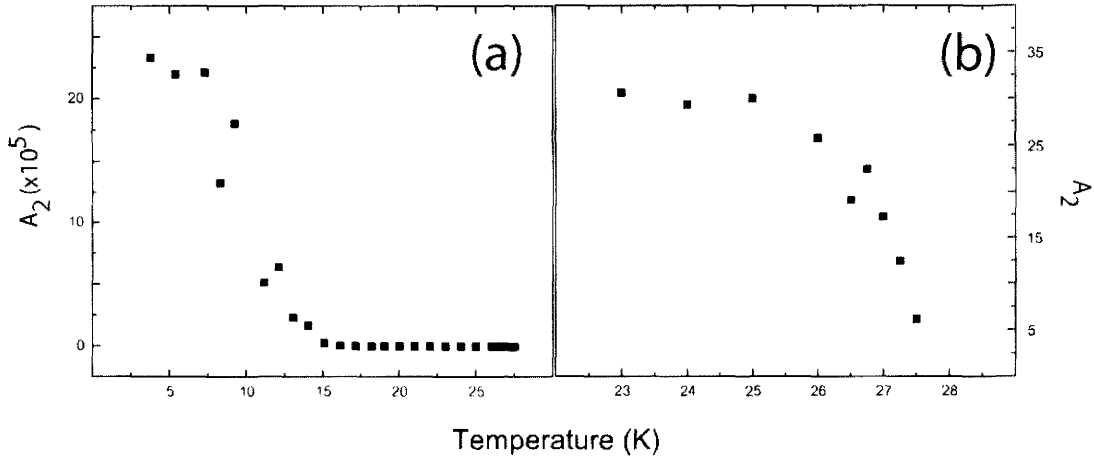


Figure 4.12: Amplitude of the Lorentzian-squared term, A_2 from fits of the data to Eq. 4.2 are plotted on a linear scale. (a) shows the full temperature range demonstrating the upturn near T_{n3} in pure CsCoBr_3 . (b) shows an expanded scale near the phase transition, T_{n1} .

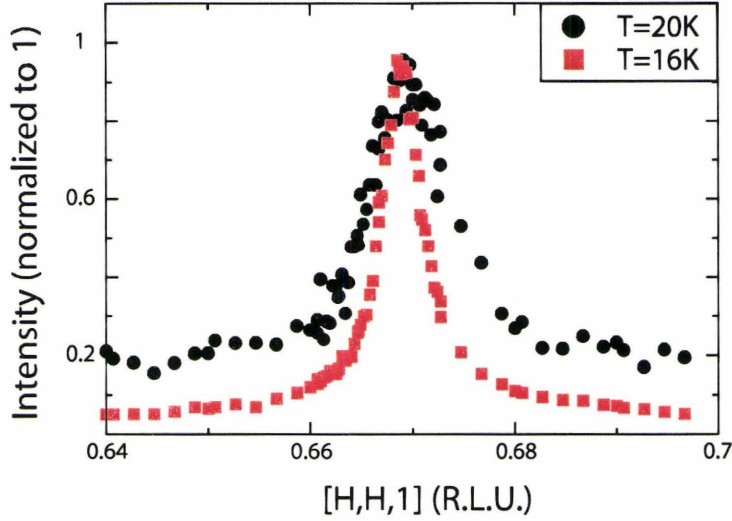


Figure 4.13: A comparison of two $[H,H,1]$ critical scattering scans near $[\frac{2}{3}, \frac{2}{3}, 1]$, both well below T_{n1} . Each has been normalized such that the peak intensity is 1.

describe the width of the Lorentzian-squared term in Eq. 4.2 (κ_{ab} and κ_c) are not resolution limited below T_{n1} . This effect can be observed by a simple comparison of the raw data below T_{n1} . Figure 4.13 shows scans through the $[\frac{2}{3}, \frac{2}{3}, 1]$ magnetic Bragg peak well below T_{n1} in zero applied magnetic field. These scans have been normalized such that the peak intensity for the scan is 1 so that a qualitative comparison of the widths can be made. If the sharp Lorentzian-squared component was the result of an impurity phase of pure CsCoBr_3 present within the sample we would expect that for both these scans taken at 20K and 16K they would be resolution limited. It is obvious from the raw data presented in Fig. 4.13 that at $T=20\text{K}$ the sharp component is not resolution limited.

We will interpret our results within the framework of the Random Field Ising Model (RFIM). A typical RFIM experimental system is that of an antiferromagnetic material on a square lattice that has been doped with magnetic holes (as discussed in Chapter 3). To realize the random field one must apply a magnetic field

along the moment direction. The system then nucleates domains pinned to the magnetic vacancies. CsCoBr_3 is a more complex realization of a random field state as it is on a triangular lattice instead of a square lattice. In addition there are two different ordered magnetic phases as a function of temperature that must be considered. In $\text{CsCo}_{0.83}\text{Mg}_{0.17}\text{Br}_3$ we will need to consider both the effect of the magnetic vacancies within a particular ordered phase and the effect the magnetic field will have on that particular ordered phase of CsCoBr_3 .

4.4.1 CASE 1: Partially Paramagnetic Phase

We will first consider how magnetic vacancies will effect the three sublattice state of CsCoBr_3 . Figure 4.2(a) displays an illustration of the three sublattice state of CsCoBr_3 , and we will introduce Mg ions into this lattice. These Mg ions will have the net effect of removing a spin from the lattice. In zero applied magnetic field there is one site on the lattice in which the Mg ion can sit without having an effect on the magnetic exchange energy present, the paramagnetic sublattice. The quenched vacancies will nucleate domains where the Mg ion is coincident with the paramagnetic sub lattice. Three such domains are depicted in Figure 4.14(a), with domain walls running between them.

With the application of a magnetic field along the \mathbf{c} -axis, the system would also like to nucleate RF domains to minimize the energy. This time if the field is strong enough, the system will nucleate these domains on the down sub-lattice (opposite the magnetic field). We would be in the field dominated regime if the magnetic field energy, $g\mu_B\Delta SH$, is greater than that of the in-plane interaction energy, $2J' \sum_{n.n.} S_i S_j$.

$$g\mu_b\Delta SH \sim 4\mu_B(1)(2.6T) \sim 0.6meV \quad (4.3)$$

$$2J' \sum_{n.n.} (S_i S_j) \sim 2 * 0.0096Thz * 6 * \frac{1}{2} * \frac{1}{2} \sim 0.13meV \quad (4.4)$$

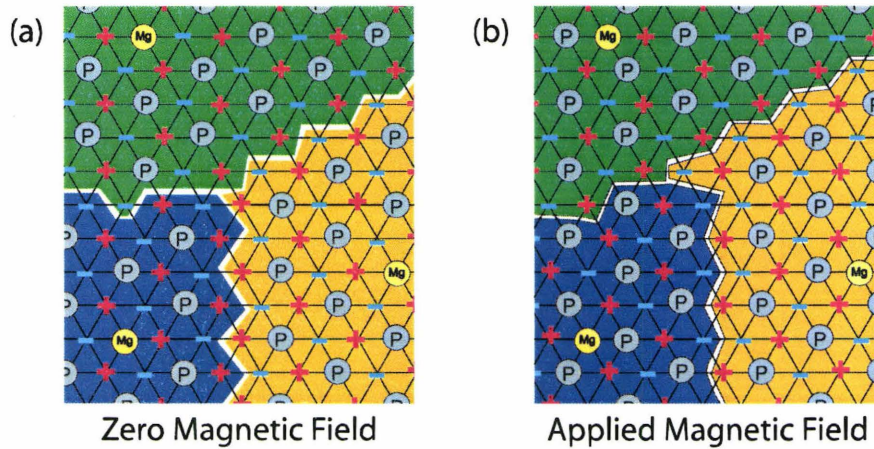


Figure 4.14: Role of nonmagnetic atoms in generating a random field domain state in the Partially Paramagnetic state of CsCoBr_3 . a) Zero magnetic field, the nonmagnetic Mg ion couples to the paramagnetic site. b) Applied magnetic field along the c -axis, the nonmagnetic Mg ion couples to the lattice sites which would have aligned opposite to the applied magnetic field in the absence of the vacancy.

Here we can see by the rough calculation that we should be within the field dominated regime with a $H=2.6$ Tesla field applied. The fact that we observe such a strong field induced effect in $\text{CsCo}_{0.83}\text{Mg}_{0.17}\text{Br}_3$ also strongly suggests we are in a field dominated regime at $H=2.6\text{T}$. An illustration of domains that would be formed in the field dominated regime can be found in Figure 4.14(b). The domains would nucleate instead such that the vacancies reside on the spin down sites in the lattice and not on the paramagnetic site, as in the zero magnetic field case.

It is then expected that in the partially paramagnetic phase of $\text{CsCo}_{0.83}\text{Mg}_{0.17}\text{Br}_3$ the RF state would be present for both an applied magnetic field and for zero applied magnetic field. Our data supports this argument, as we see in the inverse correlation length measurements for both the κ and κ' shown in Figure's 4.8 and 4.9 respectively. Both of these correlation lengths are finite within the partially paramagnetic phase of CsCoBr_3 indicating that domain structures are present.

4.4.2 CASE 2: Low Temperature Ordered Phase

The low temperature ordered phase of CsCoBr_3 as illustrated in Figure 4.2(b) is that of three-sub lattice ordered antiferromagnet. The effect of quenched magnetic vacancies in this ordered phase will be different than that of the partially paramagnetic phase. With the paramagnetic site now absent there is nothing to break the symmetry between the two possible states around an impurity without the application of a magnetic field. We still expect that with an applied magnetic field will form a RF state, as it would in a 2-D square lattice random field problem. Figure 4.15 is an illustration of how the magnetic vacancy couples to the low temperature phase of CsCoBr_3 for both zero magnetic field and a magnetic field applied along the \mathbf{c} -axis. In zero applied magnetic field, we see that two of the magnetic vacancies (Mg ions) now have the same local environment while the third is in a different environment. While in the presence of a sufficiently strong magnetic field the vacancies will reside on a unique down sublattice, thereby encouraging the domain state shown in Fig. 4.15b.

Fig. 4.8 shows that in zero magnetic field the inverse correlation length (κ_{ab}, κ_c) approaches zero below T_{n3} , the fully ordered phase of CsCoBr_3 . When we apply the magnetic field to the system we see in Fig. 4.8 that within the low temperature phase there is a persistent measurable correlation length (ξ_{ab}, ξ_c) . In fact the correlation length is fairly constant for all measured temperatures below T_{n1} while the magnetic field is applied. We therefore associate the sharp Lorentzian-squared term from Equation 4.2 with the RF state, and not the broad Lorentzian term, as was previously thought[2].

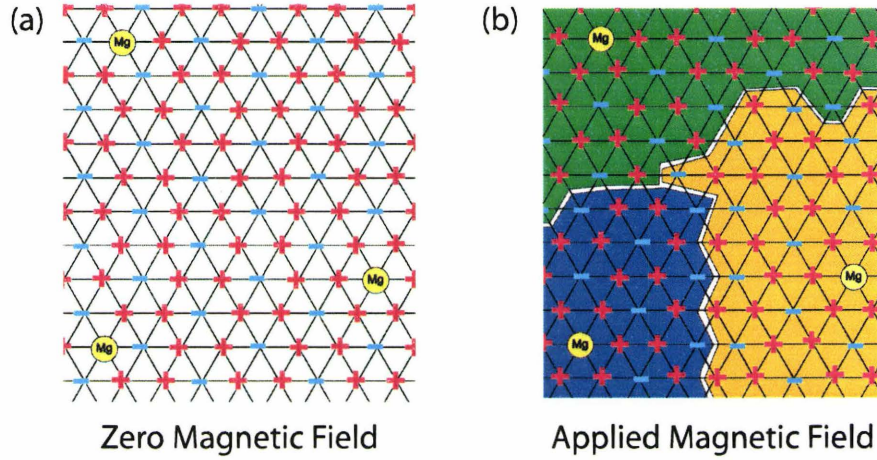


Figure 4.15: Role of nonmagnetic atoms in generating a random field domain state in the low temperature ordered phase of CsCoBr_3 . a) Zero magnetic field, the system will not be in the RF state and the system should fully order. b) Applied Magnetic Field along the c -axis, the nonmagnetic Mg ion couples to the lattice sites which would have aligned opposite to the applied magnetic field in the absence of the vacancy.

4.5 Conclusion

Our critical scattering study of $\text{CsCo}_{0.83}\text{Mg}_{0.17}\text{Br}_3$ has shown that weak dilution does not wipe out the phase transitions in $\text{CsCo}_{0.83}\text{Mg}_{0.17}\text{Br}_3$. We see clear evidence that magnetic Bragg peaks appear at $T_{n1} \sim 28\text{K}$ as seen in Figure 4.5. The system instead enters a Random Field Domain state in the temperature range from 28K-18K for zero applied field. Then as the system's paramagnetic sites begins to order we lose this Random Field Domain state in zero field. As we approach the long range ordered state at $\sim 13\text{K}$ there is a slight lattice distortion which begins at 18K. With the application a magnetic field along the c -axis of 2.6 Tesla the system remains in the domain state to the lowest temperatures measured. We see that the Lorentzian-squared term (the sharp component to the scattering) is in fact the component associated with the Random Field Domain state.

Bibliography

- [1] R. J. Birgeneau, H. Yoshizawa, R. A. Cowley, G. Shirane, and H. Ikeda, *Phys. Rev. B* **28**, 1438 (1983).
- [2] J. van Duijn, B. D. Gaulin, M. A. Lumsden, J. P. Castellan, and W. J. L. Buyers, *Phys. Rev. Lett.* **92**, 077202 (2004).
- [3] N. W. Ashcroft and N. D. Mermin, *Solid State Physics* (Harcourt College Publishers, New York, 1976).
- [4] G. Squires, *Introduction to the Theory of Neutron Scattering* (Dover Publications, Inc., New York, 1978).
- [5] S. W. Lovesey, *Theory of Neutron Scattering from Condensed Matter* (Oxford University Press, New York, 1987).
- [6] M. F. Collins, *Magnetic Critical Scattering* (Oxford University Press, New York, 1989).
- [7] J. D. Jackson, *Classical Electrodynamics* (John-Wiley and Sons, Toronto, 1975).
- [8] B. Warren, *X-ray Diffraction* (Addison-Wesley Publishing Company, Don Mills, Ontario, 1969).

- [9] M. Plishke and B. Bergersen, *Equilibrium Statistical Physics* (World Scientific Publishing Co. Pte. Ltd., Singapore, 1987).
- [10] M. Fisher, *J. Math. Phys.* **5**, 944 (1964).
- [11] L. Ornstein and F. Zernicke, *Proc. Sect. Sci. K. Med. Akad. Wet.* **17**, 793 (1914).
- [12] R. Birgeneau, R. A. Cowley, G. Shirane, and H. Yoshizawa, *Journal of Statistical Physics* **34**, 817 (1984).
- [13] Y. Imry and S. K. Ma, *Phys. Rev. Lett.* **35**, 1399 (1975).
- [14] S. Fishman and A. Aharony, *J. Phys. C* **12**, L729 (1979).
- [15] M. Hagen, R. Cowley, S. Satija, H. Yoshizawa, G. Shirane, R. Birgeneau, and H. Guggenheim, *Phys. Rev. B* **28**, 2602 (1983).
- [16] R. A. Cowley, H. Yoshizawa, G. Shirane, M. Hagen, and R. J. Birgeneau, *Phys. Rev. B* **30**, 6650 (1984).
- [17] R. A. Cowley, H. Yoshizawa, G. Shirane, and R. J. Birgeneau, *Z. Rev. B* **58**, 15 (1985).
- [18] H. Diep, *Magnetic Systems with Competing Interactions* (World Scientific, Singapore, 1996).
- [19] J. E. Greedan, *J. Mat. Chem.* **11**, 37 (2001).
- [20] S. E. Nagler, W. J. L. Buyers, R. L. Armstrong, and B. Briat, *Phys. Rev. B* **27**, 1784 (1983).
- [21] W. B. Yelon, D. E. Cox, and M. Eibschutz, *Phys. Rev. B* **12**, 5007 (1975).
- [22] A. Farkas, B. D. Gaulin, Z. Tun, and B. Briat, *J. Appl. Phys* **69**, 6167 (1991).

- [23] M. Mao, B. D. Gaulin, R. B. Rogge, and Z. Tun, *Phys. Rev. B* **66**, 184432 (2002).
- [24] R. B. Rogge, Y. S. Yang, Z. Tun, B. D. Gaulin, J. A. Fernandez-Baca, R. M. Nicklow, and A. Harrison, *J. Appl. Phys* **73**, 6451 (1993).
- [25] S. E. Nagler, W. J. L. Buyers, R. L. Armstrong, and R. A. Ritchie, *J. Phys. C* **17**, 4819 (1984).
- [26] Y. S. Yang, F. Marsiglio, M. Madsen, B. D. Gaulin, R. B. Rogge, and J. A. Fernandez-Baca, *Phys. Rev. B* **65**, 212408 (2002).
- [27] D. Belanger, A. King, and V. Jaccarino, *Phys. Rev. B* **31**, 4538 (1985).

Chapter 5

Two and Three Dimensional Incommensurate Modulation in Optimally-Doped $\text{Bi}_2\text{Sr}_2\text{CaCu}_2\text{O}_{8+\delta}$

This chapter incorporates the article "Two and Three Dimensional Incommensurate Modulation in Optimally-Doped $\text{Bi}_2\text{Sr}_2\text{CaCu}_2\text{O}_{8+\delta}$ ", Phys. Rev. B, **73**,174505(2006). The x-ray experiments were performed on the rotating anode x-ray generator at McMaster University and in part on the 4-ID-D beamline at the Advanced Photon Source in Argonne Il. The samples were prepared by H.A. Dabkowska, A. Nabialek and G. Gu using the floating zone image furnace at McMaster University. The experiments and subsequent data analysis was performed by myself under the guidance of B.D. Gaulin. The article was authored by myself and B.D. Gaulin.

Two and Three Dimensional Incommensurate Modulation in Optimally-Doped $\text{Bi}_2\text{Sr}_2\text{CaCu}_2\text{O}_{8+\delta}$ ¹

J.P. Castellan¹, B.D. Gaulin^{1,2}, H.A. Dabkowska¹, A. Nabialek³, G. Gu⁴, X. Liu⁵,
and Z. Islam⁶

¹Department of Physics and Astronomy, McMaster University, Hamilton, Ontario,
L8S 4M1, Canada

²Canadian Institute for Advanced Research, 180 Dundas St. W., Toronto, Ontario,
M5G 1Z8, Canada

³Institute of Physics, Polish Academy of Sciences, Al, Lotnikow 32/46, 02-668
Warsaw, Poland

⁴Institued of Physics, Brookhaven National Laboratory, Upton, New York
11973-5000, USA

⁵Department of Physics, University of California, San Diego, CA, 92093, U.S.A.

⁶Advanced Photon Source, Argonne National Laboratory, Argonne, IL, 60439,
U.S.A.

¹©2006 The American Physical Society

Abstract

X-ray scattering measurements on optimally-doped single crystal samples of the high temperature superconductor $\text{Bi}_2\text{Sr}_2\text{CaCu}_2\text{O}_{8+\delta}$ reveal the presence of three distinct incommensurate charge modulations, each involving a roughly fivefold increase in the unit cell dimension along the \mathbf{b} -direction. The strongest scattering comes from the well known $(h, k \pm 0.21, l)$ modulation and its harmonics. However, we also observe broad diffraction which peak up at the L values complementary to those which characterize the known modulated structure. These diffraction features correspond to correlation lengths of roughly a unit cell dimension, $\xi_c \sim 20 \text{ \AA}$ in the \mathbf{c} direction, and of $\xi_b \sim 185 \text{ \AA}$ parallel to the incommensurate wavevector. We interpret these features as arising from three dimensional incommensurate domains and the interfaces between them, respectively. In addition we investigate the recently discovered incommensurate modulations which peak up at $(1/2, k \pm 0.21, l)$ and related wavevectors. Here we explicitly study the L -dependence of this scattering and see that these charge modulations are two dimensional in nature with weak correlations on the scale of a bilayer thickness, and that they correspond to short range, isotropic correlation lengths within the basal plane. We relate these new incommensurate modulations to the electronic nanostructure observed in $\text{Bi}_2\text{Sr}_2\text{CaCu}_2\text{O}_{8+\delta}$ using STM topography.

5.1 Introduction

High temperature superconductivity is observed and has been extensively studied across several families of layered copper oxides[1]. While the structure of families of these materials differ in detail, they are all comprised of stackings of CuO_2 rectangular layers, with so-called charge reservoir layers in between. The CuO_2 layers can occur in isolation, or appear in bi- or trilayer assemblies. One of the most extensively studied of these materials is $\text{Bi}_2\text{Sr}_2\text{CaCu}_2\text{O}_{8+\delta}$, which is known to display an optimal superconducting T_C of ~ 93 K [1]. As shown in Fig. 5.1, it is a bilayer superconductor with orthorhombic symmetry and lattice parameters of $a \sim b \sim 5.4 \text{ \AA}$, and $c = 30.8 \text{ \AA}$ [2]. As such two CuO_2 bilayers appear within the unit cell separated by $\sim 15.4 \text{ \AA}$ along c .

$\text{Bi}_2\text{Sr}_2\text{CaCu}_2\text{O}_{8+\delta}$ has been the high temperature superconducting sample of choice for studies using surface-sensitive techniques such as photoemission[3] and scanning tunneling microscopy (STM)[4]. This is due to the relative ease of producing clean, cleaved surfaces of $\text{Bi}_2\text{Sr}_2\text{CaCu}_2\text{O}_{8+\delta}$ at low temperature, a consequence of its extreme quasi-two dimensionality, even compared with other families of layered high temperature superconductors, such as $\text{YBa}_2\text{Cu}_3\text{O}_{7-\delta}$ and $\text{La}_{2-x}\text{Sr}_x\text{CuO}_4$. These techniques and the information they provide on electronic structure have been very important to the general field of high temperature superconductivity, and $\text{Bi}_2\text{Sr}_2\text{CaCu}_2\text{O}_{8+\delta}$ has been crucial to these studies. Unfortunately, the two dimensional nature of the material has also resulted in relatively thin single crystals being grown (with thicknesses in the c direction of as much as, but typically smaller than, a few millimeters). This has precluded, or made very difficult, the study of the $\text{Bi}_2\text{Sr}_2\text{CaCu}_2\text{O}_{8+\delta}$ family by experimental techniques which require a large volume of material, such as single crystal neutron scattering[5].

The structural detail for which $\text{Bi}_2\text{Sr}_2\text{CaCu}_2\text{O}_{8+\delta}$ is perhaps best appre-

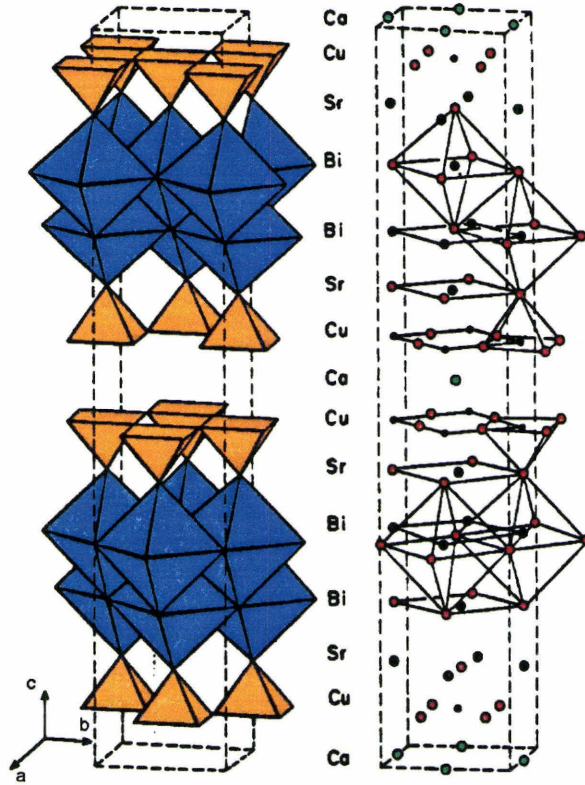


Figure 5.1: A schematic diagram depicting one unit cell of $\text{Bi}_2\text{Sr}_2\text{CaCu}_2\text{O}_{8+\delta}$ is shown. The light (orange) pyramids represent CuO_2 plus apical oxygen complexes, while the dark (blue) octahedra represent BiO_2 plus apical oxygen atom complexes. The Cu ions reside at the center of the base of the light pyramids, while the Bi ions reside at the center of the octahedra. The CuO_2 and BiO_2 bilayer thicknesses are 3.3 \AA and 3.2 \AA , respectively, while the bilayer-bilayer separation, $c/2$, is $\sim 15.4 \text{ \AA}$.

ciated is the incommensurate modulation it possesses within its basal plane. This incommensurate modulation has been observed by different techniques including, x-ray[6], neutron[7] and electron diffraction[8]; scanning tunneling microscopy[9], and electron microscopy[10]. This complex crystal structure has been described in terms of two interpenetrating periodic crystals, each of which modulate the other[11], with supporting experimental evidence from neutron scattering[12].

The modulation is one-dimensional, running along the **b**-direction in the basal plane, and it is the modulation (as opposed to a difference between a and b lattice parameters) that is responsible for the lower-than-tetragonal symmetry of the structure. The incommensurate modulation is characterized by multiple harmonics, and the first order harmonic corresponds to a periodicity of roughly 5 unit cells along **b**. Interestingly, it appears that $\text{Bi}_2\text{Sr}_2\text{CaCu}_2\text{O}_{8+\delta}$ crystals typically grow untwinned, likely a consequence of strains which would develop between orthogonal modulations. This is in contrast to other families of high temperature superconductors which can be produced in an untwinned state, but only with considerable effort in preparation.

5.2 Materials and Experimental Methods

The $\text{Bi}_2\text{Sr}_2\text{CaCu}_2\text{O}_{8+\delta}$ single crystal samples were grown by the traveling solvent floating zone techniques using a Crystal Systems Inc. image furnace. The growth was performed from premelted polycrystalline rods in 2 atmospheres of flowing O_2 . The rods were counter-rotated at 30 rpm and the growth speed was 0.2 mm/hour. The resulting single crystals were carefully extracted from a large boule, and had approximate dimensions of 10 mm \times 5 mm \times 0.1 mm, where the thin dimension was parallel to the **c** axis. Although thin, the single crystals were of excellent quality with mosaic spreads less than 0.07 degrees, and a superconducting transition temperature, determined by SQUID magnetometry, of $T_C \sim 92$ K with a width of ~ 2 K.

Two sets of x-ray scattering measurements were performed on these samples. Measurements were made using a Cu-rotating anode source and a triple axis spectrometer at McMaster University. These measurements employed Cu-K α radiation and utilized a pyrolytic graphite monochromator. The sample was mounted in a closed cycle refrigerator and placed in a four-circle goniometer. Four sets of slits were employed to define the incident and scattered beams.

A high resolution diffraction setup at the Advanced Photon Source synchrotron radiation facility was used to study a subset of the modulations with greater precision. These measurements were performed on the 4-ID-D beamline at an x-ray energy of 16 keV. This beamline is equipped with a double-crystal Si(111) monochromator. A Pd-coated bent mirror was used to focus the beam to a spot size of $180 \times 220 \mu\text{m}$ at the sample. A flat Pd mirror was used to further suppress higher order harmonics. The thin single crystal sample was placed in a closed cycle refrigerator. A Ge(111) analyser was used to reduce background and to improve resolution.

5.3 Experimental Results

5.3.1 Three Dimensional Modulated Structure

Synchrotron x-ray scattering scans of the form $(0, K, 0)$ and $(0, K, 1)$ are shown in Fig. 5.2. This data is plotted on a logarithmic intensity scale, and was taken at $T=10$ K, although no significant temperature dependence was observed to this scattering to temperatures as high as 300 K. A clear pattern of diffraction peaks is observable at incommensurate wavevectors of the form $(0, 4-n \times \tau, L)$ for $\tau=0.21$, corresponding to a roughly 5 unit cell modulation, and at all harmonics ($n=1,2,3,4$) which we studied. Two distinct lineshapes are clearly present. One is very sharp, resolution limited, and these peaks alternate in harmonic for a particular L . This is to say that the even

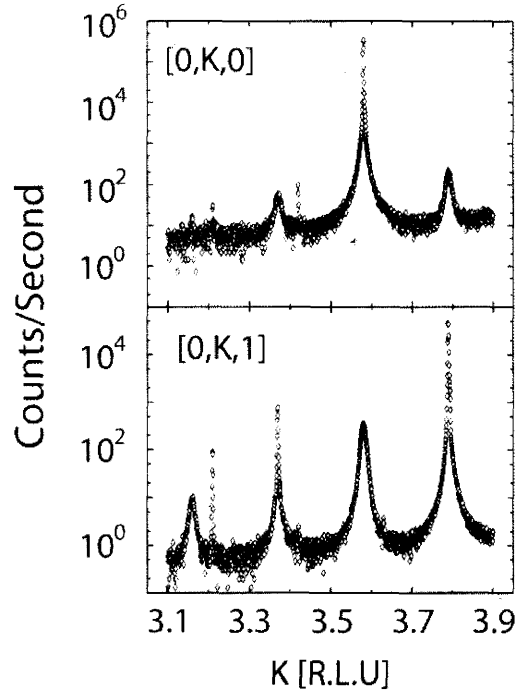


Figure 5.2: Synchrotron X-ray scattering scans on a logarithmic intensity scale along $[0,K,0]$ (top panel) and $[0,K,1]$ (lower panel) in $\text{Bi}_2\text{Sr}_2\text{CaCu}_2\text{O}_{8+\delta}$. A total of four harmonics of the modulated structure with the form $(0, 4-n\times\tau, L)$ are observed at both $L=0$ and $L=1$, and they clearly alternate between resolution-limited and broad along both K and L (see Fig. 5.3). The broad component to the scattering is well described by a Lorentzian-squared lineshape (see Fig. 5.4).

harmonic, $n=2$ ($K=3.58$), is clearly sharp in K for $L=0$, while it is the odd harmonics, $n=1$ ($K=3.79$) and $n=3$ (3.37), which are sharp for $L=1$.

Figure 5.3 shows x-ray scattering data, plotted on a logarithmic intensity axis, taken with the rotating anode source. This data examines the systematic L dependence of the scattering shown in Fig. 5.2. Once again this data is taken at 10 K and scans of the form $(0, 4, L)$, $(0, 3.79, L)$, and $(0, 3.58, L)$ are shown in the top, middle and bottom panels of Fig. 5.3, respectively. Consistent with the data shown in Fig. 5.2, two sets of incommensurate diffraction peaks are seen in the bottom two panels, which alternate with L , between a sharp, resolution-limited lineshape, and a broad diffraction feature.

Clearly, at alternate harmonics one observes a much broader lineshape. This is considered quantitatively in Fig. 5.4, where broad diffraction features at $(0, 3.58, 1)$ and $(0, 3.58, 5)$ are plotted as a function of K and L on a linear intensity scale. This data was fit to a Lorentzian-squared form along both b^* and c^* :

$$S(\mathbf{Q}) = \frac{A}{\left[1 + \frac{(\mathbf{Q}-\mathbf{Q}_0)^2}{\kappa^2}\right]^2} \quad (5.1)$$

yielding correlation lengths of $\xi_b = \frac{1}{\kappa_b} \sim 185 \text{ \AA}$ and $\xi_c = 20 \text{ \AA}$.

Together these data illustrate two co-existing incommensurate structures one of which displays resolution-limited long range order in three dimensions, while the other displays three dimensional, albeit highly anisotropic, short range order. We interpret the anisotropic, short-range order diffraction peaks as arising from stacking faults in the incommensurate modulation.

For simplicity, we discuss this three dimensional scattering as if a single harmonic characterized the incommensurate structure. Domains of well ordered modulated regions give rise to the resolution limited peaks at say $(0, 3.79, L)$ with $L=\text{odd}$. The $L=\text{odd}$ requirement implies a phase shift of $\pi, 3\times\pi, 5\times\pi$, between either CuO_2

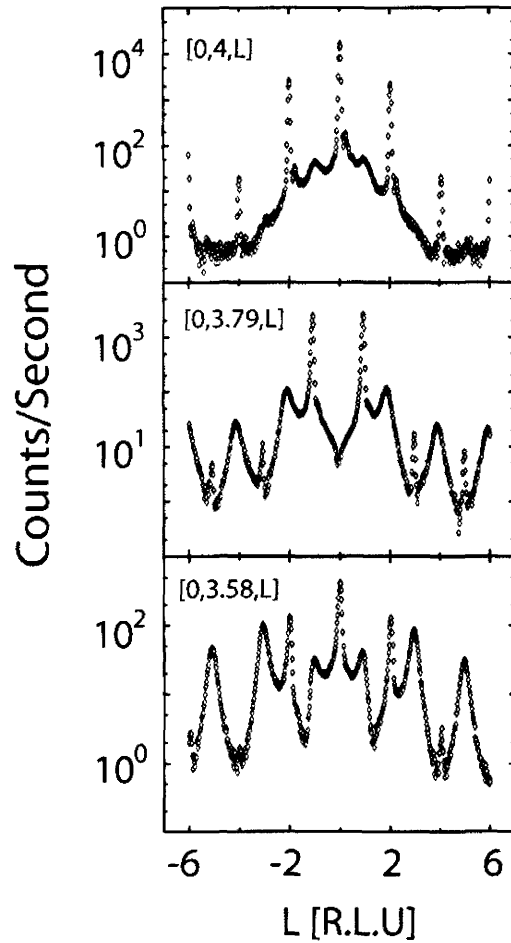


Figure 5.3: Rotating anode x-ray scattering measurements on a logarithmic intensity scale show the L -dependence of the principal Bragg peaks, such as $[0,4,L]$ (top panel); the first order harmonic of the modulated structure $[0, 3.79, L]$ (middle panel); and the second order harmonic of the primary modulated structure $[0, 3.58, L]$ (bottom panel). The harmonics alternate with L between resolution-limited Bragg scattering and broad scattering which is well described by a Lorentzian-squared lineshape (see Fig. 5.4).

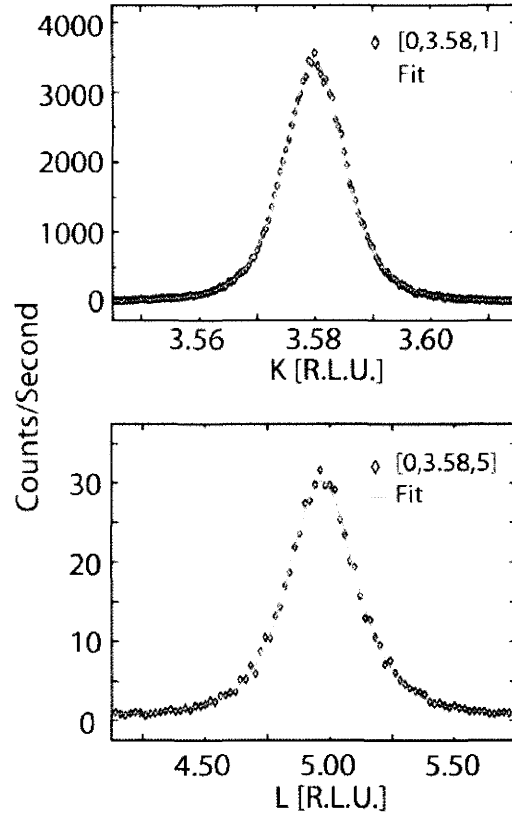


Figure 5.4: X-ray scattering scans along K (top) and L (bottom) taken from Figs. 5.2 and 5.3 and plotted on a linear intensity scale. Both plots show the second order harmonics of the primary modulation $[0, 3.58, 1]$ and $[0, 3.58, 5]$. These positions correspond to wavevectors with broad (as opposed to resolution-limited) lineshapes. Also shown is the fit to each lineshape using a Lorentzian-squared form, Eq. 5.1, which is clearly excellent. As described in the text, this lineshape is typically used to describe the three dimensional random field domain state in disordered magnets.

bilayers (or equivalently BiO₂ bilayers) which are separated from each other by half a unit cell along *c* (see Fig. 5.1). That is, the modulated structure within a particular bilayer is π out of phase with that immediately above and below it.

In contrast the *L*-dependence of the broad diffraction peaks, such as (0, 3.79, *L*) with *L*=even, implies that this incommensurate modulation is in phase with that in the bilayer immediately above and below it. Also, as the correlation length along *c* is roughly a unit cell dimension, we have a very natural interpretation that these diffraction features arise from the interface between two bulk domains, but which are out of phase with respect to each other. While the domain interfaces, attributed to the broad diffraction peaks, are anisotropic with $\xi_c \sim 20 \text{ \AA}$ and $\xi_a \sim 185 \text{ \AA}$, we classify all of the (0, $4 \pm n \times \tau$, *L*) superlattice diffraction peaks as being three dimensional in nature, as all of the superlattice peaks are localized around a particular point in reciprocal space, as opposed to being organized into rods or sheets of scattering, as is known to be relevant to two and one dimensional structures, respectively.

5.3.2 Two Dimensional Modulated Structure

X-ray scattering measurements using the rotating anode source were also extended to look for additional charge modulation. Additional modulation, distinct from that at (0, $4 - n \times \tau$, *L*) and discussed above, involving a doubling of the periodicity along *a* have recently been reported in Bi₂Sr₂CaCu₂O_{8+ δ} by Megtert and co-workers[13], and also by ourselves[14]. Scans performed along H, going through the second order harmonic of the three dimensional modulation, (0, $4 - 2 \times 0.21$, 5), are shown in the bottom two panels of Fig. 5.5. The (0, 3.58, 5) second order harmonic of the three dimensional modulation is easily observable at the ~ 10 counts/second level. However, we also observe peaks at ($\pm 1/2$, 3.58, 5) at the 0.4 counts/second level on a ~ 0.2 counts/second background. While weak, this H=1/2 modulation is clearly resolved

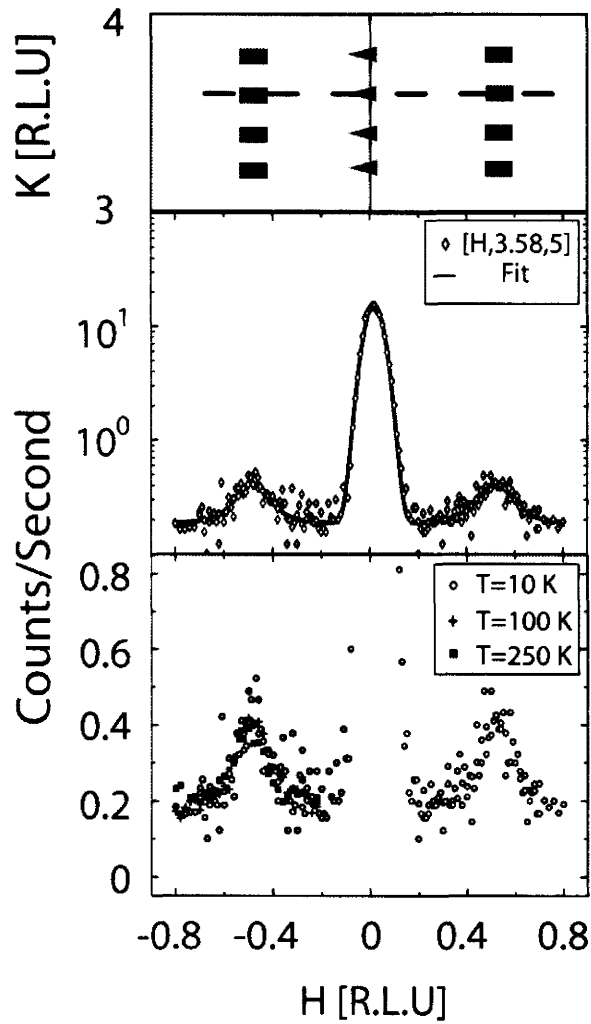


Figure 5.5: X-ray scattering scans of the form $[H, 3.58, 5]$ which show the new modulated structure corresponding to a doubling of the unit cell along a is shown. The dashed line in the upper panel shows where the scans reside in reciprocal space, passing through the second order harmonic of the primary modulation. The middle and lower panels show these scans on logarithmic (middle) and linear (bottom) intensity scales, with Lorentzian lineshapes (Eq. 5.2) fit to the data. The bottom panel also demonstrates the lack of temperature dependence to this scattering below room temperature.

in the middle panel of Fig. 5.5. The bottom panel of Fig. 5.5 shows three data sets at $T=10$ K, 100 K, and 250 K, at the $(-1/2, 3.58, 5)$ wavevector and demonstrates that, like the $H=0$ modulations discussed above, the new $H=1/2$ modulations have little or no temperature dependence to temperatures as high as room temperature. The peaks shown in Fig. 5.5 were fit to a resolution-convoluted Lorentzian form:

$$S(\mathbf{Q}) = \frac{A}{[1 + \frac{(\mathbf{Q}-\mathbf{Q}_0)^2}{\kappa^2}]} \quad (5.2)$$

and the $(\pm 1/2, 3.58, 5)$ peaks were found to be characterized by a correlation length of $\xi_a \sim 27 \text{ \AA}$ along \mathbf{a} .

Figure 5.6 shows x-ray scattering scans of the form $(1/2, K, 5)$ passing between $K=3$ and 4, and showing $(1/2, 4-n\times\tau, 5)$ for $\tau=0.21$ and $n=1,2,3$, and 4. The top panel of Fig. 5.6 locates these scans in reciprocal space as the dashed lines. Also shown in the bottom panel of Fig. 5.6, are scans of the form $(0, K, 0)$ and $(0, K, 1)$ taken under precisely the same experimental conditions as the $(1/2, K, 5)$ scan. This data shows K scans through $(0, 3.58, 0)$ and $(0, 3.79, 1)$ which are both resolution-limited Bragg peaks (see Fig. 5.2). We therefore conclude that the peaks shown in the $(1/2, K, 5)$ scans of Fig. 5.6 are not resolution limited. We can provide an excellent fit to this data, shown as the solid line in Fig. 5.6, with a resolution-convoluted Lorentzian lineshape, Eq. 5.2. We then extract a relatively short correlation length along \mathbf{b} for this $H=1/2$ modulation of $\xi_b \sim 27 \text{ \AA}$, very similar to the correlation length ξ_a , extracted from the $(H, 3.58, 5)$ scans of Fig. 5.5.

Figure 5.7 shows L-scans of the form $(1/2, 4-n\times\tau, L)$ for $n=2$ in the top panel, that is $(1/2, 3.58, L)$, and for $n=1, 2, 3$, and 4 in the bottom panel. Also shown in the top panel is a background scan taken at $(0.3, 3.45, L)$. Remarkably these scans, from $L=-10$ to 10, show almost no L -dependence at all; that is rods of scattering characteristic of two dimensional structures. The scattering is weakly

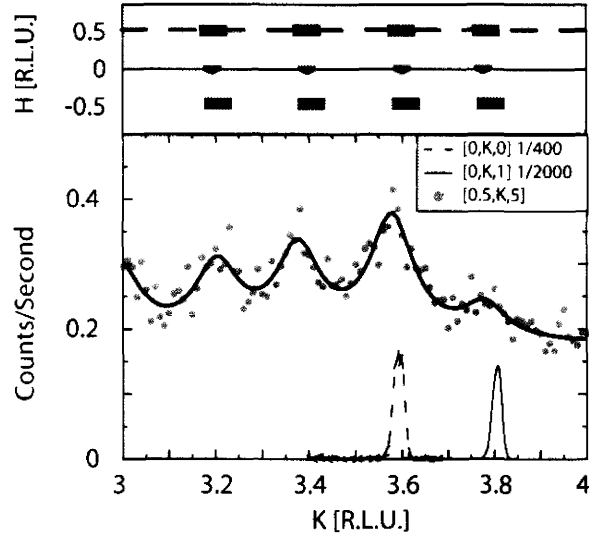


Figure 5.6: X-ray scattering scans of the form $[1/2, K, 5]$ which display the new modulated structure corresponding to a doubling of the unit cell along \mathbf{a} is shown. The upper panel shows where the scans reside in reciprocal space, passing through the first four harmonics of this new modulated structure. The data in the bottom panel is fit to Lorentzian lineshapes (Eq. 5.2) centered at each of the four harmonic positions along \mathbf{K} . Also shown for comparison in the same panel are \mathbf{K} scans of the first and second harmonics of the primary modulated structure, whose linewidth defines the instrumental resolution.

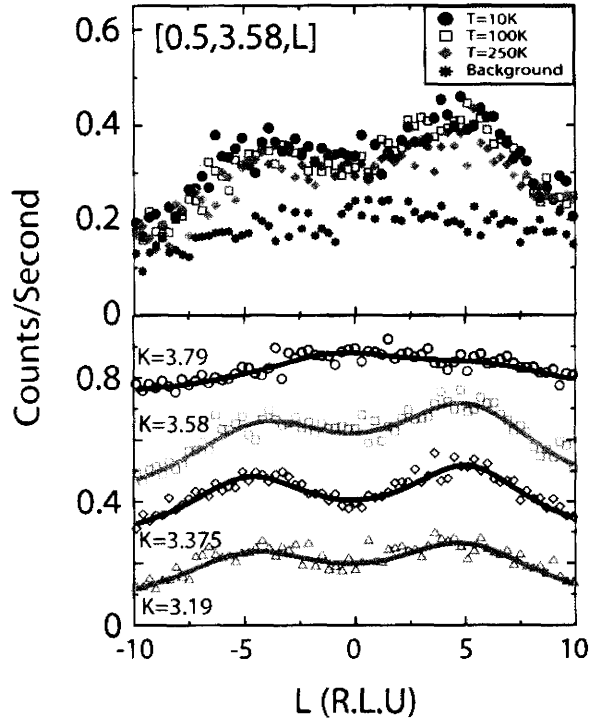


Figure 5.7: X-ray scattering scans of the form $[1/2, K, L]$ which observe the new modulated structure corresponding to a doubling of the unit cell along \mathbf{a} are shown. The top panel shows L-scans of the second order ($K=3.58$) harmonic of this scattering, at different temperatures below 250 K, as well as a background scan of the form $[.3, 3.45, L]$. The lower panel shows the L dependence of each of the first four harmonics of this structure at 10 K. Remarkably over the 10 Brillouin zones from $L=10$ to $L=-10$, a near complete rod of scattering is observed for the first order harmonic ($K=3.79$), while higher order harmonics peak up weakly at $L=\pm 5$.

peaked at $L \sim \pm 5$, but extends over all L values measured. These scans were also carried out as a function of temperature, and again, as seen in the top panel of Fig. 5.7, one sees little or no temperature dependence to temperatures as high as room temperature. These results on the new $(1/2, 4-n\times\tau, L)$ modulations extend those reported earlier[13, 14] by explicitly determining L dependencies. We also see that our results give approximately isotropic correlation lengths within the **a-b** plane a factor of two smaller than those reported by Megtert and collaborators[13]. However, the Megtert et al. work does not discuss the form to which the scattering was fit to extract their correlation length, and hence a quantitative comparison is not possible at present.

The extreme extended nature of this scattering in L helps us understand why the scattering is so weak at any one position, and therefore why it is difficult to observe, and has escaped observation until recently. As the scattering is broad in both H and K (with correlation lengths $\xi_{ab} \sim 27 \text{ \AA}$ and rod-like in L , the *integrated* intensity of these $H=1/2$ incommensurate modulations is in fact quite appreciable. However the scattering is sufficiently diffuse so as to make its *peak* intensity very weak, down by a factor of 10^6 compared with principal Bragg peaks of the three dimensional structure, such as $(0, 4, 0)$. The characteristics of the three sets of scattering from incommensurate modulations are summarized in Table 1.

5.4 Discussion and Relation to STM Imaging

Our results show three distinct sets of incommensurate modulation in optimally-doped $\text{Bi}_2\text{Sr}_2\text{CaCu}_2\text{O}_{8+\delta}$, which co-exist at all temperatures below room temperature. Two of these are three dimensional in nature, with scattering centered on definite Bragg points in reciprocal space. This scattering is peaked up at $(H, 4-n\times\tau, L)$ and alternates as a function of harmonic at a particular L , and as a function of L at

	$(0, 4 - \delta, \text{even})$	$(0, 4 - \delta, \text{odd})$	$(1/2, 4 - \delta, L)$
In-plane correlations	$\xi_b \sim 185 \text{ \AA}$ (Lorentzian) ²	res. lim.	$\xi_a \sim \xi_b \sim 27 \text{ \AA}$ Lorentzian
Out of plane correlations	$\xi_c \sim 20 \text{ \AA}$ (Lorentzian) ²	res. lim.	Rodlike

Table 5.1: The characteristics of the scattering at the incommensurate wavevectors with three distinct lineshapes is summarized. As discussed in the text, $(0, 3.79, 0)$, $(0, 3.37, 0)$ and $(0, 3.58, 1)$ are typical of $(0, 4-\delta, \text{even})$ wavevectors; while $(0, 3.58, 0)$, $(0, 3.79, 1)$, and $(0, 3.37, 1)$ are typical of $(0, 4-\delta, \text{odd})$ wavevectors (see Figs. 2 and 3).

a particular harmonic, between resolution-limited peaks and those characterized by finite and anisotropic correlation lengths in all three directions.

The broad, $(H, 4-n \times \tau, L)$, incommensurate peaks are extremely well described by a Lorentzian-squared lineshape (Fig. 5.4). This is an interesting result in itself, as a sum of Lorentzian plus Lorentzian-squared terms is typically used to model diffuse magnetic scattering in random field Ising model (RFIM) magnets, which display random local symmetry breaking[15]. Three dimensional RFIM systems, such as $\text{Co}_x\text{Zn}_{1-x}\text{F}_2$ [16] and $\text{Fe}_x\text{Zn}_{1-x}\text{F}_2$ [17] in the presence of an applied magnetic field, show magnetic diffraction features with negligible Lorentzian weight, and thus their diffuse scattering is also very well described by a Lorentzian-squared form. Such a scattering form implies a pair-correlation function in three dimensions which falls off with distance as $\exp(-\kappa r)$, and is characteristic of a domain wall state[15]. Our results for κ_{ab} imply these domains are hundreds of angstroms across, with domain walls which are a single unit cell in extent in the c direction. This small spatial extent, $\xi_c \sim 20 \text{ \AA}$ in the c direction is consistent with local stacking defects. As $\text{Bi}_2\text{Sr}_2\text{CaCu}_2\text{O}_{8+\delta}$ is

more generally the $m=2$ member of the $\text{Bi}_2\text{Sr}_2\text{Ca}_{m-1}\text{Cu}_m\text{O}_{4+2m+\delta}$ family, the nature of the stacking fault is likely a missing Ca-layer. As such the domain wall itself is expected to locally be the $m=1$ member of the family: $\text{Bi}_2\text{Sr}_2\text{CuO}_{6+\delta}$. This is a relatively low T_C superconductor ($T_C \sim 10$ K) with a smaller c-axis, $c=24.6 \text{ \AA}$ [18] than $\text{Bi}_2\text{Sr}_2\text{CaCu}_2\text{O}_{8+\delta}$. Such a scenario has recently been proposed from high resolution electron microscopy measurements performed on the same crystals as those studied here[19].

The most remarkable result we report is the confirmation and characterization of the incommensurate modulation corresponding to a doubling of the periodicity along H and giving rise to rods of scattering of the form $(1/2, 4-n\times\tau, L)$ at all L. The scattering tends to be weakly peaked near $L=\pm 5$. This indicates out-of-phase, or π , correlations *within* a bilayer. As shown schematically in Fig. 1, the CuO_2 and BiO_2 bilayer thicknesses are almost identical, at $\sim 3.3 \text{ \AA}$. Such correlations give rise to weak peaks at wavevectors of $\pi/(\text{bi-layer thickness}) \sim \pi/3.3 \text{ \AA} = 0.95 \text{ \AA}^{-1} \sim L=5\times 2\pi/c$. As can be seen in Fig. 5.7, this tendency for the two dimensional rods of scattering to peak up near $L\sim \pm 5$ seems to be strongest for the second and third order harmonics of this incommensurate structure $(1/2, 3.58, L)$ and $(1/2, 3.375, L)$, and is not seen at all for the 1st order harmonic $(1/2, 3.79, L)$ which appears to be truly rod-like in nature.

Several interesting questions arise from the observation of this two dimensional incommensurate structure. First, from what does it arise? For example, is it a surface effect, or can it arise from an intrinsically two dimensional charge inhomogeneity which exists throughout the full volume of the crystal?

The scattering geometry employed in all of the measurements presented in this paper is *transmission* geometry, and hence it is very unlikely that the rod-like incommensurate scattering we observe in Figs. 5.5, 5.6, and 5.7 is due to surface

structure of any kind, even though it is two dimensional in nature. We are then left with the intriguing conclusion that the scattering originates from the bulk of the crystal, but is nonetheless two dimensional in nature.

A second question which arises is, given that the $\text{Bi}_2\text{Sr}_2\text{CaCu}_2\text{O}_{8+\delta}$ family of superconductors have been studied for more than 15 years, has this type of structure been observed in previous experiments? We believe the answer to this question is yes, and consider earlier STM measurements of the surface structure of $\text{Bi}_2\text{Sr}_2\text{CaCu}_2\text{O}_{8+\delta}$. Room temperature measurements by Sugita et al.[20] identified a superstructure with periodicity of two unit cells along the \mathbf{a} direction. In addition, we reconsider higher resolution, low temperature STM images of the surface structure of $\text{Bi}_2\text{Sr}_2\text{CaCu}_2\text{O}_{8+\delta}$ discussed several years ago by Pan and co-workers[9]. Figure 5.8 shows an STM image of the [001] cleaved surface of near-optimally doped $\text{Bi}_2\text{Sr}_2\text{CaCu}_2\text{O}_{8+\delta}$ from Pan et al[9]. The well known $(0, 0.21, L)$ modulation is seen as the periodic lighter stripes which run along the vertical direction in the STM image and which have an approximate periodicity of 5 unitcell dimensions along \mathbf{b} . However, superposed on the light stripes is an “S-like” dark modulation, which has a periodicity of 2 unit cells along the stripe; that is along the \mathbf{a} -direction. This additional modulation in the structure appears superposed on every light stripe within the field of view. As such one expects its manifestation in reciprocal space to appear at wavevectors of the form $(1/2, 0.21, L)$, exactly where we observe the two dimensional rods of scattering.

Further, careful examination of the STM image shows that the S-modulation along \mathbf{a} is not a perfect pattern, but is characterized by phase slips both along \mathbf{a} and between S-modulations imposed on adjacent light stripes. Consequently, such substructure would not give rise to resolution-limited Bragg peaks, but rather to diffuse peaks characterized by relatively short correlation lengths. Again, this is fully consistent with the two dimensional rods of scattering which we have observed at

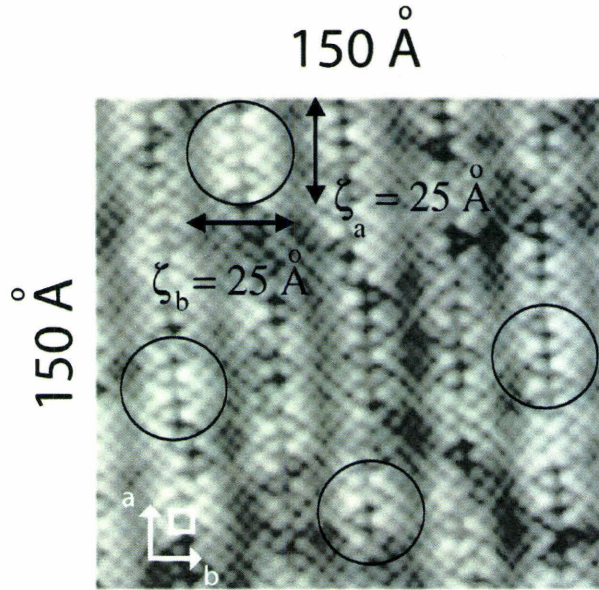


Figure 5.8: The correlation areas of the new modulated structure corresponding to a doubling of the unit cell along a extracted from our x-ray scattering analysis are superposed on STM topographs[9] of the surface of $\text{Bi}_2\text{Sr}_2\text{CaCu}_2\text{O}_{8+\delta}$. Our measurements indicate isotropic short range correlations with a correlation length of $\sim 27 \text{ \AA}$, and these correspond very well to the extent of the “S” microstructure which appears to be imprinted on the primary modulated structure of $\text{Bi}_2\text{Sr}_2\text{CaCu}_2\text{O}_{8+\delta}$, as observed in real space with the STM measurements.

($1/2, 4-n \times \tau, L$), wherein the correlation length measured in the ab-plane was found to be approximately isotropic, $\xi_{ab} \sim 27 \text{ \AA}$. We have superposed correlation-areas within the ab plane using the correlation lengths extracted from our x-ray scattering measurements, onto the STM images[9] of the structure of the cleaved [001] plane of optimally-doped $\text{Bi}_2\text{Sr}_2\text{CaCu}_2\text{O}_{8+\delta}$, and the agreement between the two is remarkably good. The S-modulation within the STM image was not commented on by Pan et al[9]. However, as STM is a very surface sensitive probe, it provides little information as to the behaviour of this substructure into the bulk of the material. It would therefore be possible to associate such structure in an STM experiment with a surface effect. However, we reiterate that our x-ray scattering measurements, performed in transmission geometry, are very *insensitive* to the surface. We conclude that the two dimensional modulated structure we observe in x-ray scattering is the same as the electronic inhomogeneity observed with STM, and that it originates from charge inhomogeneity within the bulk of the $\text{Bi}_2\text{Sr}_2\text{CaCu}_2\text{O}_{8+\delta}$ superconductor.

Finally, one can ask how general is the phenomenon of charge inhomogeneity in different families of high temperature superconductors? Of course, electronic phase separation is implied within a variety of models for high temperature superconductivity, most prominently those involving “stripes”[21]. However, is there related diffuse scattering evidence in other high temperature superconductors?

The answer again appears to be yes, with the recent reports of a four unit cell superstructure with correlation lengths of $\sim 20 \text{ \AA}$ within the ab plane and very short range correlations along **c** in optimally doped $\text{YBa}_2\text{Cu}_3\text{O}_{7-\delta}$ [22], and related superstructure in underdoped $\text{YBa}_2\text{Cu}_3\text{O}_{7-\delta}$ [23]. In these cases, the short range ordered superstructure is periodic along the shorter Cu-Cu bond, whereas the two unit cell superstructure we report here for $\text{Bi}_2\text{Sr}_2\text{CaCu}_2\text{O}_{8+\delta}$ is periodic along a diagonal of the CuO_2 basal plane cell, and thus at 45 degrees to either

Cu-Cu bond. This difference, however, may simply be a consequence of the electronic inhomogeneity following the appropriate template for $\text{Bi}_2\text{Sr}_2\text{CaCu}_2\text{O}_{8+\delta}$ or $\text{YBa}_2\text{Cu}_3\text{O}_{7-\delta}$. That template would be set by the three dimensional modulation in $\text{Bi}_2\text{Sr}_2\text{CaCu}_2\text{O}_{8+\delta}$ and by the short range oxygen-vacancy ordered superstructures in the case of $\text{YBa}_2\text{Cu}_3\text{O}_{7-\delta}$ [23], which are present throughout the superconducting region of its phase diagram[24]. We also note that recent STM measurements on $\text{Bi}_2\text{Sr}_2\text{CaCu}_2\text{O}_{8+\delta}$ [25] and $\text{Ca}_{2-x}\text{Na}_x\text{CuO}_2\text{Cl}_2$ [26] have also observed a checkerboard pattern to the local density of electronic states with a 4 to 5 lattice constant periodicity within the basal plane. These results have been interpreted as being related to static, crossed stripes[27]. It may therefore be the case that such quasi-two dimensional, short range charge inhomogeneity is a general property of cuprate high temperature superconductors and related materials.

5.5 Conclusions

We report the observations of three sets of incommensurate modulation to the structure of the high temperature superconductor $\text{Bi}_2\text{Sr}_2\text{CaCu}_2\text{O}_{8+\delta}$. Two of these are the well known modulation characterized by wavevectors $(0, 4-n\times\tau, L)$. These Bragg features alternate in both harmonic, n , for the same L , and in L for the same harmonic, between resolution-limited Bragg peaks and diffuse scattering lineshapes which are very well described by a Lorentzian-squared profile. We also confirm and extend the characterization of the recently discovered $(1/2, 4-n\times\tau, L)$ modulations. These charge correlations are quasi-two dimensional. The rod-like character of this scattering along \mathbf{c}^* is weakly peaked at $L=5$, and this scattering is characterized by finite and relatively short correlation lengths of $\sim 27 \text{ \AA}$ within the ab plane. We contend that the charge inhomogeneity underlying this diffuse scattering is that previously observed in STM measurements[9]. These new x-ray scattering measurements, in

transmission geometry, establish that this charge inhomogeneity is a bulk property of the system, and is not due to any reconstruction or related surface effect. We have also thoroughly investigated any possible temperature dependence to all three of these structural modulations below room temperature and find no such effect.

5.6 Acknowledgements

We wish to acknowledge useful discussions with J.M. Tranquada. This work was supported by NSERC of Canada. Use of the Advanced Photon Source is supported by the U.S. Department of Energy, Office of Basic Energy Sciences, under contract No. W-31-109-ENG-38. This work was supported in part by the BES (DOE) Grant DE-FG02-03ER46084 (SKS).

Bibliography

- [1] see, for example: M.R. Norman and C. Pepin, *Rep. Prog. Phys.* **66**, 1547 (2003);
J. Orenstein and A.J. Millis, *Science*, **288**, 468 (2000).
- [2] J.E. Fischer, P.A. Heiney, P.K. Davies, and D. Vaknin, *Phys. Rev. B*, **39**, 2752 (1989); A. Yamamoto, M. Onoda, E. Takayama-Muromachi, F. Izumi, T. Ishigaki, and H. Asano, *Phys. Rev. B*, **42**, 4228 (1990).
- [3] A. Damascelli, Z. Hussain, Z.X. Shen, *Rev. Mod. Phys.*, **75**, 473 (2003).
- [4] J.C. Davis, *Materials Today*, **5**, 4, 24 (2002).
- [5] although some efforts have been successful; see: H.F. Fong, P. Bourges, Y. Sidis, L.P. Regnault, A. Ivanov, G.D. Gu, N. Koshizuka, and B. Keimer, *Nature*, **398**, 588 (1999).
- [6] V. Petricek, Y. Gao, P. Lee, and P. Coppens, *Phys. Rev. B*, **42**, 387 (1990); A.A. Levin, Y.F. Shepelev, Y. I., Smolin, and A.A. Bush, *Physica C*, **291**, 155 (1997); A. Bianconi, M. Lusignoli, N.L. Saini, P. Bordet, A. Kvik, and P.G. Radaelli, *Phys. Rev. B*, **54**, 4310 (1996); X. Zhao, W. Wu, X. Sun, and X.G. Li, *Physica C*, **320**, 225 (1999).
- [7] P. Bordet, J.J. Capponi, C. Chailout, J. Chenavas, A.W. Hewat, E.A. Hewat, J.L. Hodeau, M. Marezio, J.L. Tholence, and D. Tranqui, *Physica C*, **156**, 189

- (1988); P.A. Miles, S.J. Kennedy, G.J. McIntyre, G.D. Gu, G.J. Russell, and N. Koshizuka, *Physica C*, **294**, 275 (1998).
- [8] J.C. Toledano, *Phase Transitions*, **30**, 127 (1990); W. Sun, T. Kimoto, and T. Mochiku, *J. Supercond.*, **10**, 6, 649 (1997).
- [9] S.H. Pan, J.P. O'Neal, R.L. Badzey, C. Chamon, H. Ding, J.R. Engelbrecht, Z. Wang, H. Eisaki, S. Uchida, A.K. Gupta, K.W. Ng, E.W. Hudson, K.M. Lang, and J.C. Davis, *Nature*, **413**, 282 (2001).
- [10] E.A. Hewat, M. Dupuy, P. Bordet, J.J. Capponi, C. Chaillout, J.L. Hodeau, and M. Marezio, *Nature*, **333**, 53 (1988).; H.W. Zandbergen, W.A. Groen, F.C. Lijhoff, G. van Tendeloo, and S. Amelinckx, *Physica C*, **156**, 325 (1988); Y. Matsui, H. Maeda, Y. Tanaka, and S. Horiuchi, *Jpn. J. Appl. Phys.*, **27**, L372 (1988).
- [11] M.B. Walker and W. Que, *Phys. Rev. B*, **45**, 8085 (1992).
- [12] J. Etrillard, P. Bourges, and C.T. Lin, *Phys. Rev. B*, **62**, 150 (2000).
- [13] S. Megtert, J. Avila, M. Izquierdo, P.A. Albouy, G. Gu, M.C. Asensio, and R. Comes, *J. Phys. IV France*, **118**, 333 (2004).
- [14] J.P. Castellán, B.D. Gaulin, Y. Zhao, and H.A. Dabkowska, *Bull. Am. Phys. Soc.*, **49**, 371 (2004).
- [15] R.A. Cowley in *Methods of Experimental Physics*, Vol. 23, Part C, edited by K. Skold and D.L. Price (Academic Press, Inc., 1987).
- [16] M. Hagen, R.A. Cowley, S.K. Satija, H. Yoshizawa, G. Shirane, R.J. Birgeneau and H.J. Guggenheim, *Phys. Rev. B*, **28**, 2602 (1983).
- [17] R.A. Cowley, H. Yoshizawa, G. Shirane, and R.J. Birgeneau, *Z. Phys. B*, **58**, 15 (1985).

- [18] R.M. Hazen in *Physical Properties of High Temperature Superconductors II*, edited by D.M. Ginsberg (World Scientific, Singapore, 1990.)
- [19] G. Botton, M. Niewczas and H.A. Dabkowska, private communication.
- [20] S. Sugita, T. Watanabe, and A. Matsuda, *Phys. Rev. B*, **62**, 8715 (2000).
- [21] see, for example: V.J. Emery, S.A. Kivelson, and J.M. Tranquada, *PNAS*, **96**, 6, 8814 (1999).
- [22] Z. Islam, X. Liu, S.K. Sinha, J.C. Lang, S.C. Moss, D. Haskel, G. Srajer, P. Wochnner, D.R. Lee, D.R. Haeffner, and U. Welp, *Phys. Rev. Lett.*, **93**, 157008 (2004); J. Stremper, I. Zegkinoglou, U. Rutt, M. v. Zimmermann, C. Bernhard, C.T. Lin, Th. Wolf, and B. Keimer, *Phys. Rev. Lett.*, **93**, 157007 (2004).
- [23] Z. Islam, S.K. Sinha, D. Haskel, J.C. Lang, G. Srajer, B.W. Veal, D.R. Haeffner, and H.A. Mook, *Phys. Rev. B*, **66**, 092501 (2002).
- [24] D. de Fontaine, V. Ozolins, Z. Islam, and S.C. Moss, *Phys. Rev. B*, **71**, 212504 (2005).
- [25] K. McElroy, D.H. Lee, J.E. Hoffman, K.M. Lang, J. Lee, E.W. Hudson, H. Eisaki, S. Uchida, and J.C. Davis, *Phys. Rev. Lett.*, **94**, 197005 (2005); A. Fang, C. Howald, N. Kaneko, M. Greven, and A. Kapitulnik, *Phys. Rev. B*, **70**, 214514 (2004); C. Howald, H. Eisaki, N. Kaneko, M. Greven, and A. Kapitulnik, *Phys. Rev. B*, **67**, 014533 (2003); J.E. Hoffman, K. McElroy, D.H. Lee, K.M. Lang, H. Eisaki, S. Uchida, and J.C. Davis, *Science*, **297**, 1148 (2002).
- [26] T. Hanaguri, C. Lupien, Y. Kohsaka, D.H. Lee, M. Azuma, M. Takano, H. Takagi, and J.C. Davis, *Nature*, **430**, 1001 (2004).
- [27] R.S. Markiewicz, *Phys. Rev. B*, **71**, 220504(R) (2005).

Chapter 6

Structural Ordering and Symmetry Breaking in $\text{Cd}_2\text{Re}_2\text{O}_7$

This chapter incorporates the article “Structural Ordering and Symmetry Breaking in $\text{Cd}_2\text{Re}_2\text{O}_7$ ”, Phys. Rev. B, **66** 134528(2002). The x-ray experiments were performed on the rotating anode x-ray generator at McMaster University. The samples were prepared by J. He from the Department of Physics and Astronomy of the University of Tennessee. The experiments and subsequent data analysis was performed by myself under the guidance of B.D. Gaulin. The article was authored by myself and B.D. Gaulin.

Structural Ordering and Symmetry Breaking in $\text{Cd}_2\text{Re}_2\text{O}_7$ ¹

J.P. Castellan¹, B.D. Gaulin^{1,4}, J. van Duijn¹, M. J. Lewis¹, M. D. Lumsden², R.
Jin², J. He³, S. E. Nagler², and D. Mandrus^{2,3}

¹*Department of Physics and Astronomy, McMaster University, Hamilton, Ontario,
L8S 4M1, Canada*

²*Solid State Division, Oak Ridge National Laboratory, P.O. Box 2008, Oak Ridge,
TN, 37831 U.S.A.*

³*Department of Physics and Astronomy, The University of Tennessee, Knoxville,
TN, 37996 U.S.A.*

⁴*Canadian Institute for Advanced Research, 180 Dundas St. W., Toronto, Ontario,
M5G 1Z8, Canada*

¹©2002 The American Physical Society

Abstract

Single crystal X-ray diffraction measurements have been carried out on $\text{Cd}_2\text{Re}_2\text{O}_7$ near and below the phase transition it exhibits at $T_{C'} \sim 195$ K. $\text{Cd}_2\text{Re}_2\text{O}_7$ was recently discovered as the first, and to date only, superconductor which displays the cubic pyrochlore structure at room temperature. Superlattice Bragg peaks show an apparently continuous structural transition at $T_{C'}$, however their behavior is unconventional. The evolution with temperature of these Bragg intensities show anomalously strong temperature dependence at low temperatures, where it falls off as $I_0(1-BT^2)$, and resolution limited critical-like scattering is seen above $T_{C'}$. High resolution measurements show the high temperature cubic Bragg peaks to split on entering the low temperature phase, indicating a (likely tetragonal) lowering of symmetry below $T_{C'}$.

6.1 Introduction

Materials which crystallize into the cubic pyrochlore structure have been of intense recent interest, due to the presence of networks of corner-sharing tetrahedra within such structures [1]. Cubic pyrochlores display chemical composition $A_2B_2O_7$, and space group $Fd\bar{3}m$. Independently, both the A and B sublattices reside on networks of corner-sharing tetrahedra, an architecture also common to Laves phase cubic spinels, for example. Such materials have the potential to display phenomena related to geometrical frustration in the presence of antiferromagnetism. While much activity has focused on local magnetic moments in insulating pyrochlores, interesting metallic properties have also been observed recently. The $RE_2Mo_2O_7$ system (where RE is a rare earth ion), for example, is well studied and is known to undergo a transition from metallic ferromagnetism to semiconducting spin glass behavior as one moves from the light to the heavy rare earths occupying the A sublattice of the pyrochlore structure [2]. One such metallic pyrochlore $Nd_2Mo_2O_7$ [3] has recently been seriously studied and a large anomalous Hall effect has been measured. In $Cd_2Os_2O_7$, a metal insulator transition has recently been shown to occur near 226 K [4], while the spinel LiV_2O_4 is the only known transition metal based heavy fermion conductor [5].

While many metallic, cubic pyrochlore oxides exist, no superconductors were known to exist within this family of materials until very recently. Hanawa et al.[6], Sakai et al.[7], and Jin et al.[8] have all recently reported superconductivity in $Cd_2Re_2O_7$, the first such pyrochlore. The superconducting T_C 's are somewhat sample dependent and have been reported between 1 and 2 K. Moreover, the relatively high temperature metallic properties are anomalous, and may be driven by an as-yet poorly-understood phase transition near $T_{C'} \sim 195$ K [9]. In this paper, we report on the nature of the phases above and below $T_{C'}$ as well as the phase transition itself. We show compelling evidence for a splitting of the cubic Bragg peaks, indicating a

lowering of symmetry below $T_{C'}$, likely to a tetragonal structure, as well as an unusual order parameter which grows very slowly with decreasing temperature.

$\text{Cd}_2\text{Re}_2\text{O}_7$ is a rather poor metal near room temperature, exhibiting an almost flat resistivity between 200 K and 400 K [6, 7, 9]. Just below 200 K, the resistivity falls off sharply, continuing down to a low temperature Fermi liquid regime characterized by a T^2 dependence to the resistivity between 2 K and roughly 60 K, and a residual resistivity on the order of $10 \mu \text{ ohm-cm}$ [8, 6]. On further lowering the temperature, the resistivity falls to zero, at $T_C \sim 1.4 \text{ K}$ in crystals from the same batch as that under study here, indicating the onset of the superconducting state. Heat capacity measurements show a large anomaly at T_C , while above T_C these measurements give a Sommerfeld γ value of roughly 30 mJ/mol-K^2 . This result can be combined with A , the coefficient of the quadratic term in the temperature dependence of the resistivity, to give a Kadowaki-Woods ratio, A/γ , similar to that seen in highly correlated metals such as the heavy fermion superconductor UPe_{13} [8]. Recent transverse field μSR measurements [10] reveal the presence of a vortex lattice below T_C , with a large and temperature independent value of the penetration depth below $0.4T_C$. These measurements show $\text{Cd}_2\text{Re}_2\text{O}_7$ to be a type II superconductor and are consistent with a nodeless superconducting energy gap.

Heat capacity measurements show a pronounced anomaly near $T_{C'} \sim 200\text{K}$, consistent with a continuous phase transition[9]. Electron diffraction from single crystals[9] and preliminary x-ray diffraction studies from powder samples[11] show the appearance of superlattice Bragg peaks at reflections such as $(0,0,6)$ and $(0,0,10)$, which are inconsistent with the $(0,0,h): h=4n$ condition appropriate to the high temperature cubic space group. In addition, DC susceptibility measurements[6, 9] show an abrupt reduction in the susceptibility below $T_{C'}$. Very recent Re NQR measurements, however, have revealed no indication of either a magnetically ordered

or a charge ordered state below 100 K[12].

6.2 Experimental Details

The high quality single crystal, which is the subject of the present study, was grown as reported by He et al.,[13] and had approximate dimensions $4 \times 4 \times 2\text{mm}^3$ and a mosaic spread of less than 0.04° full width at half maximum. It was mounted in a Be can in the presence of a He exchange gas and connected to the cold finger of a closed cycle refrigerator with approximate temperature stability of 0.005 K near $T_{C'}$, and 0.01 K elsewhere. X-ray diffraction measurements were performed in two modes, both employing an 18 kW rotating anode generator, Cu $K\alpha$ radiation, and triple axis diffractometer. Relatively low resolution measurements of the superlattice Bragg peak intensities were obtained using a pyrolytic graphite (002) monochromator and a scintillation counter. Much higher resolution measurements were performed with a perfect Ge (111) monochromator, and a Bruker Hi Star area detector, mounted 0.75 m from the sample position on the scattered beam arm of the diffractometer. The high resolution experiment easily separated $\text{Cu}_{K\alpha_1}$ from $\text{Cu}_{K\alpha_2}$ diffraction, and was used for precision measurements of the line shapes of both the principal and superlattice Bragg peaks.

6.3 Order Parameter

Figure 6.1 shows the temperature dependence of the integrated intensity of low resolution scans of the (0,0,10) superlattice Bragg peak. Data was taken in separate warming and cooling runs, and is shown over an extended temperature range in the top panel, as well as over a narrow range near $T_{C'}$ in the bottom panel. The form of this scattering, proportional to the square of the order parameter, is anomalous

as it grows very slowly below $T_{C'}$, especially between ~ 170 K and ~ 40 K. A mean field phase transition displays the slowest such growth among conventional models for cooperative behavior which exhibit continuous phase transitions. In Fig. 6.1, we compare the integrated intensity of the superlattice Bragg scattering to the square of the mean field order parameter[14], as well as to the square of the order parameter appropriate to the three dimensional Ising model[15]. Clearly the growth of the measured order parameter is much slower with decreasing temperature, than would be predicted by even mean field theory. Closer to the phase transition, the measured order parameter does look more conventional as shown in the bottom panel of Fig. 6.1. This panel shows integrated intensity with both downward curvature below ~ 195 K, and upward curvature above ~ 195 K, consistent with the measurement of the order parameter squared below $T_{C'}$. and the measurement of fluctuations in the order parameter, or so-called critical scattering, above $T_{C'}$. Data in the temperature range 175 K to 190 K was analyzed assuming this to be the case, and fits were carried out in the approximate range of reduced temperature from 0.02 to 0.10, placing the data within a typical asymptotic critical regime. The fit of this data by the critical form:

$$Intensity = I_0 \left(\frac{T_{C'} - T}{T_{C'}} \right)^{2\beta} \quad (6.1)$$

is shown in the bottom panel of Fig. 1. The fit is of high quality, and it produces $T_{C'}=194.3 \pm 0.1$ K and a critical exponent $\beta=0.33 \pm 0.03$, which is typical of three dimensional continuous phase transitions [16].

Although the (0,0,10) intensity above $T_{C'}=194.3$ K appears to be critical scattering, we show below that it is anomolous and remains resolution limited at all temperatures measured. \mathbf{Q} -broadened critical fluctuations can be measured by moving slightly off the (0,0,10) Bragg position, however it is extremely weak. Scattering at (0.04,0.064,10) is shown in the bottom panel of Fig. 6.1 and it displays a weak peak

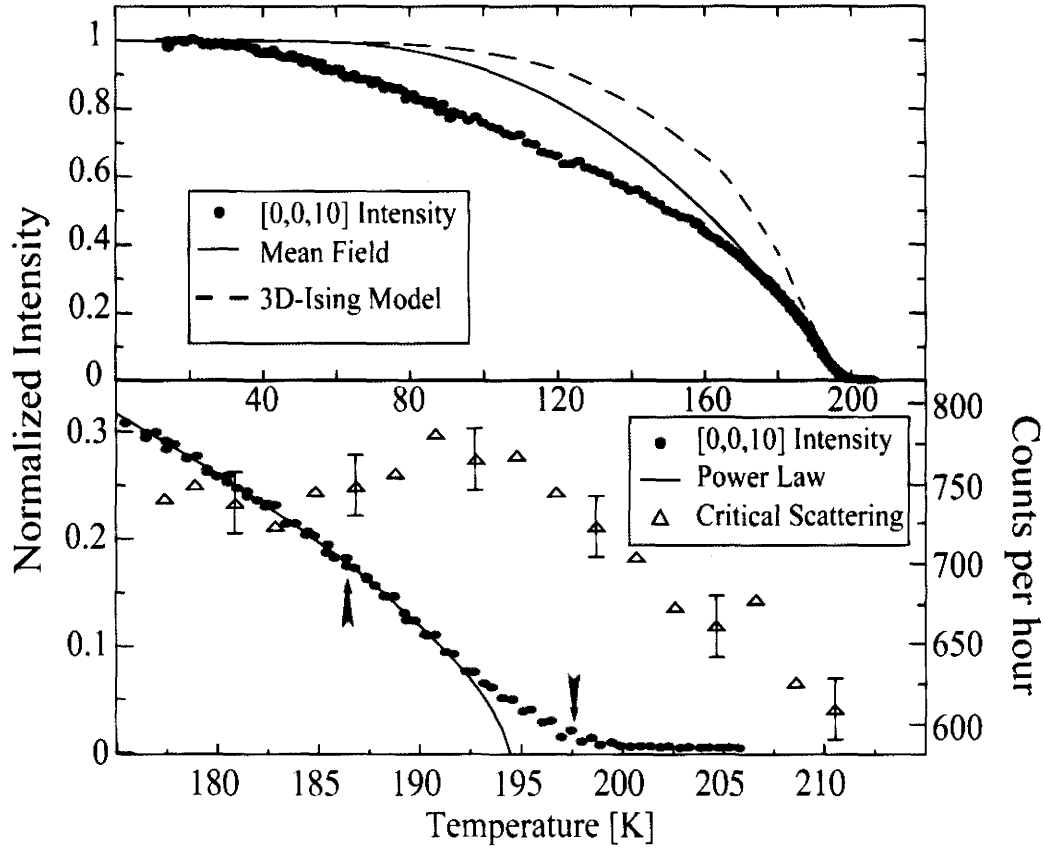


Figure 6.1: The top panel shows the integrated intensity of the (0,0,10) superlattice Bragg peak as a function of temperature, compared with the square of the order parameter expected from mean field theory, and that expected from the 3 dimensional Ising model. The lower shows the same data in the immediate vicinity of $T_C \sim 194$ K, along with a fit to critical behavior modeled as a power law in reduced temperature (left-hand y-axis), and the broad critical scattering as measured at (0.04,0.064,10) (right-hand y-axis).

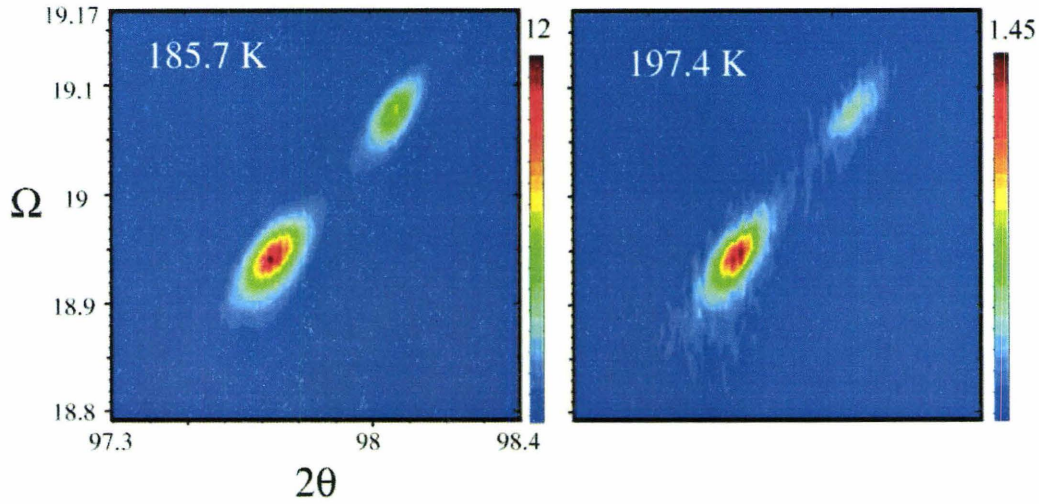


Figure 6.2: High resolution scans of the scattering at and near the (0,0,10) superlattice Bragg peak positions are shown for the temperatures marked by arrows in the inset to Fig. 6.1. Data is shown in maps as a function of sample rotation angle Ω and scattering angle 2θ . The two diffraction features at 2θ values of $\sim 97.7^\circ$ and 98.07° are from Cu $K_{\alpha 1}$ and Cu $K_{\alpha 2}$ radiation, respectively. The top of the linear color scale is different for each data set.

near $T_{C'}$, as expected for a continuous phase transition. This broad scattering is measured in counts per *hour*, and it makes a negligible contribution to the overall scattering around (0,0,10) above $T_{C'}=194.3\text{K}$. It does however provide a consistency check on the phase transition occurring at 194.3K.

High resolution measurements of the lineshape of the (0,0,10) superlattice Bragg peak, shown in Fig. 6.2, reveal that almost all of this scattering above $T_{C'}=194.3\text{K}$ remains resolution limited; it is indistinguishable from the superlattice scattering below 194.3K, albeit weaker in intensity. Figure 6.2 shows maps of the scattering at and around the (0,0,10) superlattice position at temperatures of 185.7K and 197.4K. As indicated by the arrows superposed on the order parameter shown in

the bottom panel of Fig. 6.1, these temperatures correspond to well below and well above $T_{C'}$.

The 197.4 K data set definitely falls within the upward curvature regime of the temperature dependence of the superlattice integrated intensity, and would normally be expected to be due to fluctuations in the order parameter rather than due to the order parameter itself. As discussed above, such critical scattering is expected to broaden in Q , and therefore in angular coordinates, as the temperature increases beyond $T_{C'}$, indicating a finite and decreasing correlation length. Such broadening is clearly not observed in this scattering above $T_{C'}$.

The anomalous nature of the line shape of the superlattice scattering above $T_{C'}$ may be due to “second length scale” scattering[17], which has often been observed in high resolution synchrotron x-ray experiments near phase transitions in crystalline materials. It is not fully understood, but has been associated with the effect of near-surface quenched disorder on the phase transition. The x-rays in the present measurements have a penetration depth of the order of ten microns (tens of thousands of unit cells) and are thus not particularly surface sensitive.

It may also be that this superlattice Bragg scattering is not the primary order parameter for the phase transition near $T_{C'}$, but is a secondary feature, pulled along by the true underlying phase transition. The anomalously slow growth of the (0,0,10) superlattice Bragg peak at low temperatures also supports such an interpretation.

6.4 Lattice Parameters

We also carried out measurements of the principal Bragg peaks (which satisfy the (00h): $h=4n$ relation) at high scattering angle and in high resolution mode. Scans along the longitudinal direction, cutting through both Cu $K\alpha_1$ and Cu $K\alpha_2$ peaks of the (0,0,12) principal Bragg peaks, are shown in the right hand panels of Fig. 6.3

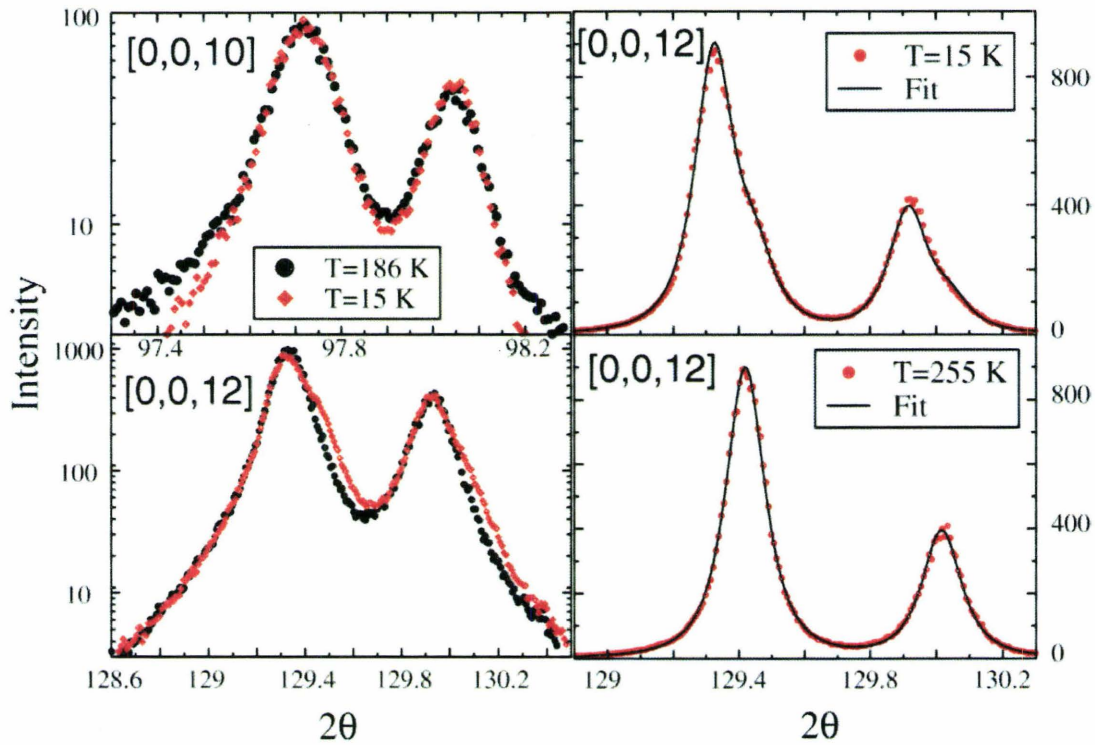


Figure 6.3: The right hand panels shows longitudinal cuts taken through the $(0,0,12)$ principal Bragg peak position well above $T_{C'}$ (bottom) and well below (top). This data, on a linear scale, shows a clear shoulder on the high 2θ side of both the $\text{Cu } K_{\alpha 1}$ and $K_{\alpha 2}$ peaks. The left hand panels show the superlattice $(0,0,10)$ (top) and principal $(0,0,12)$ (bottom) Bragg peaks on a semi-log scale, at temperatures just below and well below $T_{C'}$. Clearly, while the principal Bragg peaks split on lowering the temperature, the superlattice peaks do not.

on a linear scale, and in the bottom, left panel of Fig. 6.3 on a semi-log scale. For comparison, similar longitudinal scans through the superlattice (0,0,10) Bragg peaks are shown on a semi-log scale in the top left panel of Fig. 6.3. The data sets at the two temperatures which make up both semi-log plots on the left side of Fig. 6.3 have been shifted slightly in 2θ and, in the case of (0,0,10), scaled in intensity to allow for comparison.

A shoulder is clearly seen to develop on the high angle side of the (0,0,12) peaks as the temperature is lowered below $T_{C'}$. This indicates a splitting of the cubic Bragg peak into a lineshape characterized by at least two different lattice parameters, and consequently a symmetry lower than cubic, likely tetragonal, in the low temperature state below $T_{C'} \sim 194.3$ K.

A similar splitting of the (0,0,10) superlattice Bragg peak is *not* observed. The superlattice Bragg peaks do not exist above $T_{C'}$ and thus we must compare superlattice data taken below, but near $T_{C'}$ with that taken well below $T_{C'}$. That is what is shown for both the principal (0,0,12) Bragg peak and the superlattice (0,0,10) Bragg peak at temperatures of 186 K and 15 K, respectively in the left hand panels of Fig. 36.3. At 186 K, the splitting is not yet evident in either the principal, (0,0,12), or superlattice, (0,0,10), Bragg peaks, but by 15 K it is clear in the principal Bragg peak, but not in the superlattice Bragg peaks.

We fit the high temperature data at (0,0,12) to a phenomenological form at 255 K, assuming this to be the resolution-limited lineshape. We then fit (0,0,12) data at all temperatures to a form assuming the superposition of two such lineshapes, displaced from each other in scattering angle (2θ). This protocol allowed us to extract peak positions for each of two peaks, giving the lattice parameters as a function of temperature. This analysis assumes that only two lattice parameters are present at low temperatures, that is that the low temperature structure is tetragonal. The data

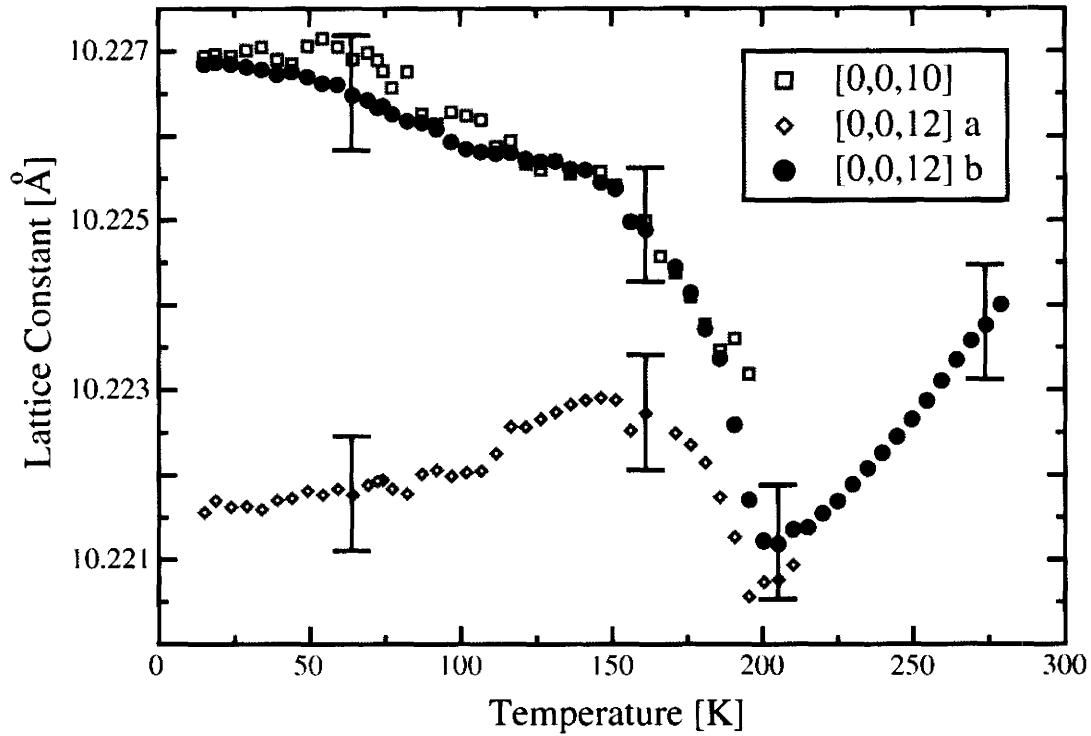


Figure 6.4: The temperature dependence of the lattice parameters extracted from fits to the (0,0,12) principal Bragg peaks are shown, along the temperature dependence of the superlattice (0,0,10) Bragg peak periodicity below $T_{C'}$. The error bars indicate uncertainties associated with the absolute values of the lattice parameters.

at 15 K in the top right panel of Fig. 6.3 shows the quality of this fit, and clearly the description of the data is very good. The resulting tetragonal lattice parameters as a function of temperature are shown in Fig. 6.4.

6.5 Discussion

The behavior of the lattice parameters as a function of temperature is striking. The cubic lattice parameter displays the usual thermal contraction with decreasing temperature until near $T_{C'}$. The splitting in the lattice parameters first develops near 200 K, with a 30 K interval from ~ 190 K to 160 K in which both lattice parameters increase with decreasing temperature. This trend continues to lower temperatures for the larger of the two lattice parameters, while the smaller turns over below ~ 150 K and displays relatively weak contraction to lower temperatures. At the lowest temperature measured, 15 K, the maximum splitting in lattice parameter measured is about 0.005 Å or 0.05 %.

The (0,0,10) superlattice peak does not show any splitting, and the temperature dependence associated with its periodicity is also shown in Fig. 6.4. It clearly follows the upper branch of the two lattice parameters associated with (0,0,12). These results imply that the low temperature state below $T_{C'}$ is likely twinned tetragonal, such that two of (0,0,12), (0,12,0) and (12,0,0) have one lattice parameter, while the other has a slightly different one. The fact that the superlattice peak displays no splitting implies that only the subset of (0,0,10), (0,10,0) and (10,0,0) which follow the upper branch of the lattice parameter vs temperature curve shown in Fig. 6.4, exists. The other(s) is (are) systematically absent. These observations allow us to discuss possible tetragonal space groups appropriate to the low temperature state below $T_{C'}$. As the transition appears to be close to continuous, we assume the low temperature state to be a gradual distortion of the high temperature cubic state, and

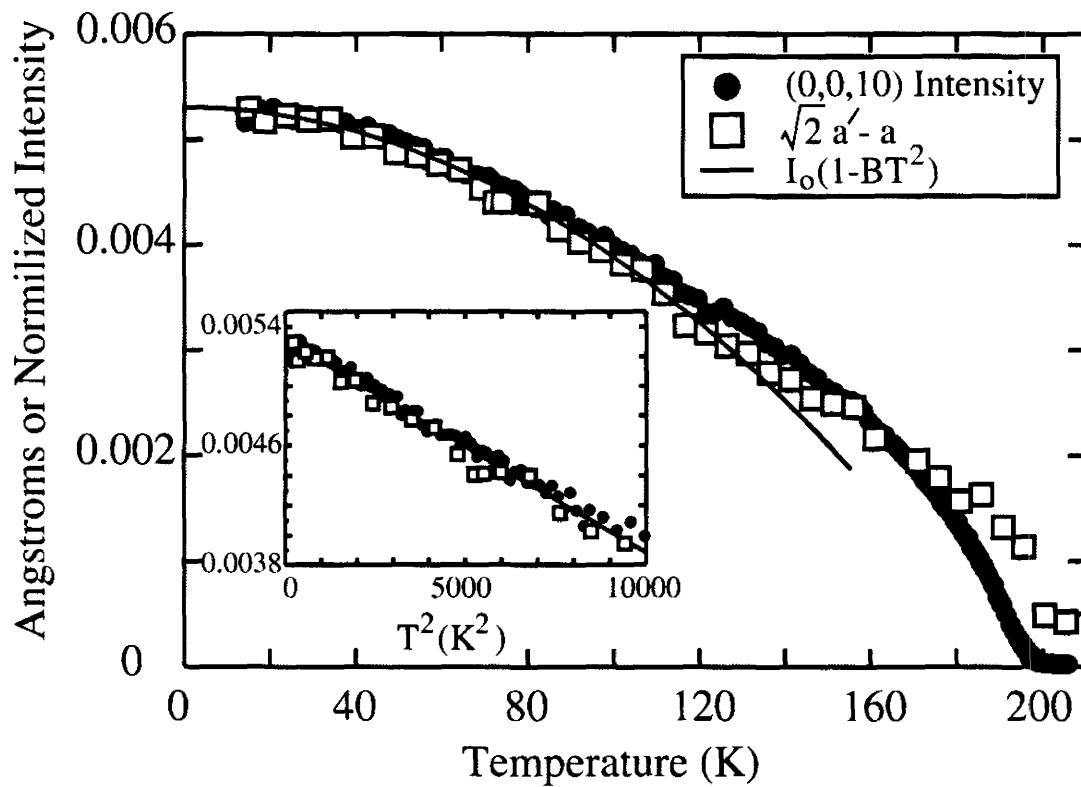


Figure 6.5: The temperature dependence of the lattice parameters extracted from fits to the (0,0,12) principal Bragg peaks are shown, along the temperature dependence of the superlattice (0,0,10) Bragg peak periodicity below $T_{C'}$.

thus the low temperature space group should be a subgroup of $Fd\bar{3}m$. There are two body-centered subgroups of $Fd\bar{3}m$ which, in the presence of twinning, would split $(0,0,12)$ and allow a single periodicity for $(0,0,10)$. These are $I4_1$ and $I4_122$. In both cases the primitive unit vectors of the basal (a' - a') plane are rotated by 45° relative to the unit vectors, a , of the high temperature cubic unit cell, and $a'=a/\sqrt{2}$.

We return now to the question of the anomalously strong temperature dependence of the superlattice Bragg peak intensity at low temperatures. In Fig. 6.5 we compare the temperature dependence of the $(0,0,10)$ superlattice intensity with the difference between the lattice parameters $\sqrt{2}a'-a$, taken from the analysis leading to Fig. 6.4. Figure 6.5 shows clearly that the same anomalous temperature dependence is seen in both the superlattice Bragg peak intensity and in $\sqrt{2}a'-a$. This is certainly surprising as the superlattice Bragg peak intensity is associated with the *square* of the order parameter in most structural phase transitions, while the difference in lattice parameter, $\sqrt{2}a'-a$, is most naturally taken as the order parameter itself.

This result suggests that the temperature dependence of both the superlattice Bragg intensity and the difference in lattice parameter are driven by the same physical origin, at least at low temperatures. Over the temperature range from low temperatures until almost 100 K, both quantities are well described by $I_0(1-BT^2)$. This quadratic temperature dependence was fitted to the data and is shown in Fig. 6.5 as a solid line. The inset of Fig. 6.5 shows both the $(0,0,10)$ intensity and $\sqrt{2}a'-a$ plotted as a function of the temperature squared. There is no doubt that the decay of both the difference in lattice parameter and the superlattice intensity goes as T^2 at low temperatures. As the low temperature resistivity of this material displays Fermi liquid behavior and goes like T^2 to temperatures as high as 60 K, an electronic origin for the low temperature behavior of the evolving structure is very strongly suggested. Given that the electronic properties are strongly correlated to the structural phase

transition at $T_{C'}$, it is perhaps not so surprising that such a strong correlation is evident at low temperatures as well.

6.6 Summary

While we cannot be more precise as to the low temperature space group at this time, we have unambiguously shown the symmetry of the low temperature state to be lower than cubic, and that this cubic symmetry breaking is an essential feature of the phase transition. The most likely scenario is that $\text{Cd}_2\text{Re}_2\text{O}_7$ undergoes a cubic to tetragonal phase transition, with the primary order parameter being the difference in lattice parameters, given by $\sqrt{2}a'-a$. We note that we do not expect this splitting of the lattice parameters to be evident in bulk measurements unless a single domain sample can be produced at low temperatures.

We have also shown that the superlattice Bragg peak intensities display anomalously strong temperature dependence at low temperature, going like $I_0(1-BT^2)$ at temperatures below ~ 100 K. These results indicate a strong coupling between the electronic properties and the evolving structure at all temperatures below $T_{C'}=194.3\text{K}$.

Finally it is interesting to note that recent theoretical work may have anticipated such a structural phase transition related to the underlying network of corner-sharing tetrahedra. This work[18] discusses the role of magnetoelastic couplings in generating “order by distortion” in pyrochlore antiferromagnets.

We wish to acknowledge useful discussions with J.F. Britten. This work was supported by NSERC of Canada. Oak Ridge National Laboratory is managed by UT-Battelle, LLC the U.S. D.O.E. under Contract DE-AC05-00OR22725. Work at UT is supported by NSF DMR-0072998.

Bibliography

- [1] for recent reviews see: S.T. Bramwell and M.J.P. Gingras, *Science*, **294**, 1495 (2001), **Magnetic Systems with Competing Interactions**, edited by H.T. Diep (World Scientific, Singapore (1994), P. Schiffer and A.P. Ramirez, *Comm. Cond. Mat. Phys.*, **18**, 21 (1996).
- [2] N. Ali, M.P. Hill, S. Labroo, and J.E. Greedan, *J. Solid State Chem.*, **83**, 178 (1989); T. Katsufuji, H.Y. Hwang, and S.-W. Cheong, *Phys. Rev. Lett.*, **84**, 1998 (2000).
- [3] Y. Taguchi, Y. Oohara, H. Yoshizawa, N. Nagaosa, and Y. Tokura, *Science*, **291**, 2573 (2001).
- [4] D. Mandrus, J. R. Thompson, R. Gaal, L. Forro, J. C. Bryan, B. C. Chakoumakos, L. M. Woods, B. C. Sales, R. S. Fishman, and V. Keppens, *Phys. Rev. B*, **63**, 195104 (2001).
- [5] S. Kondo et al., *Phys. Rev. Lett.*, **78**, 3729, (1997); C. Urano et al., *Phys. Rev. Lett.*, **85**, 1052 (2000).
- [6] M. Hanawa, Y. Muraoka, T. Tayama, T. Sakakibara, J. Yamaura, and Z. Hiroi, *Phys. Rev. Lett.*, **87**, 187001, (2001)

- [7] H. Sakai, K. Yoshimura, H. Ohno, H. Kato, S. Kambe, R. E. Walstedt, T. D. Matsuda, Y. Haga and Y. Onuki, *J. Phys. Cond. Mat.* **13**, L785 (2001).
- [8] R. Jin, J. He, S. McCall, C.S. Alexander, F. Drymiotis, and D. Mandrus, *Phys. Rev. B*, **64**, 180503(R), (2001)
- [9] R. Jin, J. He, J.R. Thompson, M.F. Chrisholm, B.C. Sales, and D. Mandrus, *cond-mat/0108402*.
- [10] M.D. Lumsden, S.R. Dunsiger, J.E. Sonier, R.I. Miller, R.F. Kiefl, R. Jin, J. He, D. Mandrus, S.T. Bramwell, J.S. Gardner, *cond-mat/0111187*; R. Kadono, W. Higemoto, A. Koda, Y. Kawasaki, M. Hanawa, and Z. Hiroi, *cond-mat/0112448*.
- [11] M. Hanawa, J. Yamaura, Y. Muraoka, F. Sakai, Z. Hiroi, *cond-mat/0109050*.
- [12] O. Vyaselev, K. Arai, K. Kobayashi, J. Yamazaki, K. Kodama, M. Takigawa, M. Hanawa, and Z. Hiroi, *Phys. Rev. Lett.*, **89**, 017001 (2002).
- [13] J. He et al., unpublished.
- [14] M. Plischke and B. Birgerson, *Equilibrium Statistical Physics, 2nd Edition*, World Scientific Press (1994).
- [15] D.M. Burley, *Philos. Mag.* **5**, 909 (1960).
- [16] M.F. Collins, *Magnetic Critical Scattering*, Oxford University Press (1989).
- [17] for example: S.R. Andrews, *J. Phys. C* **19**, 3721 (1986).; T. R. Thurston, G. Helgesen, Doon Gibbs, J. P. Hill, B. D. Gaulin, and G. Shirane, *Phys. Rev. Lett.* **70**, 3151 (1993).
- [18] O. Tchernyshyov, R. Moessner, and S.L. Sondhi, *Phys. Rev. Lett.*, **88**, 067203 (2002).